Dissertation
submitted to the
Combined Faculties for the Natural Sciences and for Mathematics
of the Ruperto-Carola University of Heidelberg, Germany
for the degree of
Doctor of Natural Sciences

Put forward by
Dipl.-Phys. Ilia Louban
born in Kiev, Ukraine

Oral examination: November 4th, 2009

Mimicking the Cellular Environment: effects of elastic nanopatterned substrates on integrin-mediated cellular interactions

Referees: Prof. Dr. Joachim P. Spatz
Prof. Dr. Rainer Fink

Contents

Zusammenfassung

Die vorliegende Arbeit befasst sich mit der Reaktion von Zellen auf sich verändernde Umwelteinflüsse. Um dies zu untersuchen, wurde ein Substratsystem entwickelt, dessen biomechanische und biochemische Eigenschaften deren der extrazellulären Matrix des Bindegewebes entsprechen. Die verwendeten Substrate basieren auf Polyethylenglykol-Diakrylat (PEG-DA), dessen Elastizität E_Y innerhalb von vier Größenordnungen variiert werden kann (0.6 kPa $< E_Y <$ 6 MPa). Auf ihrer Oberfläche wurden mit Hilfe der Block-Copolymer-Nanolithographie Goldnanopartikel gezielt in den Abständen ΔL (20 nm $< \Delta L <$ 160 nm) angeordnet. Um die Adhäsion der Zellen zu ermöglichen, wurden die Partikel mit dem c(RGDfK) Peptid funktionalisiert, welches die Anbindung der Zellen durch Integrine gewährleistet. Das Verhalten von Fibroblasten wurde als Funktion der Substratelastizität sowie des Abstandes der Nanopartikel (ΔL; E_Y) untersucht. Die Interaktionszeit der Zellen mit den Substraten betrug sechs, zwölf, bzw. 24 Stunden. Als Reaktion wurde die zellulären Flächen mit Phasenkontrastmikroskopie sowie die Adhäsionskraft mit Kraftspektroskopie quantifiziert. Die Experimente zeigten, dass ein Schwellwert in der zellulären Reaktion bezüglich der Substratelastizität ($E_Y \approx$ 8 kPa), sowie ein anderer bezüglich des Abstands der Bindungsstellen ($\Delta L \approx$ 70 nm) existiert. Darüber hinaus wurde festgestellt, dass die Fähigkeit der Zellen die mechanischen Eigenschaften ihrer Umgebung wahrzunehmen, das "Mechanosensing", die dominante Komponente im zellulären Verhalten ist. Diese Erkenntnis trägt demzufolge entscheidend zum besseren Verständnis der Zell-Zell und der Zell-Matrixinteraktion bei.

Abstract

In this work, the influence of environmental parameters on cellular behavior has been investigated. Therefore, an artificial substrate system, according to the biophysical and biochemical properties of the extracellular matrix in connective tissues, has been developed. The Young's moduli E_Y of poly(ethylene glycol)-diacrylate (PEG-DA) substrates span more than four orders of magnitude (0.6 kPa $< E_Y <$ 6 MPa). Since PEG-DA substrates are protein repellent, they were decorated by quasi hexagonally ordered, extended gold nanoparticle arrays, manufactured by block copolymer micellar nanolithography (BCMN). To provide bioactivity in terms of cell adhesion c(RGDfK) peptide, which is specific for $\alpha_V\beta_3$ integrins, was immobilized on the nanoparticles. The interparticle spacing and, hence, spacing of integrin binding sites ΔL could be precisely tuned, independently of the substrate rigidity, between 20 nm and 160 nm. We investigated the behavior of fibroblasts as a function of changes within this two-dimensional parameters space (ΔL; E_Y). To this end, cell spreading area and cell-substrate interaction forces were determined by phase contrast microscopy and single cell force spectroscopy (SCFS), respectively. The experiments revealed two tactile set points, thresholds in cellular sensing behavior, at $E_Y \approx$ 8 kPa and $\Delta L \approx$ 70 nm, after 6, 12, and 24 hours of adhesion, respectively. Moreover, according to the hierarchical phase model in cellular behavior, elasticity was identified to be the dominant parameter in cellular sensing processes. Thus, this work provides an important contribution to the understanding of cell-cell and cell-matrix adhesion.

Part I

Introduction

Chapter

1

Cells and their environment

Cells are the essential and basic structural subunit of living creatures. The assembly of any multicellular organism requires a high level of communication between single cells. Therefore, the organisms are formed of many different types of tissues, in which cells are assembled and bound together. Within these cell aggregates, cells form connections which stabilize the tissue and allow to maintain and control it to support its long-range assembly with specific structural and mechanical properties.

In animal tissues the space between cells is filled by the extracellular matrix (ECM), which is constituted by proteins and polysaccharides produced and arranged by the cells. Cell-cell and cell-matrix interactions, generally termed as cellular adhesions, play a crucial role in the life of a cell. These influence the motility of the cell, its shape and general behavior like regulation and initiation of diverse signaling networks. Cell contacts are established between either adjacent cells or between proteins present in the extracellular compartment.

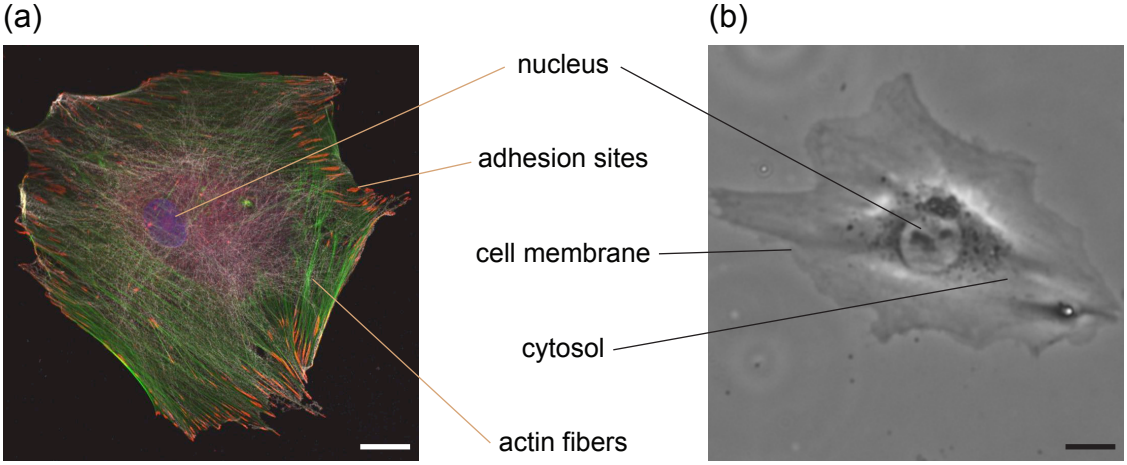

Figure 1.1: The main components of a cell. Fluorescence[a] (a) and phase contrast micrographs show cells (fibroblasts) as highly organized structures. Scale bars 20 µm.

[a]Kindly provided by Jasmin Zahn

1.1 The structure of a cell

All cells can be roughly separated into four major parts: the cell membrane, the cytosol with its embedded organelles, the nucleus and the cytoskeleton. This main structural components are displayed in Figures 1.1 and 1.2. The cellular membrane, separates the cytosol from the extracellular space. It consists of an approximately 5 nm thick lipid bilayer, where numerous membrane and transmembrane receptors are embedded and a glycocalix, a several nm to µm thick layer of polysaccharide molecules. In the cytosol, most chemical reactions such as the generation of adenosine triphosphate (ATP), the biological energy carrier necessary for the synthesis and formation of proteins, take place. The nucleus in the cell center carries the genetic code in form of deoxyribonucleic acid (DNA). The cytoskeleton is a versatile set of protein networks, which enables cells to adapt to their environment and maintain their structural integrity. Furthermore, it is responsible for directed cell movement, cell division and intracellular transport [1].

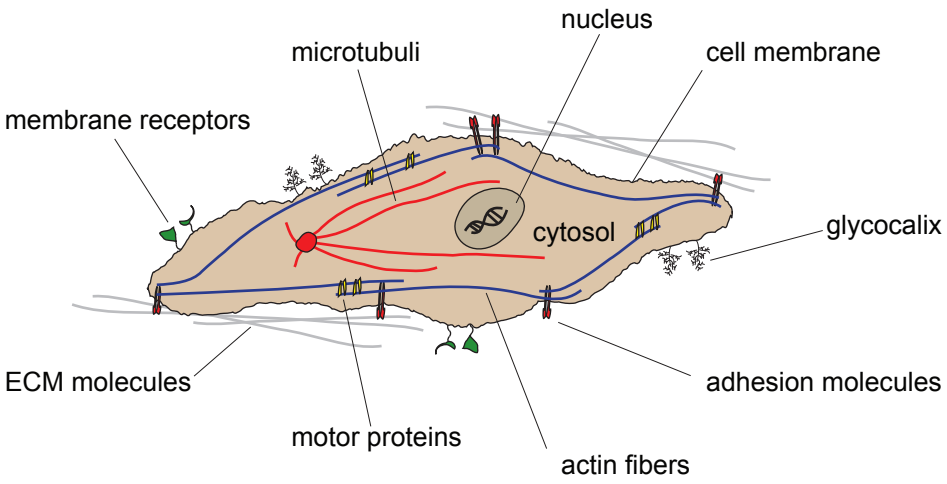

Figure 1.2: Scheme of the structural components of a cell.

The cytoskeleton is composed of three distinct protein filament structures: intermediate filaments, microtubule and actin fibers. Each of these three filament systems exhibits distinct mechanical properties. This composition of elastic and fluid-like components results in the strong viscoelastic* behavior which is observed in cells and their constituents [2].

Intermediate filaments are rope-like fibers with tensile strength and, therefore, resist mechanical stress during force application. They have a diameter of approximately 10 nm and are distributed within the entire cell [3, 4].

Microtubules are hollow cylinders of approximately 25 nm in diameter made of protein called tubulin. They grow out from the centrosome, a structure close to

*Principles of viscoelasticity are discussed in Chapter 2.2.2.

the cell center. Their mechanical properties can be described as relatively stiff rods. Microtubules are responsible for positioning of organelles and support the cell division with a mechanical framework, the mitotic spindle [1, 5].

Actin filaments are relatively long filaments built up by globular actin. They feature a diameter of nearly 7 nm and are allocated beneath the cell membrane. Actin filaments, together with motor proteins, called myosins are essential for the generation of forces. These actomyosin stress fibers are crucially involved in cell motility, cell adhesion and cell division.

In case of adherent cells, transmembrane proteins, the cell adhesion proteins (CAMs) are connected through a variety of other molecules and membrane proteins to the cytoskeletal network [6]. These proteins are composed of three domains: a large extracellular part, a transmembrane domain and a short intracellular part [1]. The extracellular portion of the transmembrane adhesion protein binds to a complementary molecule present on another cell or ECM surface. The molecule to which it adheres is called ligand. Receptor-ligand pairs are often assembled in anchoring junctions. These junctions mediate biochemical and biophysical stimuli in cell-cell and cell-matrix interactions by causing cascades of biochemical reactions, which lead to precise regulation of cytoskeletal structure and cell adhesion forces.

1.2 The connective tissue

Several types of tissues are found in vertebrates[†]. A tissue is defined as a group of cells that performs similar functions. Four types of tissue exist in traditional classifications: epithelial, muscle, nervous and connective tissue. There is a large variety of different connective tissue types [7]. In general, connective tissues can be characterized by a high amount of ECM proteins and relatively low cell number when compared to e.g. epithelial tissues [8]. Connective tissues are an essential part in many organs like skin or tendon. Cells forming and building up the connective tissues are called fibroblasts.

Fibroblasts play an crucial role in producing and rearranging the ECM. This is important, since the biophysical and biochemical properties of connective tissues are dominated by the ECM. Examples of how fibroblasts are embedded within and interact with the ECM in connective tissues are presented in Figure 1.3. Here, two major aspects are to be mentioned. First, fibroblasts are featuring binding sites to the complex protein meshwork of the ECM in order to interact and rearrange it. Second, this rearrangement results into counterfort-like structures, which are most likely built to resist stresses and strains acting on the tissue. Consequently, cells have to respond to varying biochemical and biophysical properties of the ECM such as a certain range of elasticity and a large variety of structural characteristics of tissue building proteins. For example, bulk elasticity of human skin, which is

[†]Vertebrates are species featuring backbones.

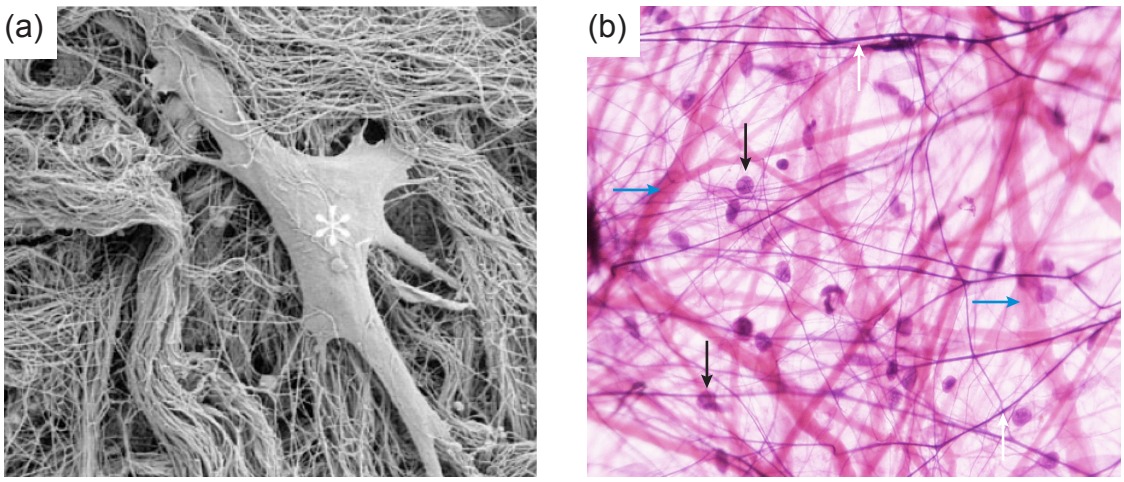

Figure 1.3: Architecture of the extracellular matrix *in vivo*. (a) A fibroblast (asterisk) is well connected to the dense collagen meshwork of the dermis. (b) Loose areolar connective tissue of mesentery, showing collagen fibers (blue arrows), elastic fibers (white arrows) and fibroblasts (recognizable by their nuclei, black arrows). The arrangement of fibers suggests stresses and strains acting on the tissue. Adapted from [9].

dominated by connective tissue, has been frequently investigated. It ranges between 20 kPa obtained from the dorsal side of the forearm and several MPa measured at the anterior part of the forearm [10]. To get a closer view on this processes, cellular adhesion and properties of the ECM will be discussed in the next chapters.

1.2.1 Extracellular matrix

The ECM is mainly composed of two classes of macromolecules. The first class is represented by glycosaminoglycans (GAGs), which are polysaccharide chains and the second class is represented by fibrous proteins. The members of the GAG family such as hyaluronan form a highly hydrated, gel-like substance in which the fibrous proteins are embedded.

Fibrous proteins can be separated into two major types: structural and adhesive proteins. Structural proteins like collagen and elastin are responsible for the biophysical properties of the ECM. Collagen fibers strengthen and help to organize the matrix, while elastin fibers provide its resilience. Adhesive proteins like fibronectin and laminin help directly to connect cells to the ECM. Fibronectin, for instance, promotes the attachment of fibroblasts and other cells to the matrix in connective tissues via the extracellular parts of some members of the integrin family. Most of the ECM proteins feature binding sites for another protein, which results in a very complex protein meshwork.

Collagens are the most abundant proteins found in animals, being the major protein comprising the ECM. They are synthesized by fibroblasts, which can also adhere to it via the integrin receptors [12]. As shown in Figure 1.4, collagen fibrils

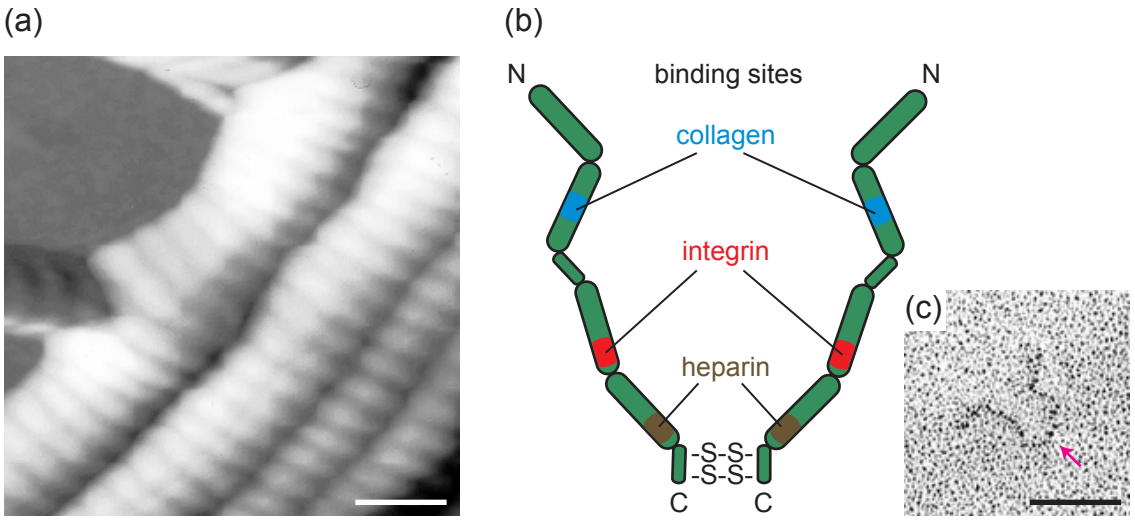

Figure 1.4: (a) Scanning probe micrograph of human collagen fibrils with characteristic banding of the protein surface. Scale bar 200 nm. Adapted from [11] (b) Scheme of the fibronectin molecules and selected binding sites. (c) Transmission electron micrograph of single fibronectin molecule. The pink arrow indicates the disulfide bonds. Scale bar 50 nm. Adapted from [1].

are long and thin rod-like structures, consisting of highly ordered bands with spacial period of approximately 67 nm [11].

Fibronectin is a large dimeric glycoprotein found in all vertebrates, composed of two subunits connected by disulfide bonds at one end (Fig. 1.4b). It is built up of multiple domains, each with specific binding sites for other matrix macromolecules and for specific CAMs like integrins. The integrin binding site is a specific peptide sequence consisting of three amino acids namely arginine, glycine and aspartate (RGD) [13]. It is a universal cell attachment site of various adhesive ECM and cell surface proteins [14]. Although RGD is a short aminoacid sequence it can compete with fibronectin for the binding site on cells, thereby inhibiting the attachment of the cells to a fibronectin matrix if available in solution. When coupled to a solid surface, RGD can promote cell adhesion to it [15].

1.3 Cell adhesion and environmental sensing

To assure functionality of particular organs and tissues, cells depend on interactions or communication between each other and the ECM. Surprisingly, cells use a relatively small set of molecular adhesion mechanisms to interact with their environment.

Basically, receptor-ligand interactions can be grouped into two types: homophilic and heterophilic interactions. Homophilic interactions are existent if ligand and receptor are identical molecules. In case of heterophilic interactions two different

molecules are associated into a stable bond. Within these interactions two principles exists in terms to control the strength of cellular bonds: affinity and valency regulation. Cells can regulate the affinity of the adhesion proteins by regulating their conformation. For example, structural changes in integrins, controlled by the short cytoplasmic tail domain can dramatically influence its binding ability [16]. By regulating the valency, cells can regulate the number of molecules involved in adhesion process. For instance, the diffusion into or out of the membrane area where interaction takes place can be controlled by the cytoskeleton [17].

There are five superfamilies of cell adhesion molecules: immunoglobulins, cadherins, selectins, mucins and integrins [18]. Immunoglobulins and cadherins mediate homophilic cell-cell interactions, but only cadherins are connected to the cellular cytoskeleton. Selectins play an important role in immune responses and are involved in leukocytes migration [19]. Integrins are transmembrane glycoproteins provide a physical linkage between the extracellular environment and the cytoskeleton. This linkage is essential for the stability of cell architecture, adhesion and migration and it enables integrins to directly transmit stress from the ECM to the cytoskeleton, and vice versa [20]. Integrin-mediated, i.e. force-dependent adhesion processes play an important role in the cellular sensing machinery. These processes (e.g. mechanosensing) are the focus of this work. Therefore, a closer look on biophysical and biochemical properties of the ECM and integrin receptors will be taken in this chapter.

1.3.1 Integrins

The CAM superfamily of integrins plays a key role in the stability of cell architecture, cell adhesion and migration. Its members are responsible for physical linkage between the extracellular environment and the cytoskeleton, which enables integrins to directly transmit stress from the ECM to the cell [21].

As shown in Figure 1.5, integrins are transmembrane, heterodimeric glycoproteins consisting of the so-called α and β subunits, which are associated by non-covalent interactions. Both subunits contain a large extracellular domain, a single transmembrane domain and a short cytoplasmic domain [22]. The β subunit is linked to the cytoskeleton by interacting with actin-binding proteins, such as vinculin and talin. All α subunits contain an extracellular structure known as β propeller, which is involved in affinity regulation. Together with the β subunit, this structure forms the ligand binding site.

Cells can regulate integrin activity by changing the affinity to specific ligands. Integrin activation involves a switchblade-like motion in which the interface between the headpiece and tailpiece is bent. In the inactive state, the integrin binding site is protected by the protein conformation and cannot be reached by ligands. In the active state, the α and the β subunits in the tail piece splay apart, thereby opening the switchblade and exposing the binding site to the ligands [16].

24 types of different integrin receptors are known. They are composed of a com-

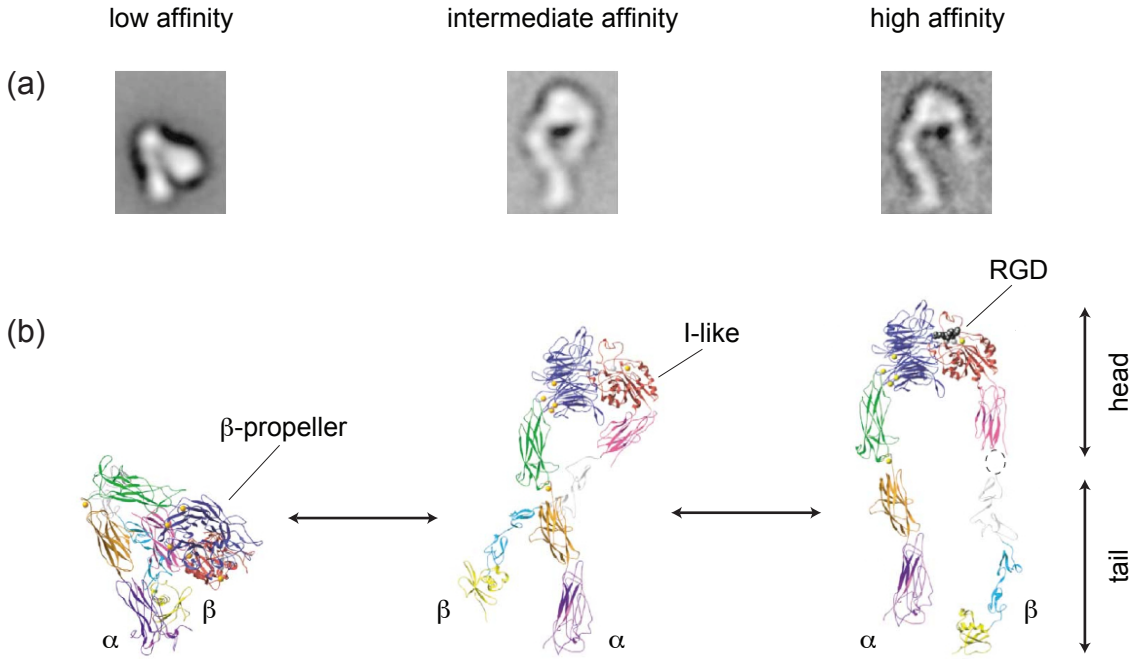

Figure 1.5: Global and local integrin conformational changes associated with affinity regulation. Electron micrographs (a) and ribbon diagrams (b). Bent conformation (low affinity), extended conformation with closed headpiece (intermediate affinity) and extended conformation with open headpiece (high affinity) is shown. Adapted from [16].

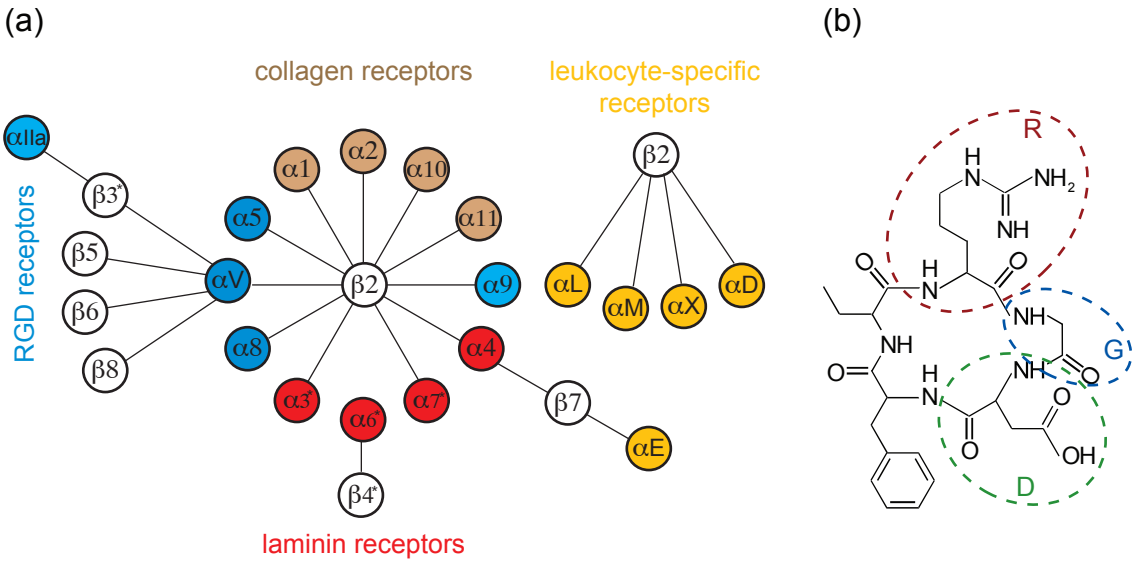

Figure 1.6: (a) The integrin family of cell-surface receptors. Adapted from [22]. (b) Molecular structure of the c(RGDfK) peptide used within this thesis. The cyclicly arranged aminoacids are arginine (R), glycine (G) and aspartate (D).

binations of eighteen different α and eight different β subunits. Each integrin type prefers a certain adhesion ligand in the extracellular matrix and binds to it with a particular affinity [22]. Figure 1.6 presents an overview of different integrin types and its subunit compositions.

As mentioned above, one prominent integrin binding protein found in the extracellular matrix is fibronectin. It contains the RGD sequence, that is, among others, a binding site for the $\alpha_V\beta_3$ integrins highly expressed by fibroblast, cells used in this thesis. Therefore, substrates presented in Part II are functionalized with the c(RGDfK) peptide to provide integrin mediated cell adhesion. The molecular structure of the c(RGDfK)[‡] is displayed in Figure 1.6b.

1.3.2 Focal adhesions

Cell-matrix interactions are mainly mediated by members of the integrin protein family. Since single or even multiple protein interactions are relatively weak, due to their non-covalent nature, cellular adhesions are formed in clusters [23]. By clustering many molecular bonds in one region, cells can increase their valency and significantly strengthened the adhesion by two mechanisms. First, the acting force can be distributed among the cluster constituents, so that the load on a single bond

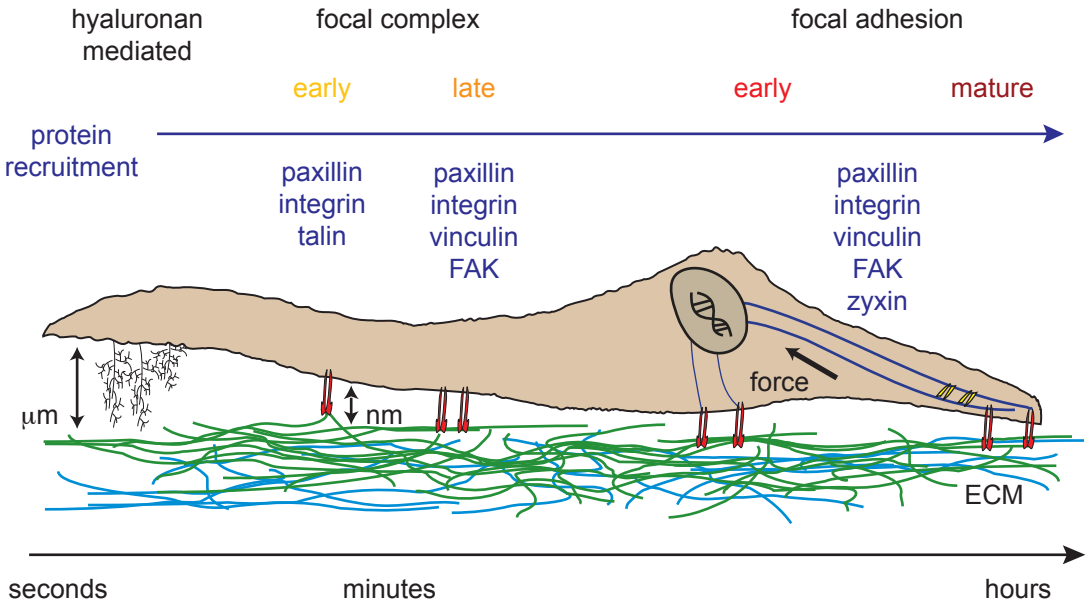

Figure 1.7: Time-dependent adhesion site formation. Within the first seconds of the adhesion process, hyaluronan mediated adhesion will be strengthened by integrin diffusing in early focal complex. Paxillin and talin will stabilize the late focal complex and connect early focal adhesion to the actomyosin stress fibers. Under action of force, maturation process of focal adhesions will proceed. Adapted from [24]

[‡]Kindly provided by Prof. Kessler, TU Munich, Germany

decreases, as well as its unbinding probability. Second, when a bond inside the cluster breaks, the rebinding probability of a single molecule within the cluster is high, since the region of possible receptor diffusion is spatially confined by the other bonds in the cluster. These adhesions sites are known under several names, such as focal contacts, focal adhesions, focal complexes and podosomes. They have a typical morphology and molecular composition and feature similar development phases [25].

The temporal development stages in focal adhesion formation are schematically presented in Figure 1.7. During this formation, the incorporation of different components is controlled by complex signaling pathways whose activation causes recruitment of different intra- and extracellular proteins.

The initial cell-matrix interactions are dominated by hyaluronan mediated events [26]. Within seconds or minutes, this interaction are replaced by integrin containing, dot-like adhesions termed focal complexes [27]. Earliest observed molecules in focal complexes are $\alpha_V\beta_3$ integrins, followed by talin and paxilin. Later, vinculin enters the developing focal adhesion, along with focal adhesion kinase (FAK). The compo-

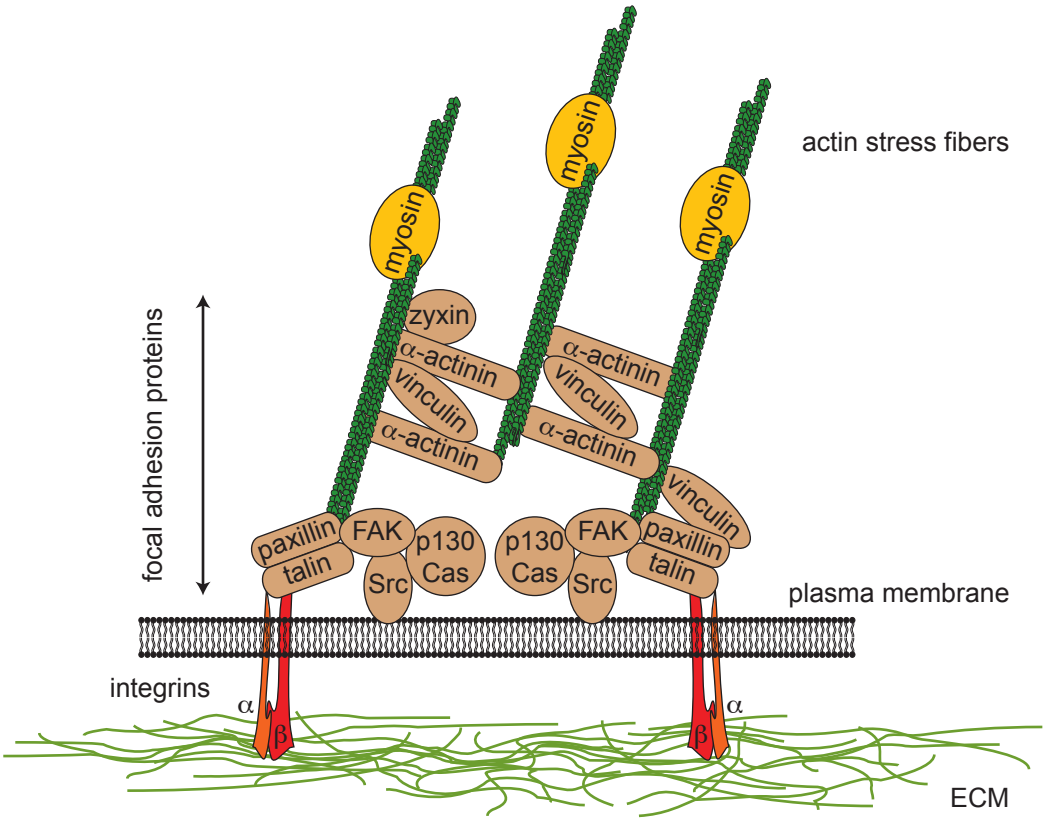

Figure 1.8: Focal adhesion at a glance. The integrin-binding proteins paxillin and talin recruit focal adhesion kinase (FAK) and vinculin to focal adhesions. α-actinin is a cytoskeletal protein that binds to vinculin and crosslinks actomyosin stress fibers and tethers them to focal adhesions. Adapted from [28].

sition of a focal adhesion in general depends on its maturation. However, zyxin is always absent from focal complexes [24]. Another mainspring is the force caused by actomyosin driven contractility. If this force is applied at the cell-matrix interaction sites, focal complexes will quickly develop into focal adhesions [29].

The aforementioned proteins, are allocated in the large complex on the intracellular side of the focal adhesion, and are called adaptor proteins. The entity of adaptor proteins is called focal adhesion plaque. Focal adhesion plaques are primarily involved in translating of forces from and into the cell and crucially affect cellular sensing behavior [30]. Figure 1.8 schematically summarizes important members of focal adhesion and their connections to the actomyosin fibers.

1.3.3 Environmental sensing through focal adhesions

The composition of focal adhesions, briefly introduced in the last chapter, is very complex. Along with integrins more than 100 adaptor and signaling proteins comprise its cytoplasmic domains [31]. Its biological activities are diverse and can control the organization of the attached cytoskeleton and a wide range of signaling molecules, such as kinases[§], phosphatases[¶] and their regulators. Focal adhesions have a primary role in sensing processes. Recent studies have established that at these sites, cells can not only sense the chemical properties of external surfaces (e.g. the presence of cell-matrix or cell-cell adhesion molecules), but also a variety of mechanical stimuli, such as forces and deformations [30, 32–34]. Two aspects of this complex sensing machinery are of great interest: the sensing of biochemical properties of cellular environment and the mechanosensing.

The biochemical properties of the ECM could be recognized by adherent cells. This recognition process is most likely mediated by integrin clustering events within focal adhesions related to the availability and structural arrangement of integrin binding sites [35]. As mentioned above, they are not randomly distributed rather arranged in a well controlled manner on ECM protein surfaces, similar to the 67 nm banding periodicity observed in collagen [11, 12].

Clustering of integrin receptors in cell-matrix interactions play an important role since it induces changes in integrin conformation, which provides binding sites for the intracellular components of focal adhesions (e.g. adaptor proteins). This triggers rearrangement of the cytoskeleton, phosphorylation of cytoskeletal proteins, activation of kinases and genomic responses [36, 37]. It was found, that cells are able to recognize even small changes in the binding site arrangement, when integring clustering was disturbed or changed under experimental conditions [15]. If binding site spacing of natural matrix proteins or RGD peptides is increased, cellular behaviour like spreading and migration as well as focal adhesion formation is dramatically affected [38–40]. One of the focal adhesion proteins, which is most likely

[§]Kinases are enzyms, which transfer phosphate groups from energy-donor molecules, ATPs, to specific (acceptor-)proteins. This process leads to activation of the acceptor-protein.

[¶]Phosphatases are proteins, that removes phosphate groups from proteins.

responsible for this cellular sensing property is talin, because of its confined size of approximately 70 nm [41] and its function as initiator of integrin clustering [42, 43].

A growing body of evidence suggests that mechanical sensing plays a crucial role in regulating cellular behavior, similar to chemical environmental cues (e.g. hormones) [44]. Mechanosensing, as the terminus may suggest, is not a unique property of cells in sensory organs. Rather it was found that may cell types (e.g. endothelial cells, fibroblasts, osteoblasts) probe external environment locally by applying actomyosin driven forces to cell-matrix and cell-cell adhesion sites [45]. In case of focal adhesions, they act as cellular mechanosensors that respond to changes in applied force by assembly and disassembly [20]. Variety of functional mechanosensing models were suggested in the past [46–48]. Two basic physical principles should be mentioned here.

One assumption is that focal adhesions contain special molecular switches represened by multi modular proteins. Under application of force they react by changing their state from inactive to active and vice versa [49]. Such a mechanism could be based on stress induced conformation transition of some focal adhesion associated proteins or of modulation activity of specific enzymes.

Another view on mechanosensitivity proposes, that mechanosensor switch is triggered by local elastic strain [46, 50]. Within this theory focal adhesion can be thought as a two layer structure, where the lower layer is represened by integrins and the upper by focal adhesion plaque. Since the lower layer is attached to the ECM, force applied by the cell on the upper layer will cause compression resulting in higher affinity for the plaque proteins.

Manifold experimental data suggests that protein tyrosin kinases such as FAK, Src or Fyn are involved in mechnotransduction[‖] [51–53]. Adaptor proteins such as paxillin, p130Cas [54] and talin [55] as well as zyxin most likely play a role in the cellular response to mechanical stress. We will now consider one example of Fyn regulated phosphorylation in force- and position-dependent mechanism of rigidity sensing [56]. It was proposed, that the binding to the ECM could initiate the assembly of two different complexes within the cell. One is linked to the cytoskeleton by a phosphorylatable linker and, via integrins, to the ECM. This linker serves as the mechanosensor. Another complex is linked to a separate extracellular site. As shown in Figure 1.9 the first complex can move under applied force, wheres the second remain stationary. When cells apply force on the first complex, the rigidity of the ECM will determine its displacement and whether the force will be sufficient to change the linker conformation in terms to expose cryptic peptide sequences. Its subsequent phosphorylation leads to an activation of signaling pathways. On soft substrates the separation will be to large and might be sufficient to prevent the sensor from interacting with the stationary complex. This force dependent mechanism is generally based on comparison, done by the cell, between the cellular elasticity and the elasticity of the surrounding environment [57].

[‖]Mechanotransduction is defined as translation of mechanical stimuli into biochemical signals.

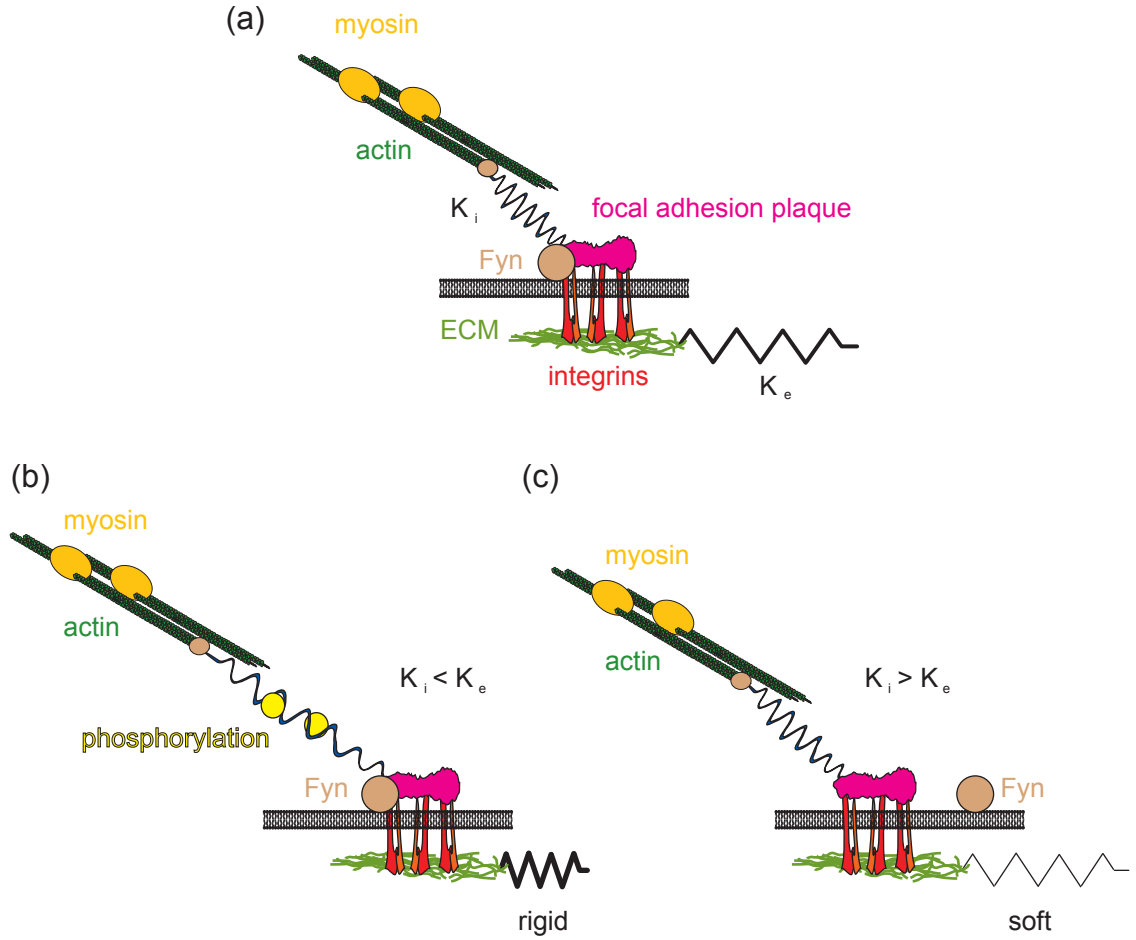

Figure 1.9: Position- and force-dependent mechanism of rigidity sensing. Stretchable linker protein (here represented by its elastic modulus K_i) between focal adhesion plaque and stress fibers can move, due to forces generated by the cell, relatively to the phosphorylating Fyn kinase. (a) In the resting state the matrix elasticity K_e can not be determined. (b) Rigid surface ($K_i < K_e$), acting forces will stretch the linker and enable phosphorylation by the Fyn kinase. (c) Soft surface ($K_i > K_e$), Partially stretched linker can not be phosphorylated due to the large displacement. Adapted from [57].

Since biomechanical properties of the cell itself play an important role in environmental sensing, simple biophysical models, which describe the cell as a physical body, will be introduced in the next chapter.

Chapter

2

Cells as biophysical model

Biological tissues in general, and cells in particular, are very complex polymer-based materials by biophysical means. Moreover, their behavior is dominated by active, adaptive reactions to the changing surrounding conditions. For example it is universally known that widely investigated cell adhesion consists of various intracellular actions, which are simultaneously dominated by contraction, bond formation and receptor-ligand cooperativity [44]. In this chapter basic physical models for viscoelastic behavior of biological, thus polymeric materials and general adhesion principles will be described.

2.1 Viscoelastic models

A distinctive feature of the mechanical behavior of nearly all common (e.b. biological) materials is the way in which they respond to an applied stress or strain. It usually depends on the rate or time period of applied loading. This dependence can be assumed to approximate a state between elastic solids and viscous liquids. Biological materials are therefore termed viscoelastic as they display aspects of both (viscous and elastic) types of behavior. Deformation of this materials can be described by a combination of Hooke's law

$$\sigma = E_Y \epsilon \tag{2.1}$$

or

$$\frac{d\sigma}{dt} = E_Y \frac{d\epsilon}{dt}, \tag{2.2}$$

where σ is the applied stress and ϵ the resulting strain on the material according to the Young modulus E_Y, and Newton's law

$$\sigma = \eta \frac{d\epsilon}{dt}, \tag{2.3}$$

where η is the viscosity and $d\epsilon/dt$ the strain rate. These relations are linear approximations of the stress σ_{ij} and strain ϵ_{ij} tensors and correspond to two basic

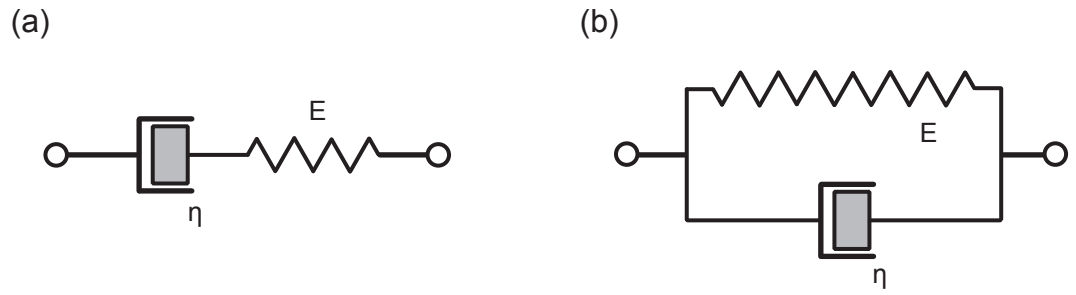

Figure 2.1: Mechanical models to represent the viscoelastic behavior of biological materials. (a) Maxwell model, (b) Kelvin model. The springs and dashpots are represented by their elasticity E and viscosity η, respectively.

components, an elastic spring of modulus E^* and a viscous dashpot of viscosity η. These components are used in various combinations in different models which describe viscoelastic behavior of biological materials, and of cells in particular [58, 59]. Figure 2.1 represents two simple models the so-called Maxwell and the Kelvin model. The Maxwell model describes primarily Newtonian fluids and flows. It consists of a spring and a dashpot in series. Under action of an uniform stress σ an overall strain ϵ occurs in the system where

$$\sigma = \sigma_1 = \sigma_2 \tag{2.4}$$

and

$$\epsilon = \epsilon_1 + \epsilon_2. \tag{2.5}$$

Including equations (2.2) and (2.3) and differentiating of equation (2.5) gives for the Maxwell model:

$$\frac{d\epsilon}{dt} = \frac{1}{E}\frac{d\sigma}{dt} + \frac{\sigma}{\eta}. \tag{2.6}$$

In the case of constant strain $\epsilon = \epsilon_0$ equation (2.6) can be readily integrated and predicts an exponential decay of the stress, thus relaxation of the material

$$\sigma = \sigma_0 e^{-t/\tau_0} \tag{2.7}$$

with the characteristic relaxation time $\tau_0 = \eta/E$.

The Kelvin model consists of the same elements as the Maxwell model, but connected in a parallel manner. This arrangement of spring and dashpot means that the strain is uniform:

$$\epsilon = \epsilon_1 = \epsilon_2 \tag{2.8}$$

and the stress in each component summarizes into overall stress such that

$$\sigma = \sigma_1 + \sigma_2 \tag{2.9}$$

*In this chapter the Young modulus E_Y will be annotated as simple spring modulus E.

The individual stress can be obtained from equations (2.1) and (2.3) for the spring and the dashpot respectively. With the equation (2.9) the Kelvin model can be described as:

$$\frac{d\epsilon}{dt} = \frac{\sigma}{\eta} - E\frac{\epsilon}{\eta} \tag{2.10}$$

Under a constant stress $\sigma = \sigma_0$ the differential equation has a simple solution

$$\epsilon = J(t)\sigma, \tag{2.11}$$

where $J(t)$ is the so-called creep compliance function. In detail it is

$$\epsilon = \frac{\sigma_0}{E}\left(1 - e^{-t/\tau_0}\right) \tag{2.12}$$

with the characteristic relaxation time $\tau_0 = \eta/E$.

The creep and relaxation behavior of both models is shown in Figure 2.2. The creep and the relaxation functions generally characterize the viscoelastic properties of the investigated materials. The creep function $J(t)$ describes the development of the material strain during the application of a constant stress. Unlike the relaxation function, which describes changes in the tensile or compressive stress, while a constant strain is applied.

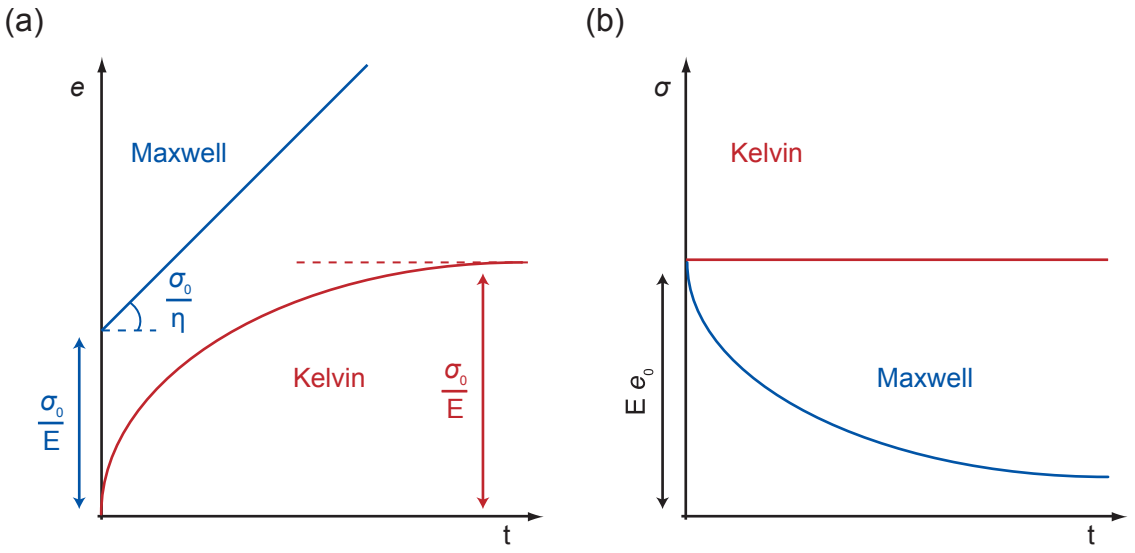

Figure 2.2: The behaviour of the Maxwell and Kelvin models during different types of loading. Creep (constant stress) (a) and relaxation (constant strain) (b).

During recent years, different approaches were followed for describing the cell as a viscoelastic material. Unfortunately, only for certain simplified experimental situations, models have been well established. For example, the extended Kelvin model is often favored if cells are well-adhered at two opposing surfaces in micromanipulation, e.g. single cell force spectroscopy (SCFS) approaches † [60, 61].

†Single cell force spectroscopy, was applied during experiments described in Chapter 7

2.2 Theory of adhesion and mechanosensing

The complex regulatory machinery within biological tissues (e.g. cell-tissue and cell-cell interactions) as described in Chapter 1.3.3 is mainly based on adhesion processes. In these specific interactions of proteins, sugars or lipids, numerous receptor ligand pairs are involved. George I. Bell pointed out in the late '70s the specific nature of cell adhesion. He realized that the nonspecific electrostatic interactions between cell membranes cannot be responsible for the strong forces acting between cells. Instead, these forces were suggested to be mediated by specific biological bonds [62]. This binding mechanism differs greatly from covalent chemical bonds. It is mainly mediated through small free energy changes in electrostatic, van der Waals and relatively strong hydrogen bond interactions at the receptor-ligand interface. These bonds are reversible and feature binding energies of the same order of magnitude as the thermal energy. For example, one of the strongest biological bonds is the avidin-biotin bond with the binding energy of about 35 k_BT [63]. The competition of binding with thermal energy leads to a finite bond lifetime and a stochastic decay of adhesion which can be influenced by the application of force as will be discussed in the next chapter. Moreover, single receptor-ligand pairs can associate in clusters and so stabilize the adhesion site due to the so-called cooperativity effects. Thus, cells are able to apply strong forces to their environment and sense actively the mechanical properties of their surroundings via adhesion-dependent processes called mechanosensing.

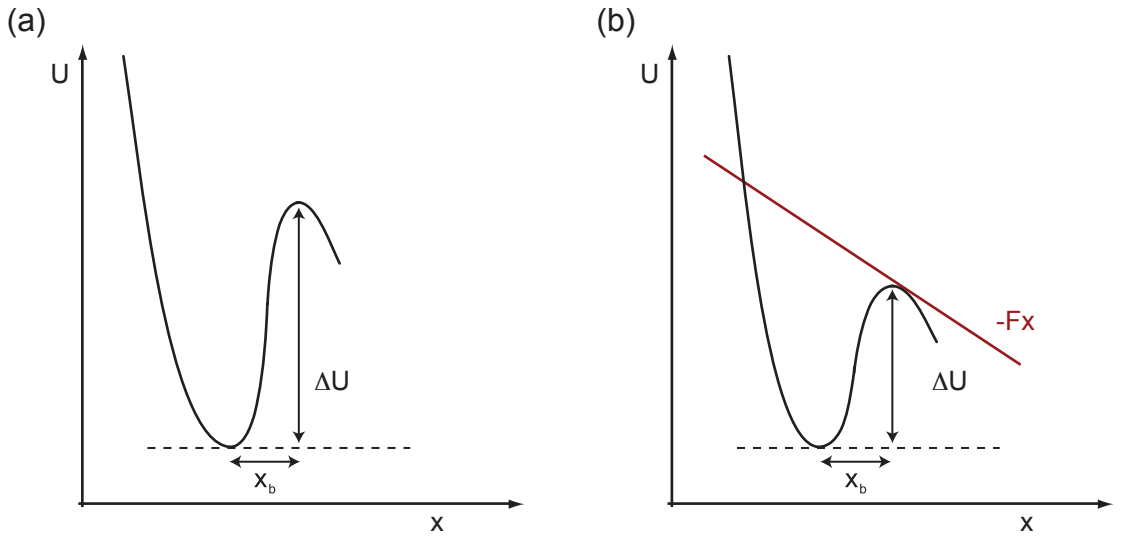

Figure 2.3: Model for a one-dimensional binding potential with a single transition barrier (a), external force decrease the effective potential barrier ΔU (b).

2.2.1 Adhesion concepts

To describe a thermodynamically induced breakage of bonds the theory of Kramers can be applied [64]. Here the receptor-ligand interaction is governed by an attractive potential with the transition state barrier ΔU as shown in Figure 2.3. The intrinsic (unstressed) dissociation of a single bond can be related to a rapture rate k_0, which is the inverse of the average transition time over the barrier. Application of force F leads to a tilt in the effective potential well and finally in bond rupture. This rupture is related to the force depended dissociation, or off-rate k_{off} which increases exponentially as a function of the external force [65]. The so-called Bell's equation is given by

$$k_{off} = k_o e^{F/F_b} \tag{2.13}$$

were $F_b = k_B T/x_b$ is the internal force scale set by the thermal energy $k_B T$ and the distance x_b between the potential minimum and transition state barrier. The scale of F_b lies in the range of several pN for typical values $x_b \approx 1$ nm and $T \approx 300$ K.

In practice, bond rupture forces are stochastically distributed around most frequent rupture force F^*. Moreover, under experimental conditions forces are applied by probes and depend therefore on the probe stiffness s and velocity v. This results in rupture force dependence on the so-called loading rate

$$r = dF/dt = v \cdot s \tag{2.14}$$

which leads to the increase of most frequent rupture force according to:

$$F^* = F_b \; ln\left(\frac{r}{k_{off} F_b}\right) \tag{2.15}$$

The theoretical basis for the dependence of unbinding force on the loading rate was derived in the late 90s [65] and was frequently verified by dynamic force spectroscopy (DFS) measurements [66–69]. An example is shown in Figure 2.4. Here, single molecule interactions of leukocyte function-associated antigen-1 (LFA-1) and intercellular adhesion molecules-1 and -2 (ICAM-1 and ICAM-2) were measured by DFS. LFA-1 belongs to the large protein family of integrins ($\alpha_L\beta_2$), and is of high interest since integrin mediated cell adhesion is in focus of this work. Following equation (2.15) the unbinding force is indeed dependent on the loading rate. It increases by more than of two orders of magnitude acquired at a loading rate range covering three orders of magnitude. The force spectra (unbinding force versus loading rate) revealed two linear regimes for the dependence of the unbinding force on the logarithm of loading rate. A fast loading regime and a slow loading regime, which correspond to a particular transition state barrier. Two-well binding potentials seems to be characteristic for the integrins as also shown by studies of fibronectin-$\alpha_5\beta_1$ integrin interactions [70].

In nature, single bonds are the exception and their relevance in biological systems is restricted to very small regions and short time scales. The more relevant situation is that the interaction happens via clusters, meaning that many molecules are

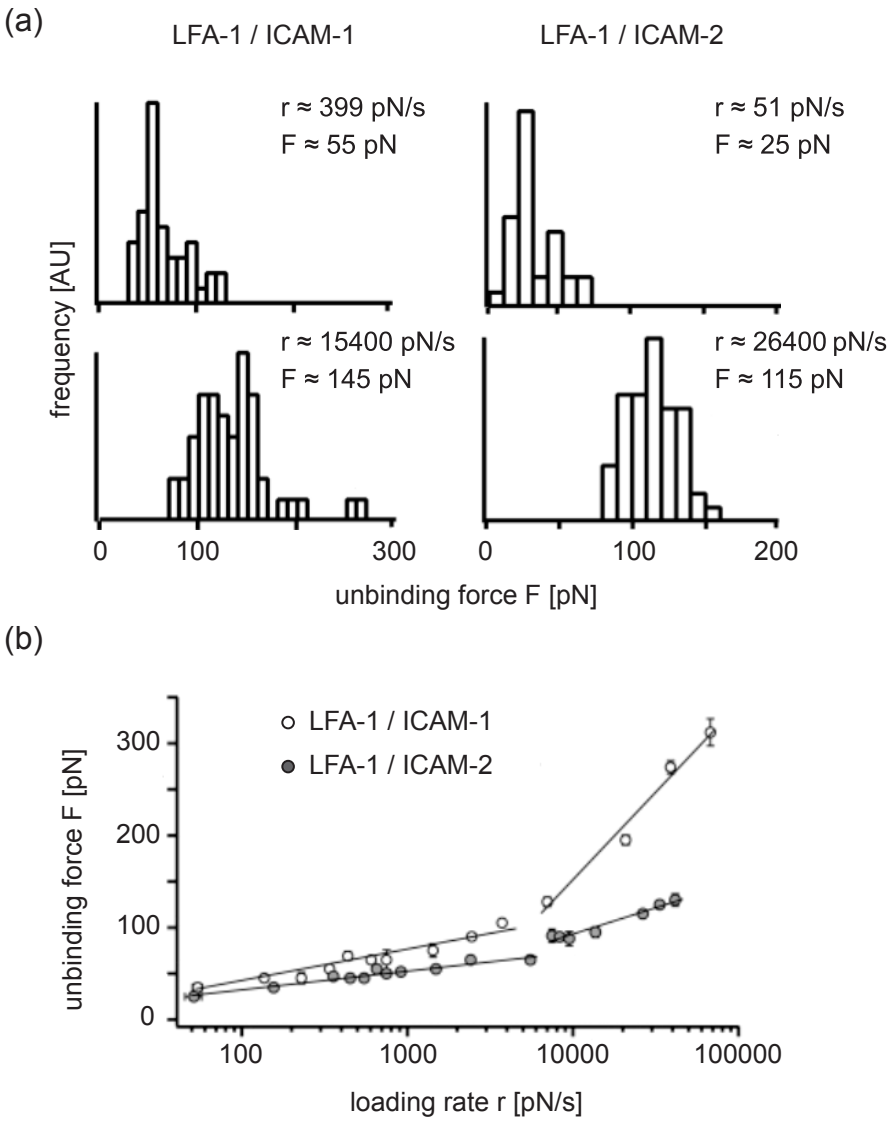

Figure 2.4: Dynamic force spectroscopy (DFS) reveals the dependence of unbinding forces F on loading rate r. (a) Examples of histograms of individual unbinding forces originating from LFA-1/ICAM-1 and LFA-1/ICAM-2 interactions respectively. (b) Two transition barriers were obtained for the integrin-ICAM interaction. Adapted from [69].

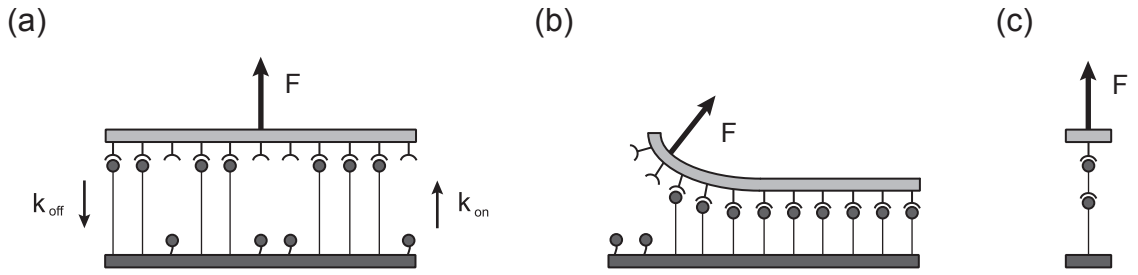

Figure 2.5: Schematic visualization of molecular bonds in different adhesion clusters. (a) Parallel loading, there are $N_t = 11$ clustered receptor-ligand pairs, of which $i =$ are closed and equally share the constant force F. Single bond rupture with dissociation rate k_{off} and rebind with association rate k_{on}. (b) In the zipper system one bond is loaded after another. (c) In the case of serial loading, all bonds are exposed to the same force.

involved and therefore the manifold case must be considered. As shown in Figure 2.5, forces applied to these multiple bonds can act in different configurations. Serial loading occurs in multiple protein binding, here all bonds are exposed to the same force. In biological context, the most known example of zipper like loading occurs in the case of DNA where proteins unzip the double strands in single strands [71]. In the case of parallel loading the force is homogeneously distributed over all closed bonds within the cluster. Focal adhesions are assumed to be arranged in a parallel configuration. They play an important role in cellular adhesion, migration and sensing processes. Therefore, theoretical models were developed to study the dynamics and growth of parallel bonds under shared constant force [50, 72, 73]. A brief description of the deterministic model developed by Bell later modified by Erdmann and Schwarz to investigate the effect of stochastic fluctuations, will follow [62, 73]. As shown in Figure 2.5a the model assumes that constant number of N_t receptor-ligand bonds are clustered on opposite surfaces. One surface acts as a rigid transducer and distributes the constant force F homogeneously over the array of bonds. At each time $\tau = k_0 t$, i bonds are closed and $N_t - i$ bonds are open. Closed bonds rupture as described by equation (2.13), but scaled by the factor i due to the equally shared force F over all closed bonds

$$k_{off} = k_o e^{F/iF_b}. \tag{2.16}$$

Open bonds are assumed to rebind with the force independent rate k_{on}. This model has three dimensionless parameters: cluster size N_t, total force $f = F/F_b$ and rebinding rate $\gamma = k_{on}/k_{off}$. While the external force destabilizes the cluster, rebinding stabilizes it. The mean number of closed bonds $N(\tau) = \langle i \rangle$ was investigated in terms of stability, thus the evolution of $\dot{N} = dN/d\tau$ as a function of N. It was found, that if the acting force F is higher as the critical force $F_c = f_c F_b$ ($f > f_c$) a positive feedback effect exist for bond rupture, which can not be balanced anymore by rebinding effects. At $f < f_c$ two fixpoints ($\dot{N} = 0$) exist, with lower being stable and upper

being unstable. At $f = f_c$ both fixpoints collapse in a saddle-node bifurcation[‡]. At this point the critical force can be calculated exactly. For no rebinding ($\gamma < 1$) the critical force

$$f_c \approx \gamma N_t / e \tag{2.17}$$

disappears with γ because the cluster decays by itself with no rebinding. If rebinding is involved ($\gamma > 1$) weak dependence on γ can be observed

$$f_c \approx \frac{N_t ln\gamma}{2} = F_c/F_b \qquad \Rightarrow \qquad F_c \approx F_b \frac{N_t ln\gamma}{2} \tag{2.18}$$

and implies that the internal, single bond force scale F_b also determines the cluster dissociation force.

This analysis shows that an external force can switch the stability of an adhesion cluster if it is close to critical state. Therefore, small changes in cytoskeletal loading result in high cluster loading and larger force, acting on the participating single bonds. This may be necessary for triggering signaling events and regulating focal adhesions growth.

2.2.2 Physical model of mechanosensing

The development of strong adhesion bonds is the first step in a mechanosensing process. Within this process cells apply forces to their environment and, depending on response, measure the elastic properties, thus the spring constant of their surrounding. Models for biomolecular bonds were recently introduced as a principle how the intracellular force generation and the extracellular elasticity could be coupled [74, 75]. A brief description of the so-called two spring model, developed by Schwarz et al. is depicted schematically in Figure 2.6. The model describes two

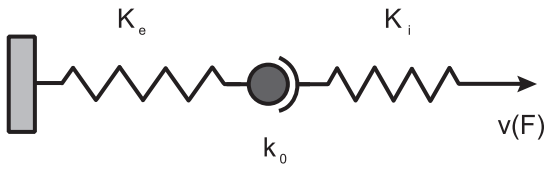

Figure 2.6: Mechanosensor as a biophysical model. The elasticity of the cellular environment is represented by the spring constant K_e, whereas the mechanical properties of the force transducer e.g. intracellular structures are represented by the spring constant K_i. The two spring model is adapted from [48]. Here, the transmembrane biomolecular bond (focal adhesion) opens in a stochastic manner with dissociation rate k_0. Forces generated by the actomyosin filaments were taken into account by the linearized force-velocity relation $v(F)$.

[‡]Bifurcation occurs when a small change made to the parameter of a dynamic system leads to a sudden appearance of a qualitatively different change in its behavior.

springs acting in series, which represents the elasticity of the extracellular matrix K_e and the force generating intracellular structures K_i. They are connected by a biomolecular bond, which opens in a stochastic manner with the dissociation rate k_0. The effective spring constant of the whole system is given by

$$\frac{1}{K} = \frac{1}{K_e} + \frac{1}{K_i} \tag{2.19}$$

due to the serial nature of the applied force. This leads to the determination of the effective spring constant of the system by the softer spring. Since the tension within the intracellular force generating structures is driven by the displacement of molecular motors (e.g. myosin II) it is represented by the force-velocity relationship

$$v(F) = v_0 \left(1 - \frac{F}{F_c}\right) \tag{2.20}$$

with the molecular motor velocity v and critical, stall force F_c. During the force generation the spring becomes strained and stores the energy $W = F^2/2K$, which results, in the case of a dynamic situation, in $dW/dF = F/K$. The power invested by the cell into the cytoskeleton, thus spring contraction according to the equation (2.20) is given by:

$$\frac{dW}{dt} = \frac{F}{K}\frac{dF}{dt} = F \cdot v(F). \tag{2.21}$$

Integration of equation (2.21) leads to:

$$F(t) = F_c \left(1 - e^{-t/t_k}\right), \tag{2.22}$$

where the typical time scale is given by $t_k = F_c/v_0K$. As suggested by Bell [62] the average bond life time T is the reciprocal off-rate of the bond of interest

$$T = \frac{1}{k_{off}} = \frac{1}{k_0} e^{-F_c/F_b}. \tag{2.23}$$

Under the assumption of constant elasticity of the acting intracellular structures K_i and according to equations (2.22) and (2.23) the typical time scale of force transduction will be lower that the average bond life time ($t_k < T$) in the case of stiff surrounding, thus large K. Here, the bond effectively senses the constant loading with the stall force F_c. If the environmental conditions are rather soft, i.e. K is small, the loading is approximately linear with the loading rate F_c/t_k. In this case, the typical time scale of force transduction is higher than the average bond life time ($t_k > T$), which results in a bond decay with intrinsic rate k_0 before the effect of force becomes relevant.

The presented model describes schematically the active mechanosensing of cells [76, 77]. Forces applied by the cells are transduced to their surroundings via focal adhesions. As discussed in Chapter 2.2.1 they should be exposed to certain amount

of force required for the activation of relevant signaling pathways. Only those adhesions reach this amount of force which experience the adequate local stiffness in their environment. Polarization of cells towards stiffer environments on anisotropic compliant substrates has been observed experimentally [77], which is in good agreement with the model presented above [76, 78].

Chapter

3

Motivation and objective

In the previous part of this thesis a brief overview of the structure and complexity of biological, cell based, systems was given. Due to their complexity, these systems must feature a high level of communication between single structural members i.e. cells. In general, communication as a process anticipates continuous sensing of surrounding environment, i.e. probing of biochemical and biophysical properties of the ECM in which the cells are embedded. Understanding the interactions of cells with the ECM is an essential step towards the understanding of the mechanical and chemical cohesion of tissues.

Two types of introduced sensing mechanisms seems to crucially affect cellular behavior:

- Mechanosensing
- Sensing of available binding site spacing and density

Both processes were investigated in the past by numerous approaches. In the case of mechanosensing, elastic, deformable substrates were employed to visualize and quantify forces applied by the cells on their surrounding [45, 79, 80]. On the other hand, soft substrates were used to quantify cellular tactile set points of rigidity sensing [81–83]. Thereby, numerous proteins and signaling pathways were identified to be involved in mechanosensing processes [29, 30, 34, 44, 57, 84, 85]. Moreover, different models and concepts were introduced to provide biophysical mechanisms of mechanosensing [46, 48, 56, 86].

In the case of binding site availability, different micro and nanostructured substrates were developed to quantify cell adhesion and cell spreading behavior, as well as cell spreading geometries [35, 39, 40, 87]. Also, effects on aforementioned cellular properties were investigated by varying protein concentration on the substrate surface [38, 88]. These findings were supported by biophysical models [73, 74].

The common disadvantage of the reviewed approaches, otherwise impressive, is that only one environmental signal, sensed by the cells, is tunable. The reason for this is, most likely, a lack of appropriate substrate systems with multi-dimensional

parameter spaces. Recently, new approaches were introduced, where both, biochemical and biophysical parameter were adjustable. Here, synthetic, compliant substrates were coated with different collagen concentrations and soft collagen gels were used to change environmental stimuli [89]. It was the first step towards better ECM analogs, but these parameters could not be varied independently enough from each other, and, in the case of binding site spacing and density, not with desirable precision (on nm scale). As prove of principle, another approach was introduced, where synthetic substrates were used as an elastic support for decoration with extended gold nanoarrays [90].

In the life science community, there is a large agreement about the importance of crosstalk of environmental stimuli on cellular behavior [31, 91, 92] and therefore a high demand for tunable substrate exists in this field.
Hence, two major objectives of this thesis were defined:

- Development of a substrate system with simultaneously and independently tunable biophysical and biochemical properties, based on poly(ethylene glycol)-diacrylate (PEG-DA) and block copolymer micelle nanolithography (BCMN).
- Quantification of cellular responses on such defined two-dimensional space of environmental parameters.

The intra- and extracellular signaling, caused by cell-matrix interactions, is a crucial aspect in the development of all adherent cells like fibroblasts and endothelial cells. Thus, fibroblasts were selected to serve as a cellular model system. Inhibition of cell-matrix interactions results in apoptosis (programmed cell death) [93]. Moreover, a strong relation between cell growth and viability has been found. Inhibition of cell growth, i.e. limitation of the cell spreading area also results in programmed cell death [87]. Therefore, cell spreading area and development of cell matrix adhesion, thus cell-matrix adhesion strength are important indicators of cellular development and tissue forming processes. Hence, these were chosen as signals to be measured during the experiments presented here.

Part II

Material and Methods

Chapter

4

Nanopatterned PEG-DA hydrogels as ECM analog

As described in 1.3.3 biomechanical and biochemical properties of cellular surroundings play a key role in cell-tissue interaction such as development, cell migration and proliferation, wound healing, etc. In this chapter, fabrication principle of substrates developed and used in this thesis will be described. The substrate system was designed in a way that allowed to tune their biophysical and biochemical properties simultaneously.

The main goal was to produce an artificial analog of the extracellular matrix (ECM). Therefore, it must be clarified what kind of ECM properties are of particular interest. Since cellular adhesion and mechanosensing capabilities are in focus of investigations, two major parameter should be controlled, the number of available adhesion ligands and elastic modulus (E_Y) of supporting substrate. As described above, the dimensions of transmembrane proteins responsible for adhesion processes e.g. $\alpha_V\beta_3$ integrins are in the range of several nanometers [94]. Coevally, it was shown that the availability of the integrin binding ligands, i.e. amino acid sequences, is periodically distributed on the surface of ECM building proteins. This periodicity ranges within several tens on nanometers [11]. Consequently, the spacing (ΔL) of anchor points for ligand immobilization on the surface of desired substrate system should be tunable between tens and hundreds of nanometers. Moreover, the size of anchor points itself should not exceed a limit of about 10 nm to assure single protein-ligand interaction. Concerning mechanical properties of desired substrates, a wide range of elastic moduli found in different tissues are to consider. They range from very low, nearly liquid 0.1 kPa to, for biological terms, hard 100 kPa [82]. These requirements were achieved by two approaches: block copolymer micelle nanolitography (BCMN) and transfer lithography based on poly(ethylene glycol)-diacrylate (PEG-DA) polymerization into hydrogel substrates.

4.1 Block copolymer micelle nanolithography

A key issue in the fabrication of functional nanostructures is the defined placement of nanometer-sized objects in periodic or aperiodic arrangements on surfaces of interest. Self-assembly techniques such as BCMN provide a hands-off method to small-scale structuring of periodic patterns or structures where nanometer-sized objects are separated by nanoscopic length scales [95]. Within this thesis, BCMN was used to fabricate extended gold nanopatterns on solid inorganic supports. Particle size of gold nanoclusters and interparticle spacing are tunable depending on experimental conditions. For fabrication details see Chapter 4.3.

4.1.1 Preparation of nanopatterned surfaces

Block copolymers, especially those consisting of two covalently bound polymer chains featuring different chemical properties, are called diblock copolymers. Their shape and size are easy to vary within the desired length scale by changing the molecular weight and composition of building blocks. Here, amphiphilic characteristics of macromolecules consisting of non-polar poly(styrene) (PS) and polar poly(vinyl pyridine) (PVP) units featuring macromolecules (PS-*b*-PVP) are used to induce aggregation to uniform inverted micelles in organic, non-polar solvents.

Table 4.1: Properties of used diblock-copolymers.

polymer PS(g/mol)-*b*-PVP(g/mol)	PS units	PVP units	PDI[a] M_W/M_n
PS(25000)-*b*-PVP(15000)	240	143	1.04
PS(47000)-*b*-PVP(24000)	451	228	1.07
PS(110000)-*b*-PVP(52000)	1056	495	1.15
PS(190000)-*b*-PVP(55000)	1824	523	1.10

[a]The polydispersity index (PDI) is the weight average molecular weight divided by the number average molecular weight. It indicates the distribution of individual molecular masses in a batch of polymers.

As shown in Figure 4.1d PS-blocks form a shell around the less soluble PVP blocks to reduce energetically unfavorable interactions with the solvent [96]. The formation of micelles starts above the so called critical micelle concentration (CMC) of diblock copolymer chains in the solution. Further increase of the PS-*b*-PVP concentration above the CMC does not affect the number of dissolved free polymer chains but strongly increases the number of micelles [97]. The diameter of micelles is controlled by the molecular weight of the block copolymers and the interactions between the polymer blocks and the blocks with the solvent. The polar PVP core can be used to incorporate metal precursor salts such as tetrachloroauric(III) acid ($HAuCl_4$) into

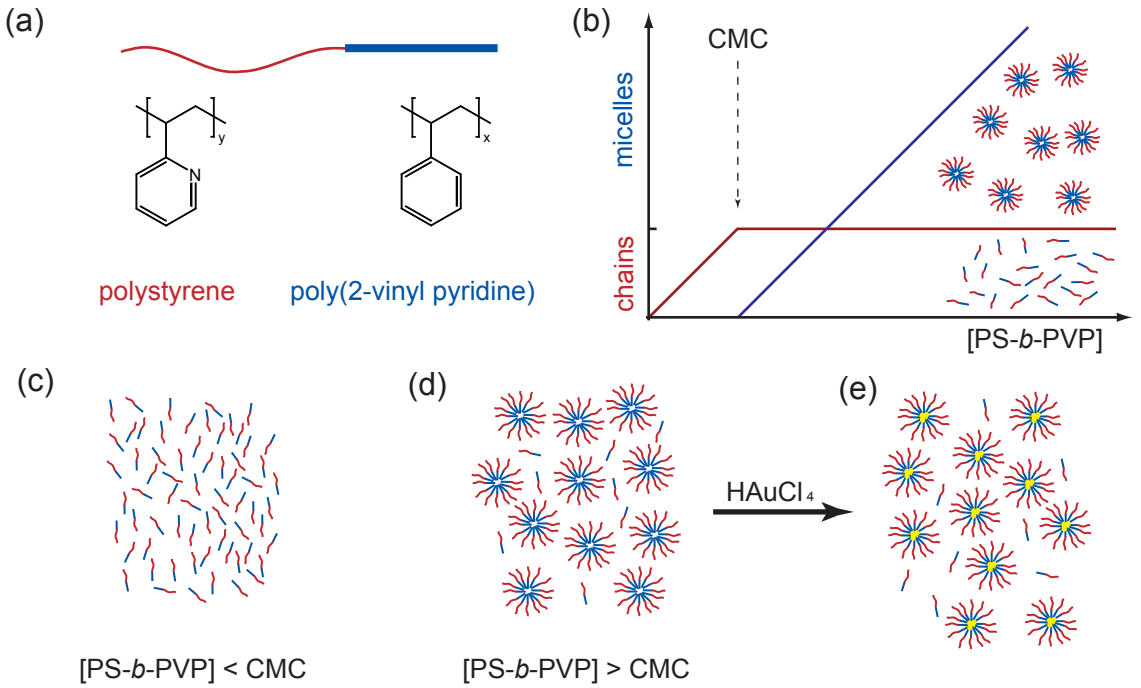

Figure 4.1: (a) The diblock copolymer consists of one hydrophobic polystyrene (PS) and one hydrophilic poly(vinylpyridine) (PVP) block (PS-*b*-PVP). (b) - (d) In organic non-polar solvents, micelle formation starts at critical micelle concentration level (CMC) with increasing concentration of free PS-*b*-PVP chains in a solution. Above the CMC only a constant number of molecules are in the free state. (e) After the addition of metal precursor into the micellar solution (here $HAuCl_4$) it is incorporated into the core of the micelle.

the micelle. This loading can be quantified according to equation (4.1).

$$L = \frac{n[HAuCL_4]VP}{mVP}. \tag{4.1}$$

Here, the loading parameter L is a theoretical measure of the nominal number of precursor salt molecules per vinyl-pyridine (VP) unit. It is defined as the ratio of neutralized VP units (n) and the total number of VP units (m). The incorporation of metal precursor salt into the core of micelles shifts the thermodynamic equilibrium between free polymer chains and assembled micelles towards the latter and decreases the CMC at the same time [98]. The properties of PS-*b*-PVP macromolecules utilized in this work are presented in Table 4.1.

The placement and well-ordered arrangement of the micelles on the solid, inorganic support is the next step of the fabrication procedure and is summarized in Figure 4.2. The self-assembly process of micellar organization was initialized via dip-coating where clean glass or silicon slides are immersed into the micellar solution. There, the micelles do not adsorb onto the surface. The arrangement of the micelles on the substrate surface occurs only during the retraction process at

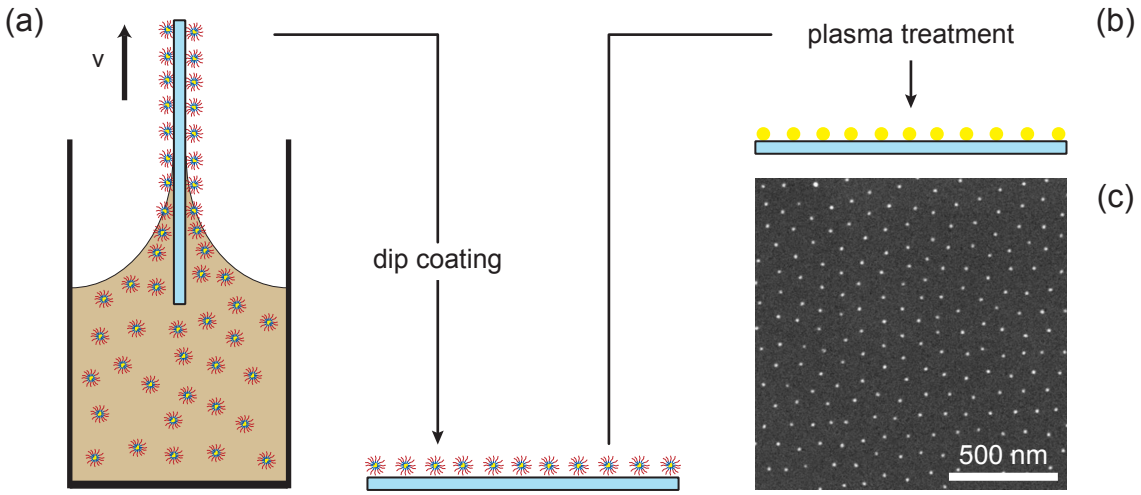

Figure 4.2: (a) Dip-coating of cleaned solid supports (e.g. glass or silicon slips) induce self organization that leads to the formation of quasi hexagonally ordered PS-*b*-PVP micelle array. Retraction velocity v is a crucial parameter to control intermicellar distances. (b) Reactive plasma treatment induces removal of the polymer and reduction of gold salt to gold nanoparticles. (c) Example of scanning electron micrograph of extended Au nanoparticle array featuring interparticle distance of 100 nm.

the air-solvent-substrate interface. The retraction velocity v or velocity gradient $v(t)$ is controlled by a stepping motor driven device*. The key event responsible for the quality of resulting structures, in terms to control their spacing and order, is the evaporation of the solvent at the air-solvent-substrate interface. It strongly affects the formation of the micelle containing film and the resulting attractive and repulsive, electrostatic and steric forces. The resulting quasi hexagonally packed arrangement of micelles on the substrate depends on the molecular weight of the polymer shell [99, 100], retraction velocity and velocity gradient [101, 102], concentration of polymer in solution [103] and the solvent properties such as polarity, viscosity, surface tension and temperature [104]. Table 4.2 summarizes the properties of micellar solution such as utilized solvents and loading. After the dip-coating

Table 4.2: Characteristics of used micellar solutions.

polymer	C $[mg/mL]$	solvent	L	trivial name
PS(25000)-*b*-PVP(15000)	7	*p*-xylene	0.5	240
PS(47000)-*b*-PVP(24000)	5	toluene	0.5	451
PS(110000)-*b*-PVP(52000)	5	toluene	0.5	1056
PS(190000)-*b*-PVP(55000)	5	toluene	0.5	1824

procedure, the polymer shell can be removed by reactive plasma etching process.

*Calibration and velocity range of used dip-coating device is presented in chapter 4.3.1

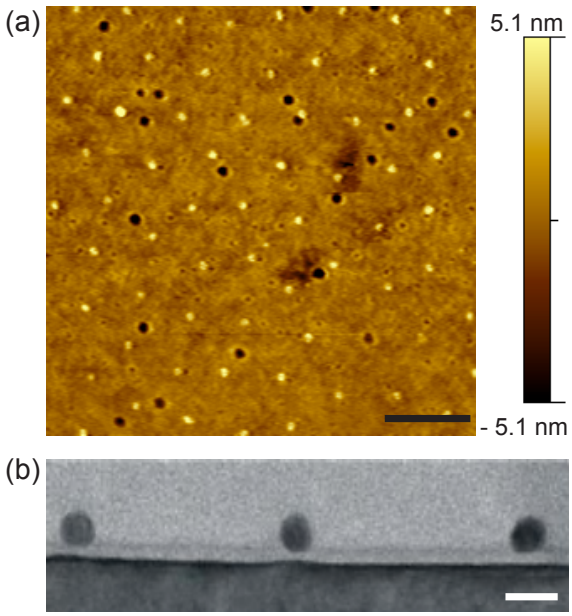

Figure 4.3: (a) Extended gold nanoarrays fabricated via PS(190000)-*b*-PVP(55000) polymer and investigated by scanning probe microscopy; scale bar 200 nm. Height signal is shown. (b) Transmission electron micrograph of single gold nanoparticles on silicon support; scale bar 10 nm. Adapted from [105].

During this process, the metal precursor salt, here $HAuCl_4$, is reduced to spherical elemental gold nanoparticles remaining on substrate surface. Figure 4.3a presents an example of extended gold nanoparticles, fabricated via BCMN on glass surface and investigated by scanning probe microscopy. Here, the quasi hexagonal arrangement of the nanopatricles (bright spots) is observable. The darker spots, according to the hight scale, represent holes in the glass surface, which is typical for commercially available glass slides.

4.2 Poly(ethylene glycol)-diacrylate hydrogels

Nanopatterning techniques like BCMN, introduced in the previous paragraph, are powerful tools in terms of arranging single, nanometer sized anchors for molecules on substrate surfaces for their further chemical modification. However, due to fabrication requirements, many of these techniques are limited to solid inorganic materials such as silicon or glass. Nowadays, the requirements for nanotechnology are not only limited to solid substrates. A wide range of applications within basic research and beyond depends on the potential to change mechanical properties of nanopatterned surfaces. Many different approaches to fabricate chemically and biologically active substrates with tunable mechanical properties are known. For example, synthetic elastic supports like polyacrylamide [80] (PA), polydimethylsiloxan [106] (PDMS), hyaluronic acid [107] (HA) are widely used. Even proteins like collagen I could be polymerized into gels [108]. In the case of synthetic supports, crosslinker concentration and concentration of functional molecules of interest in the coating solution, could control the elasticity of the resulting substrate and its chemical and biological activity.

Table 4.3: Properties of used PEG-DA polymers.

polymer	$M_W[g/mol]$	solvent
PEG-*700*-DA	700	H_2O
PEG-*10000*-DA	10000	H_2O
PEG-*20000*-DA	20000	H_2O
PEG-*35000*-DA	35000	H_2O

In this work, poly(ethylene glycol) (PEG) was chosen to serve as an elastic support because of its outstanding properties in terms of biological application. It is a water soluble, nontoxic and biologically inert polymer. Biochemical passivation is crucial if used proteins feature strong unspecific adhesion on inorganic surfaces used for BCMN. They can undercut the advantage of BCMN by adsorption between the well ordered gold nanoparticles [109, 110]. For this reason, underlying supports should feature protein-repelling properties. These properties of PEG molecules, as shown in thin film systems, originate from a number of factors including the very low interfacial free energy with water, high steric stabilization by volume restriction and excluded volume effects as well as the geometrical structure of PEG in the water lattice [111]. Unfortunately PEG macromolecules can not be polymerized into a gel. So, the attachment of two acryl groups on the opposite ends of the molecule was performed. The obtained poly(ethylene glycol)-diacrylate (PEG-DA) macromolecules still retain the protein-repellent properties of PEG, while the acryl groups allow the polymerization into a hydrogel [90, 112, 113]. PEG-DA molecules used within this work are presented in Table 6.1 Detailed synthesis of PEG-DA molecules is described in Chapter 4.3.1.

4.2.1 Transfer lithography

Graeter et al. [90] demonstrated for the first time the feasibility of the transfer of extended gold nanoparticle-arrays from a glass template to a polymer surface. Here, extended studies and further developments on nanostructured PEG-DA based hydrogel systems will be presented. PEG-DA macromers with molecular weights summarized in Table 4.3 were polymerized by UV irradiation (λ=365 nm) in the presence of (4-(2-hydroxyethoxy)phenyl-(2-propyl)ketone) as radical chain reaction initiator [114]. When exposed to UV light, the reaction initiator homolytically dissociates into two radicals (initiation). The reactive species attack the terminal double bond of PEG-DA, thereby causing the formation of new radicals. It then attacks the double bond of another PEG-DA monomer and in this way propagates the chain reaction (propagation). If the polymerization takes place on a glass substrate supporting an array of gold nanoparticles, where the gold has been functionalized with the unsaturated transfer linker N,N′-bis(acryloyl)cysteamine featuring identical acrylic group, it is possible to covalently anchor the nanoparticles to the hydrogel meshwork during

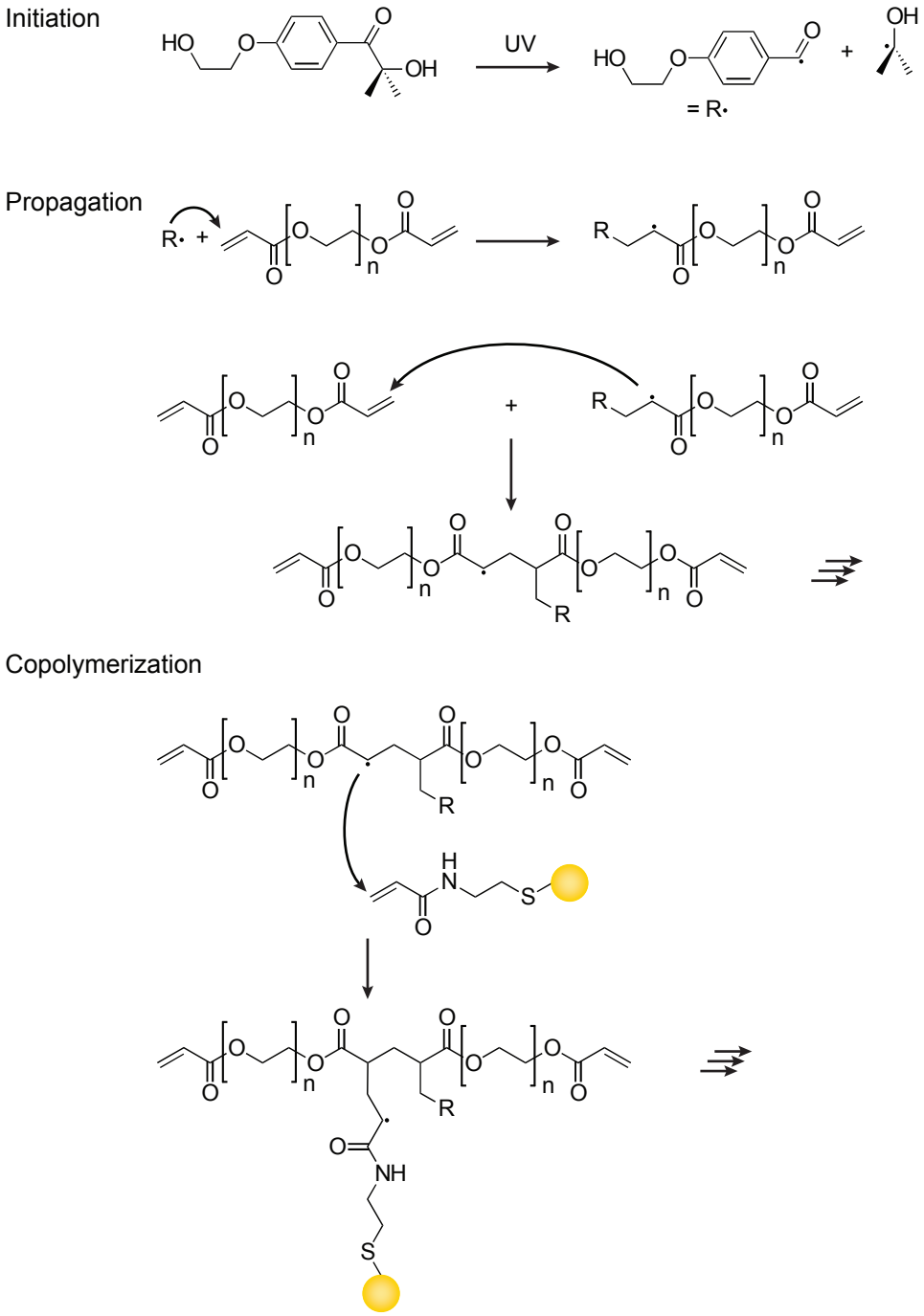

Figure 4.4: Polymerization process of PEG-DA (in aqueous solution) initiated by 4-(2-hydroxyethoxy)phenyl-(2-propyl)ketone upon UV irradiation (365 nm) and copolymerization of N,N′-bis(acryloyl)cysteamine-functionalized gold nanoparticles into the resulting PEG-DA hydrogel.

the polymerization reaction (copolymerisation). Figure 4.4 illustrates the polymerization process of PEG-DA hydrogel and covalent binding of gold nanoparticles on its surface.

Figure 4.5 depicts the whole fabrication process of nanopatterned PEG-DA hydrogels, thus transfer lithography procedure. First, extended quasi hexagonally ordered arrays of gold nanoparticles on glass supports were fabricated by BCMN. Then, the nanoparticles were functionalized by transfer linker and covered with an aqueous prepolymer solution containing the desired concentration of certain PEG-DA macromer and the photoinitiator. UV irradiation initiates the polymerization process, which results in a water-containing hydrogel covalently bound to the gold particles. Subsequently, the samples were incubated in water for at least 48 h. Lateral forces

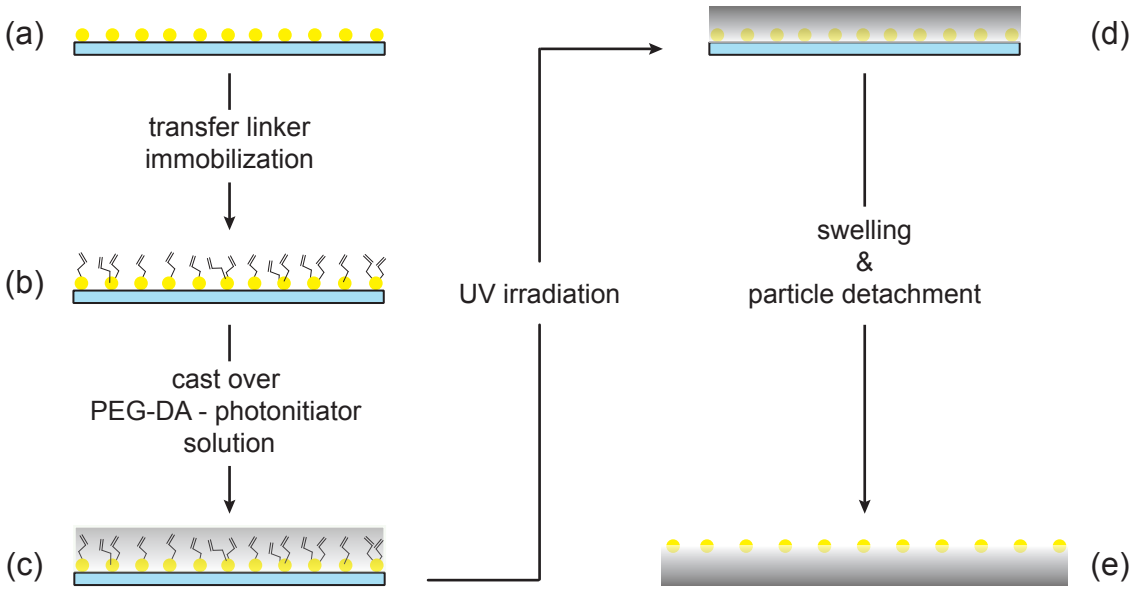

Figure 4.5: Gold nanoparticles on solid support (a) are covalently coupled to transfer linker (b). After casting over PEG-DA-photoinitiator solution (c) and irradiation by UV light the linker is copolymerized into the PEG-meshwork (d). Swelling caused by incubation in water induces particle detachment resulting in a gold nanoparticle decorated hydrogel substrate (e).

induced by the swelling process are responsible for the detachment of gold nanoparticles from the glass surface with transfer efficiency of almost 100 percent as shown in Figure 5.5. The swelling of the PEG-DA hydrogels is a crucial process in terms of particle transfer from glass support onto the hydrogel surface. Due to this process, interparticle distances on the hydrogel substrates will be increased isotropically by a so called swelling ratio factor SR.

The swelling process prevents the fabrication of interparticle distances lower than 40 nm - 45 nm because of the minimal interparticle spacing, achieved on glass surfaces, of approximately 30 nm (Fig: 5.2a). Therefore, the size of the gold nanopar-

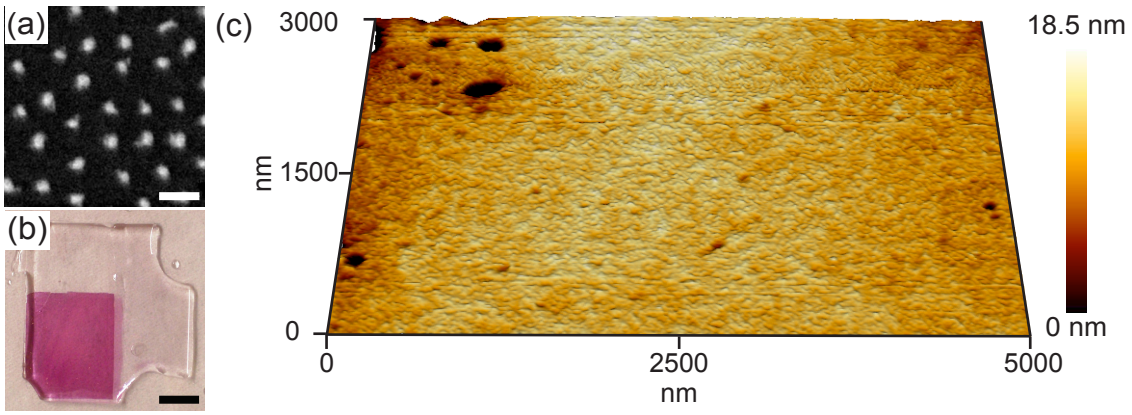

Figure 4.6: Gold nanoparticles on the surface of PEG-DA hydrogel enlarged by electroless deposition (a). Particle size ≈ 25 nm, scale bar 200 nm. (b) PEG-*700*-DA hydrogel sample decorated by extended gold nanoparticle array enlarged by electroless deposition. The Nanopatterned area is indicated by their plasmon absorbance, scale bar 5 mm. (c) Scanning probe micrograph of PEG-*10000*-DA hydrogel. The sample features very low topography profile $R_a = 3.3$ nm; $R_q = 5.4$ nm.

ticles was enlarged to 25 nm as explained in the next chapter.

4.2.2 Tuning particle size

Increasing the particle size to 25 nm sterically allow the binding of two proteins per one nanoparticle. If the original interparticle spacing was in the range of 45- 50 nm (after the hydrogel swelling), enlargement of the gold nanaoparticles will bisect the interparticle spacing. This will result in the so called effective interparticle spacing ($\Delta L^* = \Delta L/2$). For this reason, the size of gold nanoparticles covalently bound to the PEG-DA hydrogel matrix were increased by electroless deposition of gold by using a seeded-growth procedure in the presence of gold ions and hydroxylamine hydrochloride as a reducing agent [115, 116]. The gold nanopatterned hydrogels were therefore immersed in an aqueous solution of $HAuCl_4$ and reducing agent [117]. Already after the reaction time of a few seconds, the patterned parts of the sample turned red due to a higher plasmon absorbance as a consequence of the increasing particle size [118]. Cryo SEM[†] measurements were performed to investigate the particle growth in detail as shown in Figure 4.6. After 3 min reaction time, the particles were enlarged to a size of around 25 nm. Particle enlargement is proceeding as long as Au^{3+} ions are present in solution. Incubating the substrate in deionized water can stop the reaction. Thus, the particle size can be precisely adjusted depending on the reaction time.

[†]Cryo scanning electron microscopy (Cryo SEM) is detailed presented in Chapter A.1

4.3 Experimental

4.3.1 Substrate preparation

Substrate cleaning

Glass slides and the glass container for preparing the micellar solution were cleaned in freshly prepared piranha solution. This solution consisted of a 3:1 mixture of concentrated sulfuric acid (H_2SO_4) (JT Baker, Deventer, Holland) and hydrogen peroxide (H_2O_2, 30%) (Carlo Erba, Rodano, Italy). Finally the substrates or containers were extensively rinsed with deionized water (R = 18 Ω, Millipore filtered) and blown dry with pure nitrogen.

Preparation of micellar solution

Selected diblock copolymers (Polymer Source Inc., Dorval, Canada) were dissolved in toluene or *p*-xylene (p.a., Merck, Darmstadt, Germany) in the desired concentrations presented in Table 4.2 and stirred for 24 hours. All micellar solutions were loaded by $HAuCl_4$ (Sigma Aldrich) at a loading of $L = 0.5$ and stirred again until the precursor salt was dissolved, but at least for 24 hours. The amount of $HAuCl_4$ is given by

$$m_{HAuCl_4} = m_{PS-b-PVP} \frac{M_{HAuCl_4} \cdot n_{PVP}}{M_{PS-b-PVP}} L \tag{4.2}$$

The molecular weight of $HAuCl_4$ depends on the content of included crystal water, here M_{Au}=339.79 g/mol (Sigma Aldrich). The molecular weight of the polymer ($M_{PS-b-PVP}$) and the number of PVP-units (n_{PVP}) are summarized in Table 4.1.

Dip-coating and plasma treatment

The dip-coating was performed with the indicated constant velocity using a custom made dip-coating device. The calibration and velocity range of used device is presented in Table 4.4. After the solvent evaporation, substrates were treated with reactive oxygen (0.4 mbar O_2; 150 W 15 min) and hydrogen (0.4 mbar H_2; 150 W 45 min) microwave-induced plasma (TePla 100-E, Germany).

Table 4.4: Calibration of dip-coating device & retraction velocities.

voltage U [V]	3	6	8	10	12	16	18	20
retraction velocity v [mm/min]	4.5	11.1	15.5	19.9	24.3	33.1	37.5	41.9

Synthesis of PEG-DA

Poly(ethylene glycol) diacrylates (PEG-DAs) (Fluka, Basel, Switzerland) were synthesized according to a slightly modified literature procedure [119]. In a typical synthesis PEG-*10000* (50 g, 5 mmol) was dried by codistillation with toluene (3×250 mL) (p.a., Merck, Darmstadt, Germany). The residue was redissolved in dichloromethane (125 mL) (p.a., Merck, Darmstadt, Germany) and toluene (75 mL) under nitrogen atmosphere. From this point, all the following operations were performed protected from light. Triethylamine (1.4 mL, 10 mmol) (Sigma Aldrich) and acryloyl chloride (1.25 mL, 15 mmol) (Sigma Aldrich) were sequentially added and stirring was continued overnight at room temperature. The reaction mixture was then filtered over a plug of alumina (neutral). K_2CO_3 (12.5 g) (Sigma Aldrich) was added to the filtrate and the mixture was stirred for 1.5 h. The solid was removed by filtration and the filtrate was concentrated under vacuum to remove as much dichloromethane from the mixture as possible. The product was then precipitated by addition of diethylether (350-400 mL) under vigorous stirring. After 2 h the solid was recovered by filtration, washed with diethylether (2×100 mL) and dried under vacuum. 40-45 g of pure product were obtained (80-90% yield). PEG-*20000*-DA and PEG-*35000*-DA were prepared accordingly.

PEG-DA polymerization and transfer lithography

PEG-*700*-DA was mixed with water to a final concentration of 1100 mg mL^{-1}. PEG-*10000*-DA, PEG-*20000*-DA or PEG-*35000*-DA was dissolved in water at designated concentration between 200 mg mL^{-1} and 1400 mg mL^{-1}. An aqueous, cold saturated solution of 4-(2-hydroxyethoxy)phenyl-(2-propyl)ketone (Sigma Aldrich) acts as initiator and was added to the polymer solution before the polymerization process. The amount of added initiator solution was 0.22 $\mu l/mg_{PEG-DA}$ in the case of PEG-*700*-DA and 0.15 $\mu l/mg_{PEG-DA}$ for PEG-*10000*-DA, PEG-*20000*-DA and PEG-*20000*-DA, respectively. Prior to the transfer and polymerization process, gold nanostructures were incubated in an ethanolic solution (p.a. Sigma Aldrich) of N,N′-bis(acryloyl)cysteamine (2 mM) (Sigma Aldrich) for 1 h. To remove non-covalently bound N,N′-bis(acryloyl)cysteamine substrates were rinsed with ethanol three times for 10 minutes.

Electroless deposition

Electroless deposition was performed by immersing the samples into an aqueous mixture of $NH_2OH \cdot HCl$ (0.2 mM) (Sigma Aldrich) and $HAuCl_4$ (0.1% w/w) (Sigma Aldrich). After 3 minutes reaction time the samples were extensively rinsed and stored in ultrapure water to prevent further particle enlargement by excess seeding solution.

Biofunctionalization

Prior biofunctionalization, all substrates were sterilized by UV irradiation. To provide cell adhesion on PEG-DA hydrogel substrates c(RGDfK)-thiol was immobilized on gold nanopatterns. Therefore, substrates were immersed in an aqueous solution of c(RGDfK)-thiol (25 µM) for 45 min. To remove the non-covalently bound c(RGDfK)-thiol, the substrates were rinsed with deionized water (R = 18 Ω, Millipore filtered) every 10 min for a period of 40 minutes. Before seeding cells onto the substrates, PEG-DA hydrogels were transferred into sterile phosphate buffered saline (PBS) solution and subsequently incubated in warm cell culture medium for at least 10 min.

4.3.2 Scanning electron microscopy and cryo SEM

A Zeiss Ultra 55 field emission electron microscope (FE-SEM) equipped with in-lens, secondary electron (SE) and energy and angle selective backscattered electron (ESB) detectors was used for image acquisition (ZeissSMT, Oberkochen, Germany). Acceleration voltages of about 5 keV and working distances between 3 and 10 mm were used. Signals were detected by the in-lens detector.

Cryo SEM was performed under low temperature conditions ($T_{op} \approx -130°C$). Low acceleration voltages of 1-2.5 kV were applied because of the low conductivity of the investigated samples. A BAL-TECH VLC 100 (BAL-TEC AG, Balzers, Lichtenstein) shuttle and loading system and a BAL-TECH MED 020 (BAL-TEC AG, Balzers, Lichtenstein) preparation device were used to cool down and transfer the PEG-DA hydrogels into the SEM chamber.

4.3.3 Scanning probe microscopy

Single cell force spectroscopy and image aquisition

SCFS and imaging was performed with a "Nano Wizard I" SPM (JPK Instruments AG, Berlin, Germany). The instrument is mounted on an optical microscope (Zeiss Axiovert 200) and is suitable for simultaneous phase contrast or fluorescence measurements. Additionally, an incubator box driven by an EMBL GPI68 IV controller was installed to provide cell-culture conditions during the measurements. Silicon nitride tipless cantilevers (NSC 12 tipless no AL; µmasch, Estonia) were used for SCFS and (Veeco NanoProbe NP-S; Veeco, Camarillo, USA) for image acquisition. Spring constants were determined by the thermal noise calibration method and ranged between 2.6 N/m and 8.3 N/m, respectively.

Indentation measurements

Indentation measurements were performed with a "Nano Wizard I" SPM (JPK Instruments AG, Berlin, Germany). Silicon nitride cantilevers with a cone-shaped tip

(µmasch NSC 35 ALBS) were used for indentation measurements. Spring constancies were determined by the thermal noise calibration method and ranged between 2.3 N/m and 12.5 N/m [120]. Since the opening angle of the tip is a crucial parameter to measure Young modulus by the Hertz method it was determined for each used cantilever by SEM.

Cantilever functionalization

Tipless, silicon nitride cantilevers (NSC 12 tipless no AL; µmasch, Estonia) were simultaneously cleaned and activated for 5 min with reactive oxygen plasma (0.4 mbar O_2; 150 W 15 min). Subsequently, they were silanized by (3-aminopropyl)-trimethoxysilane (Sigma Aldrich) in the gas phase and dried 30 min at 60° C. After the incubation in an 1% aqueous solution of glutaraldehyde (Sigma Aldrich) they were extensively washed in PBS. Eventually, the cantilevers were rinsed in water before immersed into a PBS solution of 10 µg/ml fibronectin (Sigma Aldrich) for at least 30 minutes.

4.3.4 Cell culture

Cell type

All experiments were performed on Ret embryonic fibroblasts (REF) cells kindly provided by B. Geiger[‡] REF cells were stably transfected by A. Cavalcanti-Adam[§] with paxillin fused to yellow fluorescent protein (YFP) [121].

Cell seeding

Cells in culture are trypsinized and seeded on the biofunctionalized substrates surfaces in DMEM (Gibco) containing 10% fetal bovine serum (FBS), 2 % L-glutamine and 1 % penicillin-streptomycine. The experiments were performed after desired cell-substrate interaction time under cell-culture conditions (5 % CO_2, 37° C)

Phase contrast and fluorescence imaging

Phase contrast and fluorescence micrographs as well as live cell imaging were performed using a DeltaVision microscope (Applied Precision, Issaqua, WA, USA) equipped with phase contrast objectives (20x and 40x Olympus, Tokyo, Japan). Additionally, a home made incubator box was installed to provide appropriate conditions during the measurements.

[‡]Weizmann Institute of Science, Rehovot, Israel.
[§]University of Hiedelberg, Heidelberg, Germany.

Part III

Characterization of elastic nanopatterned substrates

Chapter

5

Combining BCMN and PEG-DA hydrogels

Basic principles of nanotechnology in terms of decorating organic an inorganic surfaces with quasi hexagonal patterns of gold nanoparticles were presented in the previous part of this thesis. BCMN is a well established and well applied approach, as is the fabrication of PEG-DA hydrogels. The most challenging issue during the presented research was the combination of both aforementioned techniques. Recently, a prove of principle was presented, where extended gold nanoparticles were successfully transferred to the PEG-DA based substrate surfaces [90]. Nevertheless, during the initial experiments it became apparent, that a further development of this substrate system is necessary. Methods and results of characterization, applied and gained during this enhancement of the substrate system will be presented in this chapter. They were achieved on statistically relevant amount of analyzed samples and were repeatedly reproduced to gain representative values of each substrate type for the whole substrate system.

To quantify the spacing and order of extended gold nanoarrays, characteristic patterns produced by used micellar solutions were consistently analyzed to gain approximate values. Prior, the transfer lithography, representative samples from each used batch were characterized via SEM and image processing evaluation routines.

The mechanical properties of PEG-DA hydrogels were quantified within 3 to 5 different areas per sample (10 measurements per area) and on at least two different substrates. This characterization routine was repeated 2-3 times for each substrate type. At least 120 values were accounted for the mean calculation of E_Y per substrate type.

In the case of swelling ratio determination, at least 3 samples were measured at 4 different positions. This was repeated 2-4 times for all PEG-DA polymers and their concentrations. At least 24 values were accounted for the mean calculation of SR, corresponding to each used substrate type.

The verification of the transfer efficiency of the nanoparticles to the PEG-DA hydrogel surface was first performed on all substrate types as prove of principles. Considering the complexity of time consuming cell experiments, each substrate was investigated by cryo SEM. Detailed characterization techniques and gained results will be presented in this paragraph.

5.1 Characterization of nanopatterned surfaces

The gold nanoparticles and pattern fabricated by BCMN are in the nanometer range. Therefore, advanced characterization methods, like scanning electron microscopy (SEM) and scanning probe microscopy (SPM) are needed to verify the quality of desired surfaces*. To do that, quality as a term should be defined. Here, two parameter are of major interest. First, it is crucial that the interparticle distance ΔL is quintessentially constant, i.e. the quasi hexagonal arrangement of the pattern should be of high quality. Therefore, so called order parameter Φ of the nanoparticles relative to each other will be defined and determined. And second, the size of the single nanoparticle is of great interest since single protein-ligand binding is important. This is affected by the amount of the precursor salt within single micelle, thus the loading L [98]. The interparticle spacing is controlled and the order parameter affected by micelle size, thus by the length of the polymer and the assembly of the micelles into a monolayer during the dip-coating [122]. This process is governed by the thickness of the solvent layer at the air-solvent-substrate interface and thus the retraction velocity. At higher velocities the solvent layer, which adheres at the glass surface and gets retracted out of the solution becomes thicker. Consequently, more solution containing more micelles is retracted. This results in a more densely packed micellar layer on the substrate surface after the complemented solvent evaporation and thus smaller interparticle distances. Several examples of scanning electron micrographs of extended gold nanoarrays with typical interparticle distances for the polymers 240, 451, 1056 and 1824 are presented in Figure 5.1. The quasi hexagonal arrangement of gold nanoparticles and constant interparticle spacing of the pattern is clearly visually observable.

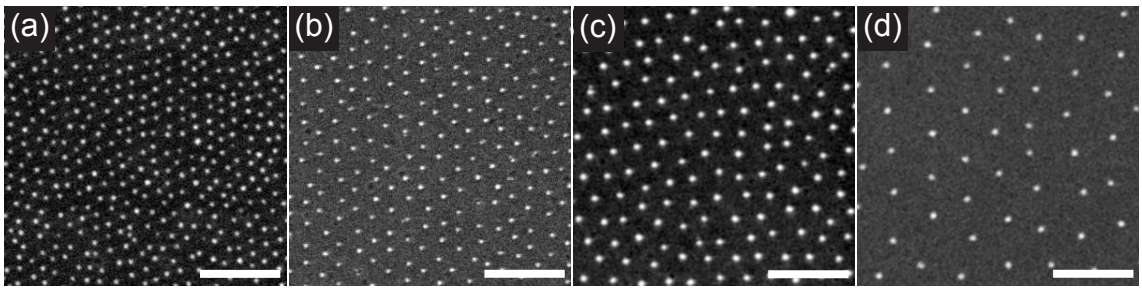

Figure 5.1: Scanning electron micrographs of extended gold nanoparticle arrays on glass support. Images correspond to the PS-*b*-PVP polymers presented in Tab. 4.2. Interparticle distances: (a) 34 nm; (b) 48 nm; (c) 68 nm; (d) 92 nm. Scale bars 200 nm.

To quantify the quasi hexagonal order of the resulting pattern the global bond-orientation order parameter $0 \leq \Phi \leq 1$ is postulated. It was originally introduced as a model of two dimensional crystallites melting in colloidal suspensions [123] and

*SEM and SPM techniques are presented in Chapters A.1 and A.2

is defined as

$$\Phi_6 = \left| \frac{1}{N} \sum_{j=1}^{N} \Psi_6(r_j) \right| \tag{5.1}$$

where N is the number of analyzed particles and Ψ_6 the local order parameter for a particle j located at $r(x, y)$. The local sixfold bond-orientation parameter of a particle j and its six nearest neighbors k is given by

$$\Psi_6(r_j) = \frac{1}{n_j} \sum_{k=1}^{n_j} \exp\left[6i\theta_{jk}\right] \tag{5.2}$$

where i is the imaginary unit and θ_{jk} denotes the angle of the bond between particle j and one of its nearest neighbors k relative to a fixed arbitrary reference axis.

The interparticle spacing ΔL within a nanoparticle array represents the average distance r_{jk} between particle j to its nearest neighbors k for every single particle and is averaged over N particles

$$\Delta L = \frac{1}{6N} \sum_{j=1}^{N} \sum_{k=1}^{6} r_{jk}. \tag{5.3}$$

The standard deviation is given by

$$\sigma_{\Delta L} = \sqrt{\frac{1}{6N} \left[\sum_{j=1}^{N} \sum_{k=1}^{6} r_{jk}^2 - 6Nd^2 \right]} \tag{5.4}$$

In practice, scanning electron micrographs of representative nanostructured substrates as shown in Figure 5.1 were analyzed using ImageJ[†], an image processing software, via a plugin kindly provided by Dr. Philippe Girard[‡]. After the binarization of a 8 bit grayscale image the plugin localizes the position of the nanoparticles and measures the angles θ_{jk} for each particle followed by calculation of the real and imaginary contribution of Φ_6 according to equation 5.5.

$$\Phi_6 = \frac{1}{6N} \sqrt{\left(\sum_{j=1}^{N} \sum_{k=1}^{6} \cos(6\theta_{jk}) \right)^2 + \left(\sum_{j=1}^{N} \sum_{k=1}^{6} \sin(6\theta_{jk}) \right)^2} \tag{5.5}$$

Interparticle spacing and order parameter of surfaces used within this thesis are plotted against the dip-coating velocity and presented in Figure 5.2. Only samples having $\Phi_6 \geq 0.5$ were taken for further use as denoted by the red dashed line.

[†]Rasband, W.S., ImageJ, U. S. National Institutes of Health, Bethesda, Maryland, USA, http://rsb.info.nih.gov/ij/, 1997-2005.

[‡]European molecular biology laboratory (EMBL). Heidelberg, Germany

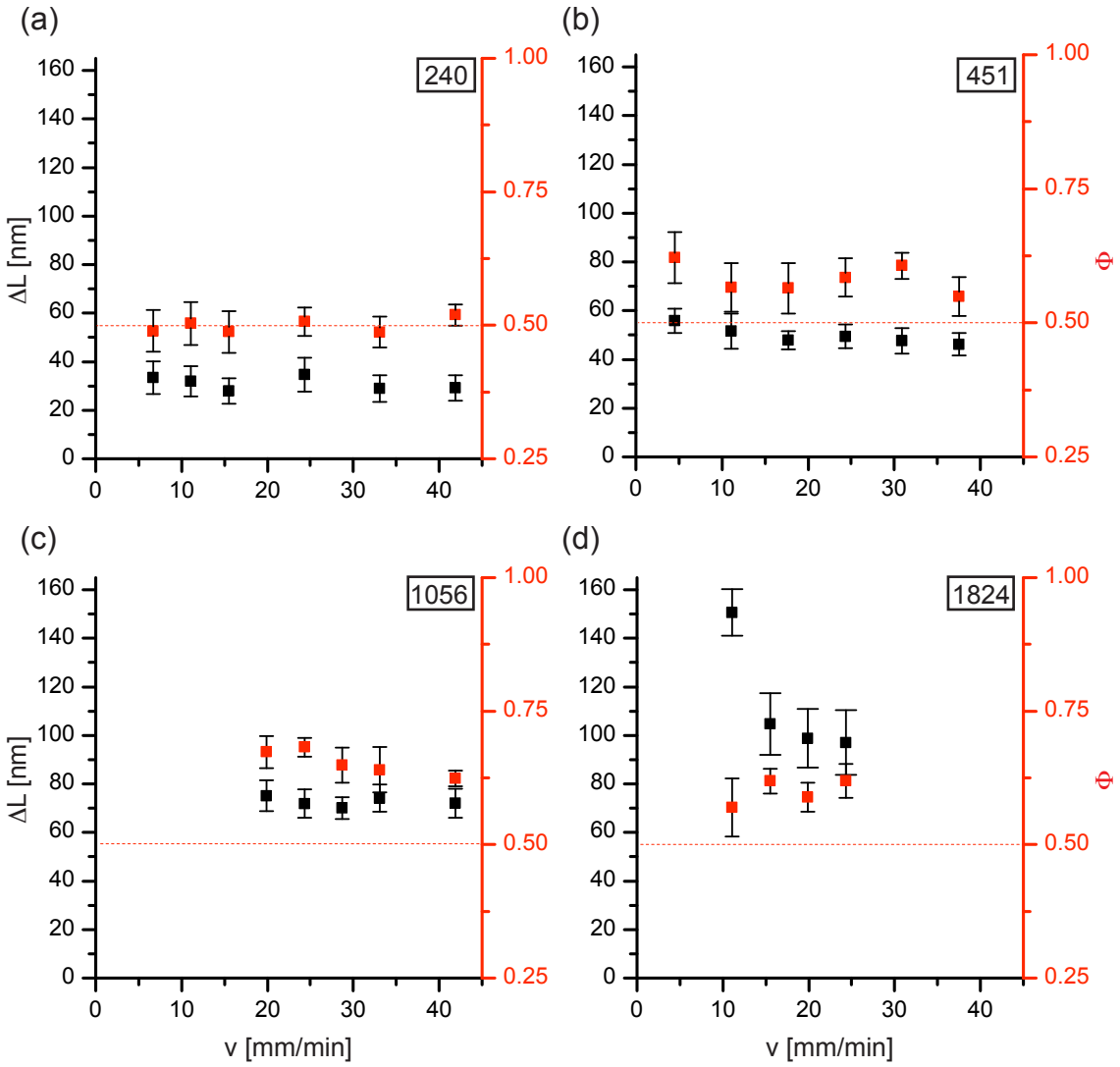

Figure 5.2: Interparticle spacing ΔL and order parameter Φ of extended gold nanopatterns created with frequently used PS-*b*-PVP polymers. (a) PS(25000)-*b*-PVP(15000), (b) PS(47000)-*b*-PVP(24000), (c) PS(110000)-*b*-PVP(52000). See also Table 4.2. The error bars represent standard deviation according to equation (5.4) and denote the standard deviation of singleparticle-particle spacing.

It turns out that four different micellar solutions (as presented in Tab 4.2) are sufficient to assure high quality decoration of substrates by gold nanoparticles with interparticle spacings from approximately 30 nm to at least 120 nm. In the case of used micellar solutions, the dip-coating velocity only partially influenced the interparticle spacing. Fabrication of strong velocity-sensitive nanopatterns is a matter of solution parameters [39] and was not in focus of this thesis. Here, different velocities were used to optimize order parameter Φ of the resulting nanopatterned surfaces.

As shown in Figures 4.3, SPM is also suitable for visualization of quasi hexagonally ordered nanoparticles on the glass surface. Since SPM is impractical for "every-day" control of the substrate quality due to the extreme sensitivity to environmental noise and the low scan size of about 100 μm^2, SEM was used to determine order parameter of nanoparticle distribution.

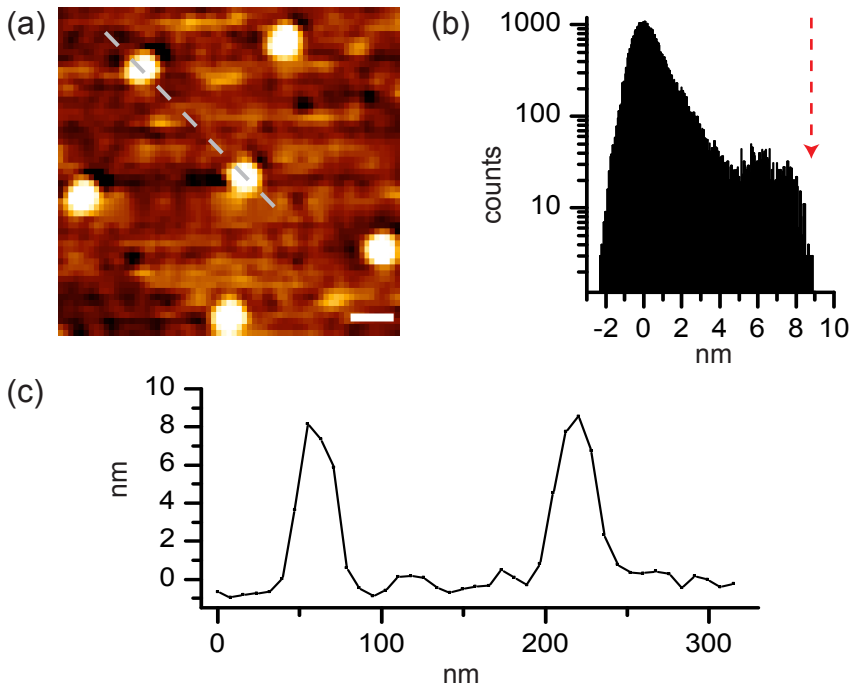

Figure 5.3: Size of typical single gold nanoparticles is characterized by scanning probe micrograph. (a) Color coded topographical information (height signal) of quasi hexagonally ordered gold nanoparticles, scale bar 30 nm. Dashed line represent hight profile showed in (c). (b) Distribution of height values acquired by the scanning procedure. Red arrow denotes maximum hight value, thus particle diameter, here about 9 nm.

Unfortunately, on the given length scale SEM is heavily charged by measurement artifacts in terms of particle size determination [124]. The size of the particles is crucial if single protein-ligand interaction is desired and should not exceed protein dimensions. As described above, integrins, which establish the cell-substrate connection are in focus of this research, thus only particle sizes of approximately 8 - 10 nm are acceptable. To determine the size of the particles, high resolution scan-

ning probe microscopy was performed on representative substrates. There are two methods of particle size determination: height profiles of selected particle arrays and height distribution histograms based on height signal information gained over the whole sample. The second is much more significant, because of better statistics of SPM images that usually consist of about 10^5 height values or pixels. Figure 5.3 visualizes high resolution close-up of SPM image of selected nanoparticles. Both, the presented height profile and height distribution histogram suggest a particle size of approximately 9 nm.

Whereas the interpretation of the height profile is straightforward, the information gained by height distribution diagram needs to be explained. During the image acquisition by conventional SPM, cantilever tip-sample interactions (e.g. attractive and repulsive forces) are processed by feedback routines to remain constant by changing the cantilever tip-substrate distance during the scan[§]. This can be achieved by continuous variation of piezo-driven cantilever holder. The readout of precise information of these variations results in a high resolution height profile of the investigated sample. Now, quantitative information about height could be gained via histogram. Here, all height values and their frequencies are outlined against nominative measured heights. As expected, the mean of the histogram is approximately allocated at zero, due to the low global coverage of the sample by nanoparticles and is representing the surface of the underlying support. Consequently, the entirety of the highest histogram values appoints highest structures on the sample surface and thus the gold nanoparticle size. This is presented in Figure 5.3b denoted by the red arrow, and determine the particle size of investigated sample of approximately 9 nm.

To prove single particle decoration by protein of interest and thus single protein-ligand bond, in case of cell-substrate interaction, gold nanoparticle decorated surfaces were functionalized by histidine-tagged green fluorescent protein (GFP) and investigated by SPM. These experiments were published in Reference [125]. In summary, glass substrates were first decorated with arrays of 142 nm spaced gold nanoparticles featuring a diameter of 6.5 nm. To avoid unspecific GFP binding to the glass surface gold nanoparticles were embedded into a 5 nm thick matrix of poly(ethylene glycol). Then functionalization with a 3 nm thick monolayer of $HS-(CH_2)_{11}-EG_3-NTA-Ni(II)$ was performed to enable side-directed immobilization of GFP molecule. Scanning probe micrographs with and without immobilized GFP molecules are presented in Figure 5.4. Here, the maxima of 4.5 nm in the height profile as well as the drop in the height histogram plot at 4.5 nm are in good accordance with the expected value. When GFP is coupled to the particles, the maxima of the height profile increases to 9 nm and the drop in the height histogram shifts to 10.5 nm. This value of around 5 nm very well suits the reported size of the protein [126] whereas the unaltered width of the presented height profiles strongly suggests single protein immobilization.

[§]SPM technique is detailed presented in Chapter A.2.1

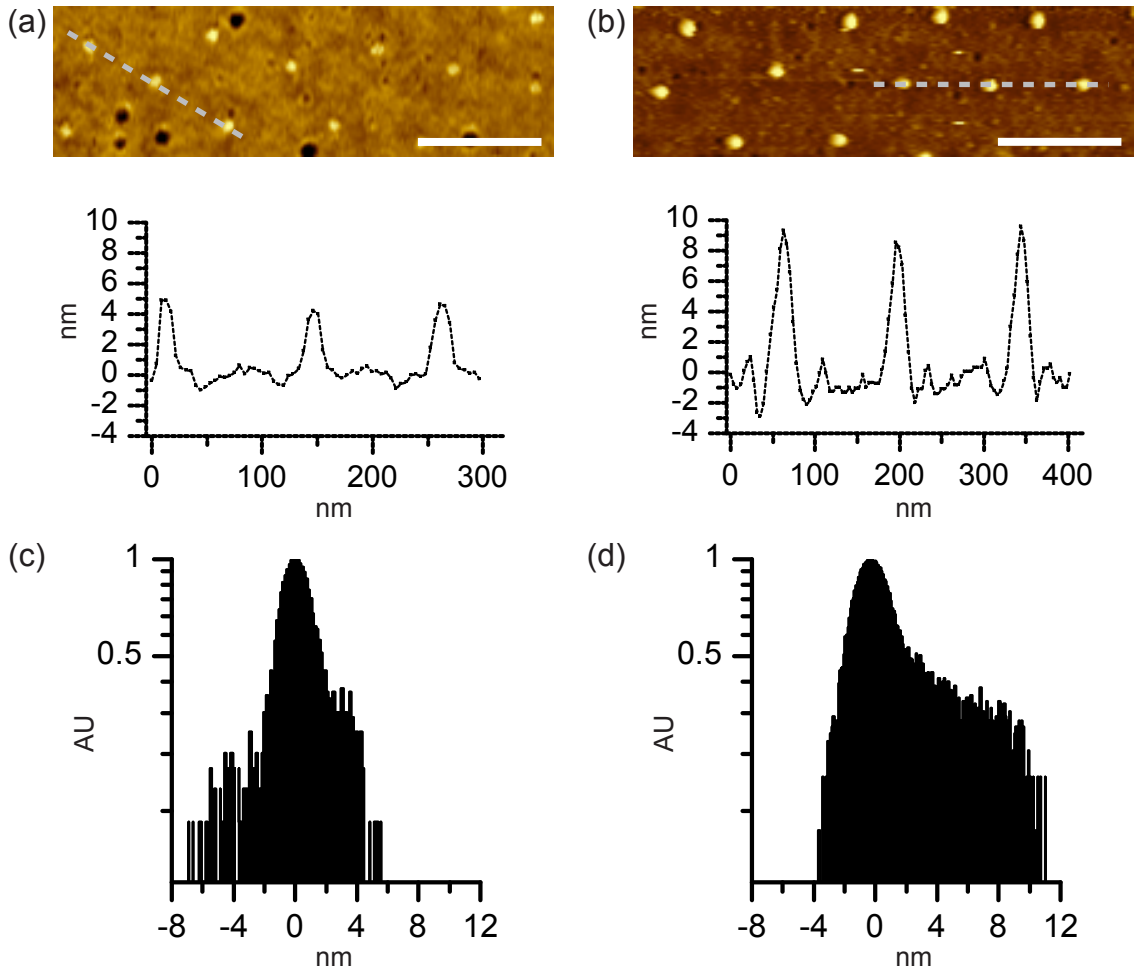

Figure 5.4: Green fluorescent protein was used to prove single molecule immobilization on gold nanoparticle surface. Blank (a) and functionalized (b) gold nanoparticles with corresponding height profiles denoted by dashed lines, scale bars 200 nm. Distribution of height values measured on unfunctionalyzed (c) and functionalised (d) surfaces. The difference of its maximum values of about 4-5 nm corresponds to the reported size of the protein [126]. Adapted from [125].

5.2 Characterization of PEG-DA hydrogels

The substrates based on PEG-DA hydrogels feature outstanding properties at one hand but at the other hand these properties like high degree of hydration and nanoparticle decoration complicate the characterization procedure. While SEM and SPM were able to quantify and prove the quality of gold nanopatterns they are not applicable in the same way on PEG-DA hydrogels. In case of SEM all samples need to be conductive and suitable for vacuum conditions. The requirement of conductance could be circumvented by applying low acceleration voltages, but due to the very high water content of hydrogels, application of required low environmental pressures within the SEM chamber (p $\approx 10^{-5}$ mbar) is not possible. Consequently,

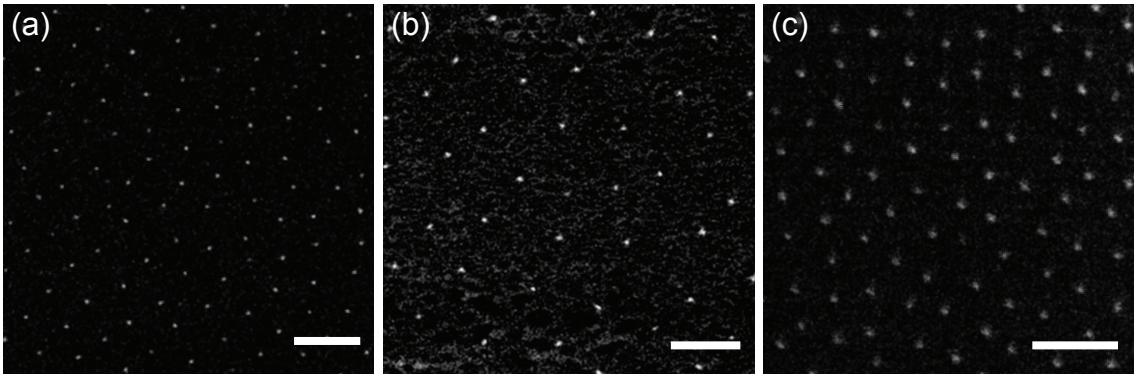

Figure 5.5: Cryo scanning electron micrographs of PEG-DA hydrogels. (a) Extended gold nanoparticle pattern fabricated via PS(25000)-*b*-PVP(15000) polymer on the PEG-*10000*-DA hydrogel surface; scale bar 100 nm. (b) PEG-*20000*-DA hydrogel decorated by gold nanoarray fabricated via PS(190000)-*b*-PVP(55000) polymer; scale bar 200 nm. (c) PS(110000)-*b*-PVP(52000) based gold nanoparticles after transfer on the PEG-*35000*-DA hydrogel surface; scale bar 200 nm.

cryo SEM was used to characterize the transfer efficiency of gold nanoparticles to the hydrogel surface. The great advantage of this method is the very low temperature (≈ -160° C) of the vacuum chamber of the SE microscope and the sample of interest. Due to this low temperature conditions the vapor pressure of ice is low enough ($p_{ice} < 1.4 \cdot 10^{-5}$mbar) to apply needed vacuum pressures without significant outgasing of H_2O molecules [127]. Detailed description of cryo SEM and sample preparation is given in Chapter A.1.

All hydrogel substrates prepared within this work were investigated and characterized by cryo SEM. Moreover, each substrate used for cell experiments described in Part IV was partially investigated to ensure the complete transfer of gold nanoparticles to the PEG-DA hydrogel surface. As presented in Figure 5.5, it could be verified, that independent of the PS-*b*-PVP polymer based micellar solution the nanostructures were successfully transferred one-to-one, with nanoscale precision, from the glass to the respective PEG-DA hydrogel substrate. At the same time the

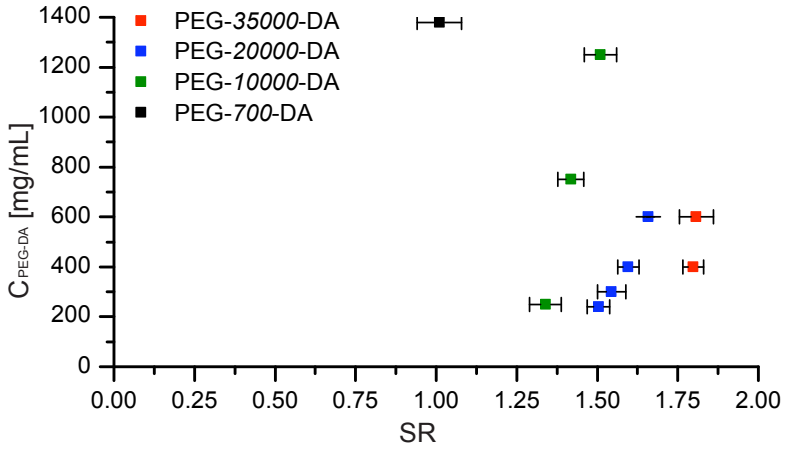

Figure 5.6: Swelling ratio SR of PEG-DA hydrogels. The error in swelling ratio refer to the standard error in the mean.

quality of the arrangement of the nanoparticles (order parameter Φ) was unaffected by the transfer procedure. Only the interparticle distances were changed due to the isotropic swelling of the gels.

Simple and fast calculation of the interparticle distances after the swelling is important, therefore corresponding swelling ratio SR of all used hydrogels at different PEG-DA polymer concentrations in pre-polymerized, aqueous solution were acquired macroscopically[¶] via slide gauge. Then the resulting interparticle distances ΔL_{new} are a product of the swelling ratio SR and the interparticle distance on the glass support ΔL.

$$\Delta L_{new} = SR \cdot \Delta L \tag{5.6}$$

As presented in Figure 5.6, the swelling ratio decreases with decreasing concentration of the polymer C_{PEG-DA} in pre-polymerized solution. It usually ranges from $SR_{PEG-700-DA} \approx 1$ to $SR_{PEG-35000-DA} \approx 1.8$.

SPM was used to quantify the surface topography and the mechanical properties of PEG-DA hydrogels. Scanning probe micrographs were performed and roughness parameter R_a and RMS[‖] roughness R_q acquired. The typical roughness of PEG-DA based substrates is approximately $R_a = 3$ nm and $R_q = 5$ nm respectively, which is comparable with the roughness of glass supports used for BCMN ($R_a \approx 0.5$ nm and $R_q \approx 1.5$ nm). An example was presented in Figure 4.6.

In order to quantify mechanical properties, indentation measurements were performed and Young's Moduli E_Y of all substrate types calculated according to modified Hertz model [128–130]. The Hertz model was chosen because no appreciable

[¶]All PEG-DA gels were prepared by casting into a casting mold with given dimensions. The swelling ratio was calculated by comparing these dimensions with the resulting gel dimensions after swelling.

[‖]RMS = root mean square

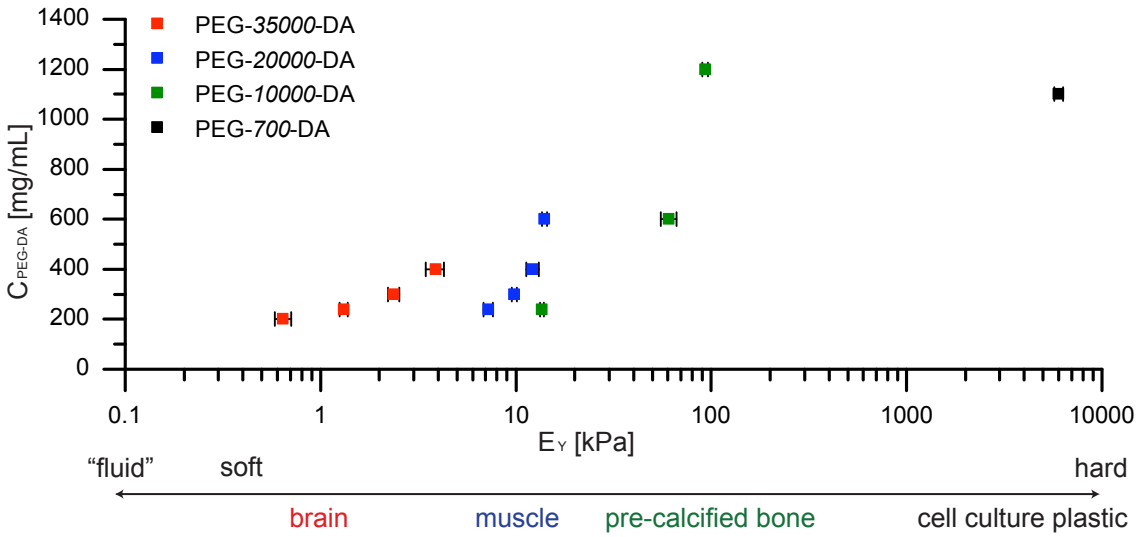

Figure 5.7: Young Moduli E_Y of PEG-DA hydrogels used in his study were determined by indentation method and fitting of the Herz model [128]. Elasticity of hydrogel substrates tunable over four orders of magnitude allows to mimic mechanical properties of nearly all significant tissues [82]. Error bars in substrate elasticity refer to the standard error in the mean.

adhesive and repulsive interactions between the indenter and the substrate were expected and measured due to the aforementioned repellent properties of PEG. The data were acquired via an SPM approach called atomic force spectroscopy (AFS). The AFS and the Hertz model are presented in Chapter A.2.1.

The E_Y of PEG-*700*-DA, PEG-*10000*-DA, PEG-*20000*-DA and PEG-*35000*-DA hydrogels are presented in Figure 5.7. Indentation measurements revealed that the mechanical properties of the hydrogel substrate system can be effectively controlled by choosing a PEG-DA macromer with appropriate molecular weight (700 g/mol$\leq$ M_W $\leq$35000 g/mol) and varying its concentration C_{PEG-DA} in the aqueous polymer solution before the polymerization process. The elasticity of PEG-DA hydrogels can be gradually adjusted within four orders of magnitude including that of all different tissues present in the human body from very soft nervous to rigid bone tissue [82].

Within the performed cell experiments, which will be presented in the next part of this thesis, fibroblasts were selected as a cellular model system. To provide bioactivity, gold nanoparticles were functionalized with the cyclic RGDfK pentapeptide mostly recognized by the integrin type $\alpha_V\beta_3$ [131] an integrin highly expressed in fibroblasts.

In the past, approaches were presented featuring good E_Y adjustment, but poor control properties in terms of ligand density (on nm range) and no control at all in terms of ligand-to-ligand spacing respectively. Moreover, their elasticity and ligand density directly or indirectly depends from each other [89]. Furthermore, substrates coated with large ECM proteins (e.g collagen or fibronectin) could be remodeled by

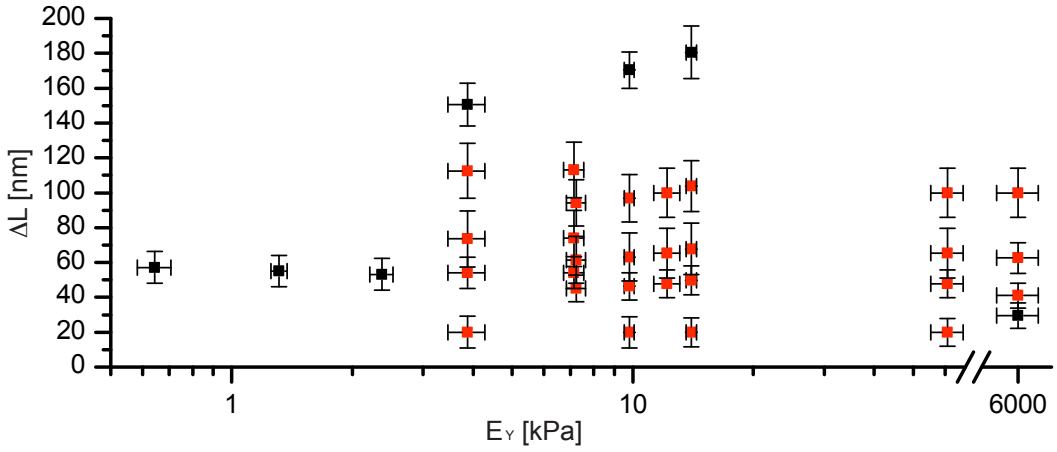

Figure 5.8: Summary over nanopatterned PEG-DA hydrogel substrates with tunable gold nanoparticle spacing ΔL and elasticity E_Y. Red datapoints denote substrates used in this work. Error in ΔL is calculated acorrding to equation (5.4). Error in E_Y refer to standard error in the mean.

cells [132, 133]. Only due to the transfer lithography approach, the elasticity of the substrates and the interparticle spacing of the decorating gold nanoparticles are fully independent from each other [134]. As denoted by the black datapoints in Figure 5.8, a large variety of substrates with different biochemical (25 nm$< \Delta L <$160 nm) and biomechanical (0.6 kPa$< E_Y <$6 MPa) properties were fabricated and characterized. The red datapoints are representing 32 substrates featuring continuously adjustable properties in terms to mimic cellular environments with unprecedented proximity.

In the next part of this thesis the first cell biology aimed approach of PEG-DA based, nanopatterned substrate system will be presented. Within this system two crucial parameters such as substrate compliance and ligand spacing could be regarded as a two-dimensional space of environmental parameters. Both parameters could be changed to mimic a large variety of different tissues types in terms to investigate cellular behavior like adhesion, migration, proliferation, differentiation and viability.

Part IV

Results

Chapter

6

Cell spreading on elastic ECM analogs

In the previous part of this thesis, PEG-DA based nanopatterned hydrogel were introduced as a versatile tool to control micro- and nano-environmental properties of cellular surroundings. As demonstrated in Figure 6.1 they are fully suitable for cell adhesion experiments. It was shown that their biochemical and biophysical characteristics are tunable within values of interest, which are set by physiological properties of connective tissues. In this part, the substrate system should be regarded as a two-dimensional space of environmental parameters that can be changed to study sensing capabilities of cells.

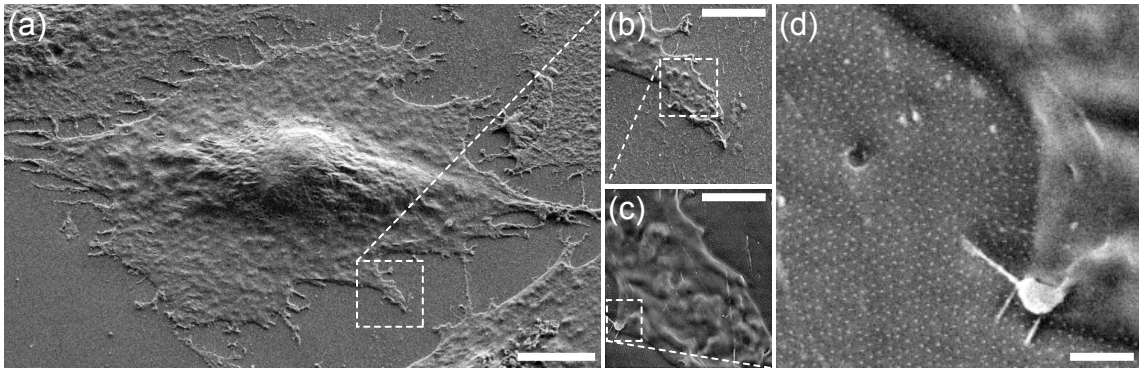

Figure 6.1: Cryo SE micrographs of PEG-DA hydrogel designed for cell experiments (E_Y=6 MPa; ΔL=60 nm). (a) Spread rat embryonic fibroblast on elastic nanopatterned substrate 24 hours after seeding; scale bar 15 µm. The cellular adhesion on the biofunctionalized gold nanoparticles is clearly observable. Scale bars 4 µm (b), 1,5 µm (c), 500 nm (d).

At the cellular level, biomechanical and biochemical signals originating from the tissues can have dramatic effects on the global regulation of cell functions such as apoptosis, migration, growth, and differentiation. Therefore, cells constantly monitor the properties of their environment. For instance, during cell spreading, cells are continuously faced with new ligands in the tissue or on substrate surface. As they stabilize, they become less dynamic, but the turnover of focal contacts and

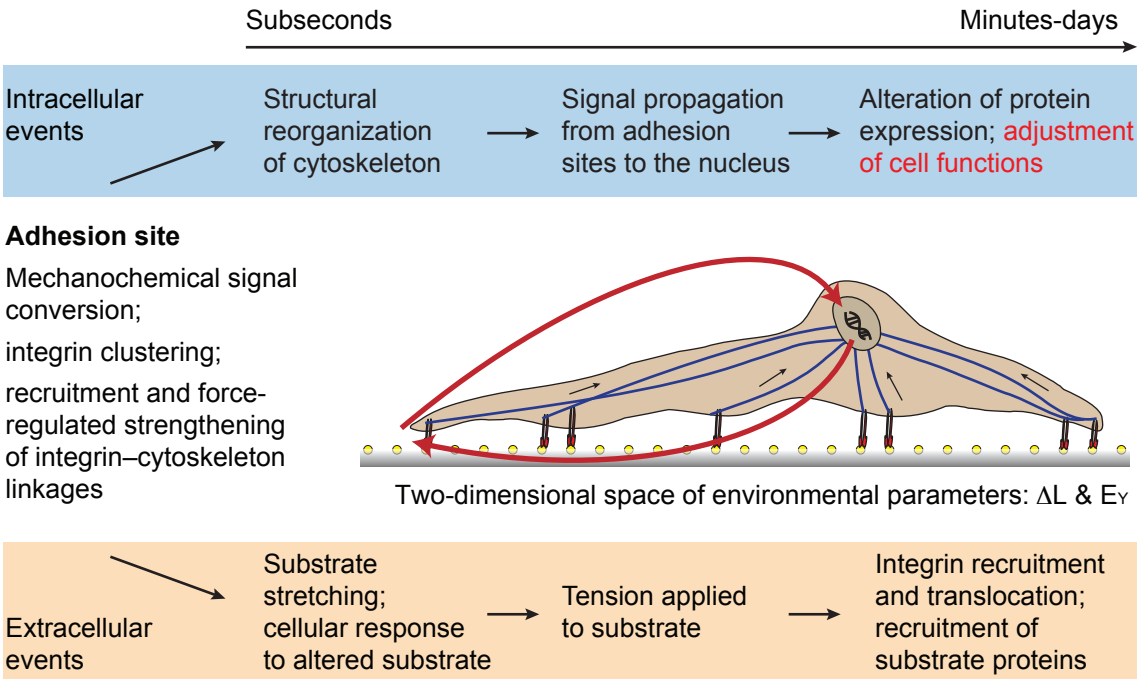

Figure 6.2: This overview shows key steps in environmental sensing over time that involve periodic testing of the substrate, substrate modification and changes in cellular protein content. Initially, cells sense the mechanical features of their environment, which cause rapid motility and signalling responses. Intracellular signals alter gene expression and finally cell shape. Adapted from [57].

the cytoskeletal proteins permanently occurs on timescale of minutes [42, 135, 136].

In case of synthetic substrates, the surface chemistry influences the composition and conformation of surface-adsorbed proteins. It can change affinity and avidity of adhesion molecules and induce signaling processes [35, 137]. Comparably, the physical properties of the ECM determine the initial rigidity sensing. As the cell generates forces on the proteins that link the ECM to the cytoskeleton, the effect on this mechanosensitive sites will cause global cellular responses due to the mechanical properties of the matrix [77, 138]. Moreover, there are possible mechanisms to transform physical stimulus via transcription factors* directly into biochemical signals that regulate gene expression [140].

As summarized in Figure 6.2 cellular responses can take place on various timescales. Initial interactions occur within subseconds and seconds. Early cell responses take seconds to minutes and involve cytoskeletal rearrangement, reinforcement of linkage and changes in cell motility and spreading [57]. For example, integrated sensing pathways finally link ECM stiffness through integrin clustering to phenotype reg-

*Transcription factors are proteins that bind to specific DNA sequences and control the transcription from DNA to RNA [139].

Table 6.1: System of PEG-DA based, hydrogel substrates representing two-dimensioned space of environmental parameters such as substrate elasticity E_Y and spacing ΔL of integrin binding sites, utilized for cell adhesion experiments. Error corresponds to the error bars in the Figure 5.8

ΔL [nm]	102±8	103±8	94±7	97±7	100±7	104±8	100±8	100±8
E_Y [kPa]	3.8±0.4	6.8±0.4	7.2±0.4	9.8±0.3	12.2±0.9	14.0±0.4	60.9±5.6	6k±300
ΔL [nm]	74±8	74±8	64±6	65±6	65±7	68±7	65±7	62±8
E_Y [kPa]	3.8±0.4	6.8±0.4	7.2±0.4	9.8±0.3	12.2±0.9	14.0±0.4	60.9±5.6	6k±300
ΔL [nm]	48±9	48±9	45±7	46±8	48±8	50±8	48±8	41±7
E_Y [kPa]	3.8±0.4	6.8±0.4	7.2±0.4	9.8±0.3	12.2±0.9	14.0±0.4	60.9±5.6	6k±300
ΔL^* [nm]	27±5	27±5	22±4	23±4	24±4	25±4	24±4	20±4
E_Y [kPa]	3.8±0.4	6.8±0.4	7.2±0.4	9.8±0.3	12.2±0.9	14.0±0.4	60.9±5.6	6k±300

ulation. The response of cells to their surroundings is cell specific and seems to correlate with the biophysical properties of the tissue where the cells originate from. For example, smooth muscle cells originating from arteries ($E_Y \approx$ 5-8 kPa) show a spreading behavior threshold at $E_Y \approx$ 8-10 kPa [81]. Therefore, the idea of the experiments presented below was to alter the environmental stimuli in terms of compliance and surface chemistry of the substrates offered to the cells. These alterations should include several orders of magnitude and thereby reveal functional limits of the investigated cell type. Table 6.1 summarizes the properties of 32 different substrate used within this thesis. The substrates were sterilized and subsequently functionalized with thiol-terminated cyclic-RGDfK peptide.

Two kinds of experiments will be introduced and described. First, spreading of rat embryonic fibroblasts, stably transfected with paxillin labeled by yellow fluorescent protein (REF YFP pax), was analyzed by phase contrast microscopy after desired cell-substrate interaction time. The resulting spreading area or projected cell area A was determined by a custom made Matlab[†] script as a function of substrate stiffness E_Y and binding site spacing ΔL. Second, cell-substrate detachment forces F_{ADH} were measured by single cell force spectroscopy (SCFS). Combined with fluorescence microscopy, the adhesion force density ρ_{ADH} was determined and will be also presented as a function of the aforementioned two-dimensional space of environmental parameters. Figure 6.3 shows an example of spread fibroblasts on elastic nanopatterned substrates. Due to the dip-coating fabrication procedure (for details see Chapter 4) all substrates utilized generally featured two different areas. A nanopatterned area, which was immersed in the micellar solution and non-nanopatterned area. Consequently, all nanopatterned PEG-DA hydrogels, have both areas, whereas the latter can serve as a control for biofunctionalization and cell

[†]The MatlabWorks Inc.

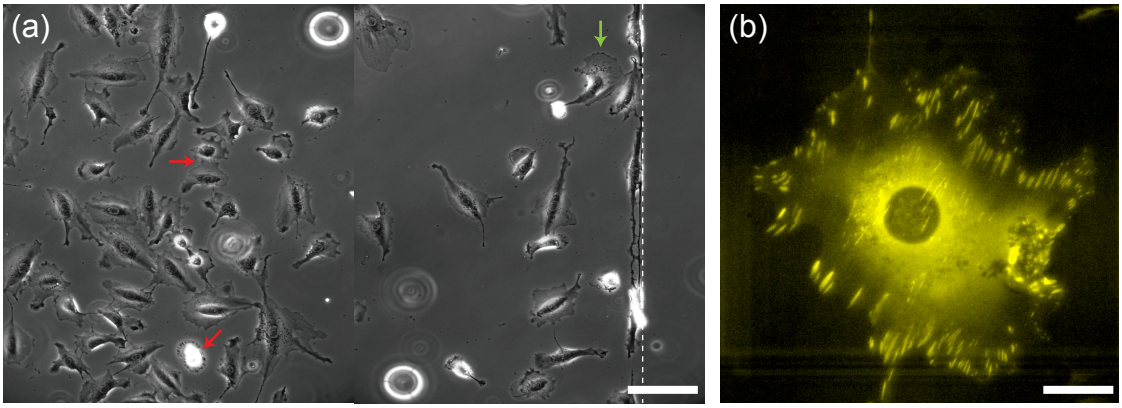

Figure 6.3: (a) Phase contrast micrographs of adherent rat embryonic fibroblasts on PEG-*10000*-DA based hydrogel (E_Y=63 kPa; ΔL=45 nm). The border between nanopatterned and non-nanopatterned area is indicated by the dashed line. No adhesion could be observed on the non-nanopatterned side due to the protein repellent properties of PEG. Cellular adhesion, proliferation (red arrows) and migration (green arrow) are observable. Scale bar 100 µm. (b) Fluorescence micrograph of same cell type, but stably transfected with paxilin fused to yellow fluorescent protein on PEG-*20000*-DA substrate (E_Y=14 kPa; ΔL=45 nm). Cell-substrate interaction sites, the focal adhesions, are well established and distributed all over the cellular periphery. Scale bar 25 µm .

adhesion. In Figure 6.3a the boundary between these areas is marked by a dashed line.

During SCFS only selected substrates were utilized, due to this very challenging and time consuming approach. Cell-substrate detachment forces F_{ADH} and adhesion force density ρ_{ADH} were quantified by varying the substrate compliance at constant nanoparticle spacing (ΔL = 45 nm). SCFS experiments where spacing of the gold nanoparticles on glass substrates was changed, were performed together with Christine Selhuber[‡] [141].

6.1 General spreading behavior

In recent years, cellular ability to spread on flat two-dimensional surfaces was exhaustively investigated. Different mathematical models were proposed to describe spreading behavior of cells [142, 143]. In case of fibroblasts a power-law area growth with distinct exponents in three sequential steps according to equation (6.1) was found [144].

$$A(t) \propto t^{\alpha_i}, i = 1, 2, 3 \tag{6.1}$$

[‡]The PhD thesis of Christine Selhuber can be found at http://www.ub.uni-heidelberg.de/archiv/7021

These steps are called phases because of the sharp transitions in spreading dynamics between them. According to the so-called hierarchical phase model, classes of functional protein modules dominate the behavior of spreading cells during a certain phase [144]. This molecules are adaptor and motor proteins and proteins involved in general signaling pathways. From the biophysical point of view, progression in phase transition can be expected as trajectories in multidimensional space of environmental parameters.

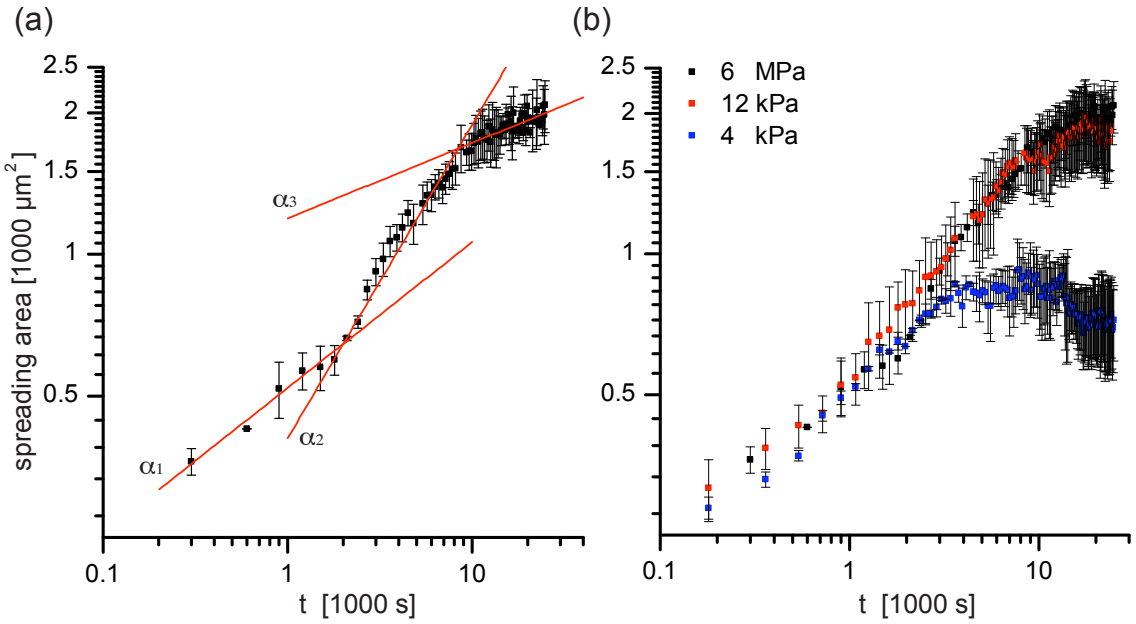

Figure 6.4: Development of the cell spreading area vs. adhesion time acquired via phase contrast microscopy. (a) Rat embryonic fibroblasts (n = 9) on rigid hydrogel substrate (E_Y=6 MPa) are showing typical spreading phases [144]. Each of these phases was fitted according to equation (6.1). (b) Development of the cell spreading area vs. adhesion time on substrates featuring different mechanical properties: E_Y=6 MPa, n = 9; E_Y=12 kPa, n = 6; E_Y=4 kPa, n= 10. The error in cell spreading area refer to the standard error of mean.

Initially, there is a phase where cells test the suitability of the substrate and the growth is minimal. Afterwards, they rapidly switch to a fast continuous spreading phase. After the development of a significant contact area, the cells sense the rigidity of the substrate via fast contraction and application of forces on the underlying substrate. These so-called basal ($\alpha_1 = 0.4 \pm 0.2$), continuous ($\alpha_2 = 1.6 \pm 0.9$) and contractile ($\alpha_3 = 0.3 \pm 0.2$) spreading represent distinct phases where significant differences in protein activities, thus overall morphological changes of the cell occur [145].

6.2 Cell spreading on compliant substrates

To validate the developed substrate system, the dynamic of cellular growth on elastic nanopatterned substrates were investigated. To this end, live cell imaging was performed. Cells were plated on substrates with elasticity of 6 MPa, 12 kPa, and 4 kPa, respectively, while the spacing of integrin binding sites remained constant at 45 nm. Phase contrast micrographs were acquired every 3 minutes. As shown in Figure 6.4 three different phases could be observed according to the model and characterized by three power-law exponents: $\alpha_1 = 0.31 \pm 0.1$, $\alpha_2 = 0.76 \pm 0.2$ and $\alpha_1 = 0.16 \pm 0.1$, respectively. As expected, each of the spreading phases qualitatively followed the model proposed above. Remarkably, the duration of the spreading phases was significantly higher than measured by Doebereiner et al. on homogeneous fibronectin surfaces. There, the phase transitions occurs within several tens of minutes [145]. This disagreement can be explained by a reduced density of integrin binding sites on nanopatterned substrates, similar to reduced fibronectin concentration on glass supports, which were shown to dramatically delay spreading time [88].

The comparison of spreading area development on all three substrate types revealed how substrate elasticity can influence cells growth. As presented in Figure 6.4, there was no significant difference in spreading area on substrates featuring E_Y=6 MPa and E_Y=12 kPa, respectively. On the other hand, on the substrate with E_Y=4 kPa cell growth stopped after approximately 50 to 60 min. Here, the cell spreading area remained constant ($\alpha_3 = 0.04 \pm 0.1$) or even decreased ($\alpha_3 = -0.17 \pm 0.3$). This suggests, that the tactile set-point of fibroblast mechanosensing lies, in agreement with the literature, most likely in between 4 kPa and 12 kPa [82]. Comparison of the cell growth on hard and soft substrates, presented in Figure 6.4b suggests the existence of an early mechanosensing event where cytoskeleton-based cell contractions are not required. Despite the relatively small number of probed cells (n=10) this should be further investigated.

It is remarkable how precise the cellular mechanosensing machinery works. A huge change in substrate elasticity, nearly three orders of magnitude (6 MPa to 12 kPa), did not influence spreading dynamics at all. Consequently, did not affected the spreading phase transitions. At the same time, a small change of several kPa (12 kPa to 4 kPa) had a strong effect on cell growth. Another very interesting conclusion can be drawn. In agreement with the model presented above, mechanosensing definitely occurs at the beginning of the third phase where fast cellular contractions were observed. If cells were plated on soft (4 kPa) substrates, the "result" of this sensing performed by the cell was negative, such that spreading was stopped and full transition into the third phase of continuous growth was impeded.

6.3 Cellular spreading behavior influenced by two-dimensional space of environmental parameters

The experiments presented above as well as recent studies [83, 146] have investigated cellular responses depending on variable substrate or tissue elasticity, thus biophysical properties. Of course, mechanosensing is a very important part of the cellular sensing machinery. At the same time, this machinery responds not only to soft or rigid substrates, but to essential multifarious environment. Other studies include variation of biochemical signals originating from the artificial substrate in form of concentration of coating protein or peptide [40, 88]. Until now, it was hardly possible to independently vary both of these parameters.

Here, the first approach aimed at cell biology of two-dimensioned space of environmental parameters was applied to gain more detailed insight into cellular spreading behavior. After changing biochemical and biophysical properties of artificial ECM analog, cell growth was investigated on the timescale of hours and days. To this end, REF YFP pax cells were plated on all available substrate types presented in Table 6.1. Subsequently, phase contrast micrographs were taken after 6 h, 12 h and 24 h of adhesion, respectively. Examples of phase contrast and fluorescence micrographs acquired 24 h after seeding to determine cell spreading area, are shown in Figure 6.5. They also show typical cellular morphology and focal adhesion formation on corresponding substrates.

Here, a strong dependence in cell spreading area and morphology on substrate stiffness and binding sites spacing is observable. On rigid substrates (Fig. 6.5f) a large, spread REF YFP pax cell is shown. Well-established focal adhesions are homogeneously distributed over the whole cell periphery. The focal adhesions appear as sharp, elongated spots of approximately the same size.

When cells attach to soft substrates, which can easily be deformed, the effective elasticity of the cell-substrate system $\frac{1}{K}$ (equation (2.19)), measured by the mechanosensitive apparatus of the cell, is dominated by the lower elastic modulus of the substrate. Therefore, the tension acting on focal adhesions may be smaller than the required amount of force to maintain them according to Chapter 2.2.1. The effect of low substrate elasticity can be observed in Figure 6.5a and b. On this substrate cells developed diffuse, small and inhomogeneously sized and distributed focal adhesions and feature low spreading area. The substrate compliance seems to be a dominant parameter, since binding site spacing variations did not affect cellular behavior on soft substrates.

On stiff substrates, spacing strongly dominated cellular morphology and affected focal adhesion formation (Fig. 6.5d). Here, cells were elongated and did not feature well-formed focal adhesions. Instead, focal complexes[§] small ($< 1\mu m$), cellular

[§]The difference between focal adhesion and focal complexes is described in Chapter 1.3.3

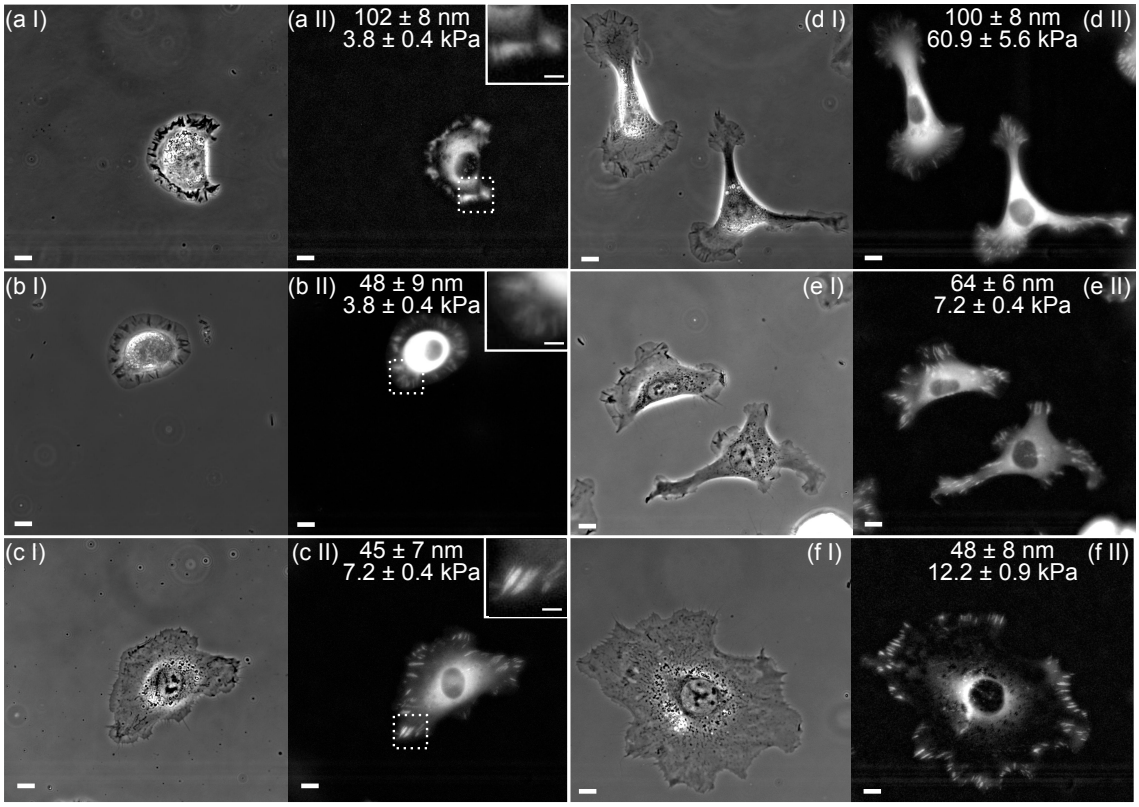

Figure 6.5: Phase contrast (I) and fluorescence micrographs (II) of rat embryonic fibroblasts stably tranfected with paxillin fused to yellow fluorescent protein (REF YFP pax) on elastic nanopatterned substrates under cell culture conditions. 24 hours after seeding. Scale bars (a)-(f) 10 µm. Insets: focal contact and focal adhesion formation on different substrates, scale bars 2 µm.

adhesion sites were visible. On the one hand, strong fluorescent cell body suggests, that paxillin, an important focal adhesion protein (see Chapter 1.3.3 for details), is still well expressed by the cell. However, it could not be recruited into the focal adhesion because of the high binding site spacing.

Interesting cellular behavior can be observed on intermediate soft substrates ($E_Y \approx$ 7 kPa) with binding site spacing of approximately 45 nm and 70 nm, respectively (Fig. 6.5c and e). The cells spread, but featured lower spreading area as in Figure 6.5f. Moreover, focal adhesion formation was strongly affected on the latter. In general, cells on substrates featuring interjacent values of E_Y and ΔL ($\Delta L \approx 70$ nm; $E_Y \approx 7$ kPa) receive environmental signals, which correspond to critical values as will be presented later. This may explain their size, shape and focal adhesion formation as shown in Figure 6.5e. All these phenotypical properties are in a kind of intermediate state. The cells are spread, but do not reach the spreading area maximum as on stiffer substrates. They develop focal adhesions, but not in the same quality and quantity as on substrates with lower binding site spacings. This

observations could be confirmed on the basis of evaluation results presented in the next paragraph.

6.3.1 Quantification of cell spreading area

To gain significant results over 11,000 cells were analyzed. Spreading area values A were pseudo color-coded and plotted against substrate elasticity E_Y and spacing of integrin binding sites ΔL as presented in Figure 6.6. These results represent the trajectories of cellular behavior in the two-dimensional space spaned by environmental parameters.

As can be observed in Figures 6.6a-c, cellular spreading area grew over the whole investigated time period. It reached its maximum on the substrate with small binding site spacing and high Young modulus (20 nm$<\Delta L<$65 nm and 10 kPa$<E_Y<$60 kPa). The area increased from approximately A_{6h}=1700 μm^2 measured 6 hours after seeding to A_{24h}=3000 μm^2 after 24 hours of adhesion. As expected, this constant growth was limited by the substrate properties mentioned above.

Already after 6 hours, very prominent threshold in cell spreading area could be observed on all substrates featuring low elastic moduli ($E_Y<$8 kPa). This is not very surprising since the mechanosensing processes are known to be initiated within the first hours of cell-substrate contact. Furthermore, evaluation results agree with sudden stop of cell area growth on soft substrates (E_Y=4 kPa) found by live cell imaging experiments as presented in Figure 6.4 and discussed in the previous chapter.

When binding site spacing was varied, a second transition in cell spreading area could be observed. It is not very dominant within first 12 hours after seeding, but becomes clearly visible after 24 hours of adhesion. It is allocated at ΔL=65 - 70 nm and is in good agreement with values, found in earlier investigations. The critical spacing of approximately 70 nm originates from integrin clustering processes during focal adhesion formation and was proposed to be caused by talin driven integrin stabilization [40, 102, 147]. The slow development of this transition, can also be affected by, compared to the elasticity, relatively large deviation in binding site spacing (see Fig. 5.2 and Tab. 6.1). However, cell feature similar, low spreading on substrate with 100 nm binding site spacing.

Obviously, there is a time-dependent development in cellular spreading within the investigated period of 24 h. Growth dynamics of the spreading area in the first 8 hours were already discussed in the last chapter. It revealed three sequential phases, each characterized by power law exponents. Considering the long time period of 24 h, no further phase transitions could be assumed. To investigate the dynamics of long-term spreading, cell growth rate ΔA was therefore calculated by simple subtraction of spreading area recorded on corresponding substrates between the 6th and 24th hour of adhesion. Normalized, color-coded results ([% h^{-1}]) are presented in Figure 6.6d.

As expected, both aforementioned thresholds in the cell spreading area are still

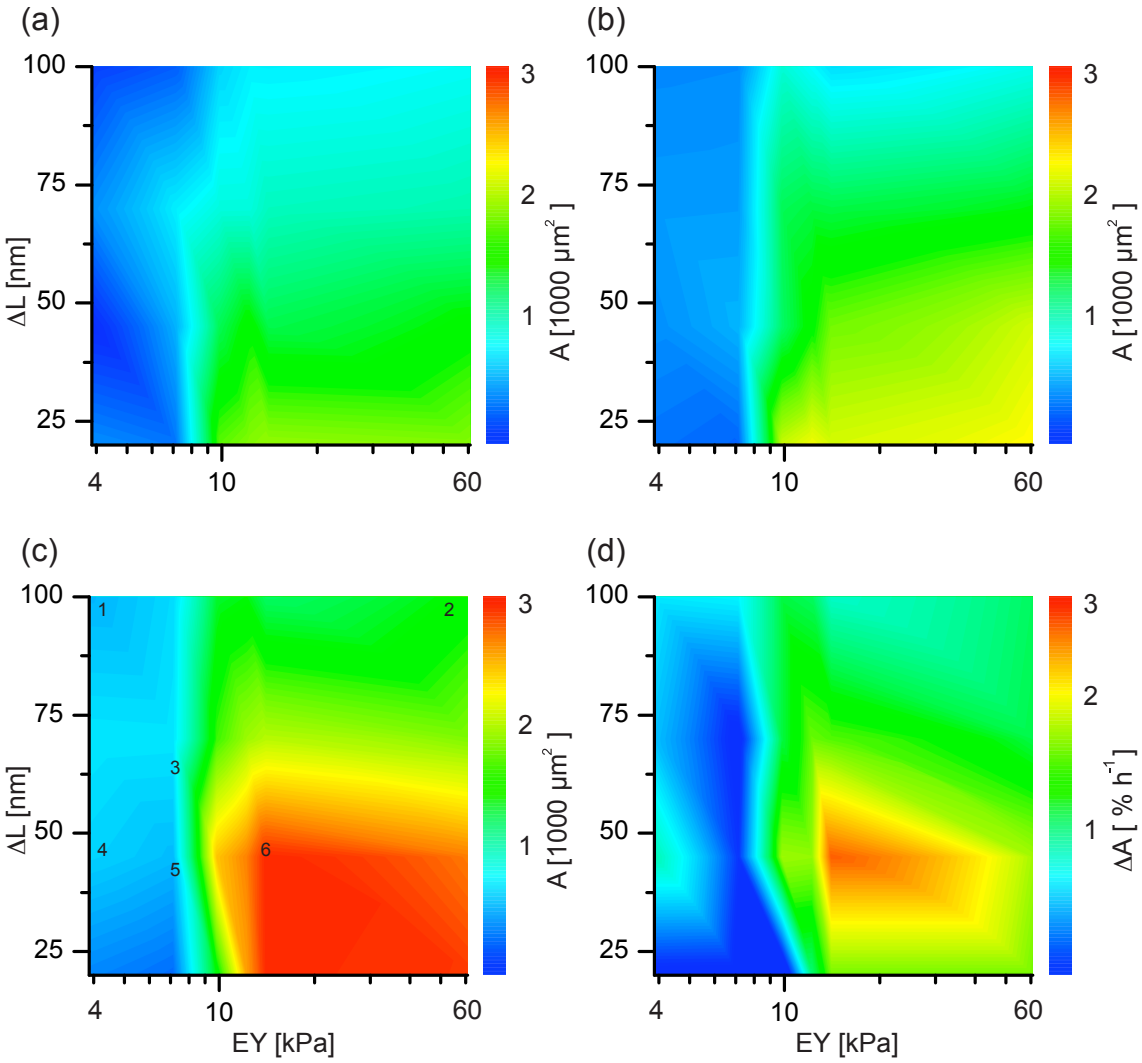

Figure 6.6: Cell spreading area of REF YFP pax cells 6 h (a), 12 h (b) and 24 h (c) after seeding, respectively. The spreading area is pseudo-color coded and plotted against substrate elasticity E_Y and spacing of integrin binding sites ΔL. More than 11,000 cell were analyzed in total. Numbers in (c) correspond to phase contrast and fluorescence micrographs presented in Figure 6.5. The data is smoothed for better visualization. Example of discrete, measured datapoints are presented in Figure 6.7.

dominant. Moreover, cells on soft substrates ($E_Y < 8$ kPa) showed less or no growth during the whole time period. In contrast, cell growth rate on substrates with high binding site spacings ΔL >70 nm was definitely affected, but to a significantly lower extent.

Surprisingly, the growth rate was not constant on substrates with small binding site spacing and high Young modulus. Here, an area of maximal growth rate is present. Substrate elasticities between approximately 12 and 50 kPa and binding site spacings of about 35 to 65 nm seems to enhance the cell growth. This is a remarkable result: cells does not grow equally on all substrates, even if the environmental parameters are not critical. They develop maximum growth rates on substrates featuring properties corresponding to the physiological. For example, during biomechanical investigations of the dorsal side of the arm elasticities between 20 and 100 kPa were found [10]. Concerning the cell growth decrease on substrates with binding site spacing less than 35 nm, one can speculate that integrins do not bind to each ligand presented on the substrate surface until a half of the critical value (70 nm) is reached. Thus, spacings lower than 35 nm lead to steric inhibition of adhesion molecules, which can result in lower spreading area.

6.3.2 Tactile set-points of mechanosensing

The substrate-stiffness dependent trend in cell growth seems to be very dominant. At each measured time-point cells are more spread on stiffer substrates. But on some substrates meanderings from this trend exist. Namely small shifts of threshold in spreading area on substrates featuring binding sites spacing of around 70 nm after 6 hours of adhesion and at 30 nm, 24 hours after seeding. Therefore, a theoretical model was applied to gain more insight into the cellular spreading processes.

A hyperbolic relation,

$$A(E_Y) = (A_{max} - A_{min})\frac{E_Y^m}{E_{1/2}^m + E_Y^m} + A_{min} \tag{6.2}$$

modification of so-called Hill[¶] equation, here normalized between suitable limits, was fitted to the spreading area data. It is generally used in biochemistry, and was recently adapted to describe cell spreading dynamics and motility [81, 148]. The A_{max} represents the maximum spreading area achieved after certain adhesion time and A_{min} the initial, "unspread" cell area. The so-called Hill's coefficient m describes the steepness of the transition, i.g. how fast the transition takes place with the change of substrate compliance E_Y. Fast transition, i.g. steep thresholds in spreading area corresponds to high values of m and slow transition to low values.

$E_{1/2}$ is the half saturation constant, the transition- or tactile set-point sensed by the cells. Obviously at this point cells react quasi-linearly. Therefore they can response with large changes of their spreading area on small substrate or tissue

[¶]Archibald Hill first proposed this equation to describe O_2 binding curve of hemoglobin

compliance changing. This results in the most largest margin in terms to quickly adapt to environmental changes.

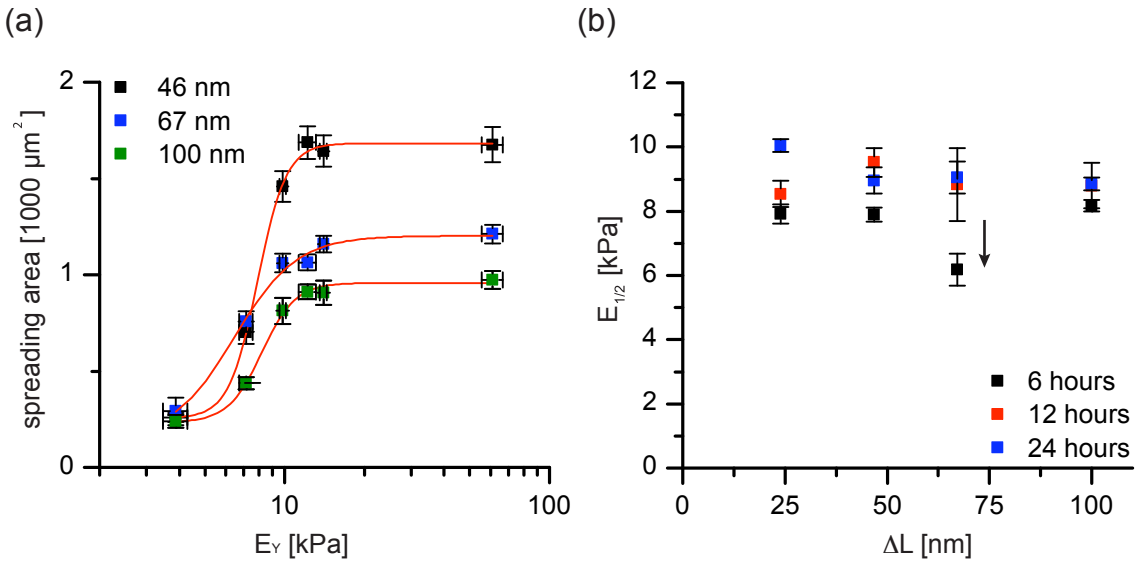

Figure 6.7: (a) Fit examples of the data measured 6 hours after seeding on elastic nanopatterned substrates featuring continuous variation of elastic modulus E_Y and binding site spacing of 45 nm, 67 nm and 100 nm, respectively. Half saturation constants $E_{1/2}$=7.86±0.12 kPa for 46 nm, $E_{1/2}$=6.18±0.5 kPa for 67 nm and $E_{1/2}$=8.17±0.2 kPa for 100 nm were calculated. χ^2_{45nm}=0.21, χ^2_{67nm}=1.16, χ^2_{100nm} = 0.23. The error in the spreading area refer to the standard error of the mean (b) Generalized half saturation constant $E_{1/2}$ values for 6 h, 12 h and 24 h of adhesion respectively. The error refer to the standard error of the mean $E_{1/2}$, calculated under consideration of weighting by the fit error.

The relation (6.2) was fitted to all acquired cell spreading area data. Fit examples are given in Figure 6.7a. Here, one can see the transition anomaly on substrates with binding sites spacing of 67 nm as described above (blue datapoints). On these substrates, the $E_{1/2}$ value was lower than that of cells on other substrates 6 hours after seeding. Considering the fact, that the integrin binding site spacing of 67 nm is actually the critical transition value, cellular sensing machinery can seriously be destabilized and may lead to affected mechanotransduction process. This surprising effect needs further, intensive investigations, which go beyond the scope of this work.

It turns out, that this shift of about 2 kPa is unique for the whole substrate system as denoted by the black arrow in Figure 6.7b. Small fluctuations of $E_{1/2}$ on substrates with different binding site spacings are present, but the one described above is the only dominant. Application of described model on all available substrates revealed a time-dependent development of $E_{1/2}$, which is summarized in Figure 6.8. Moreover, the Hill's coefficient m seems to be time dependent as well. Obviously, the tactile set-points, 6 hours after cell seeding, are significantly lower than the set-points

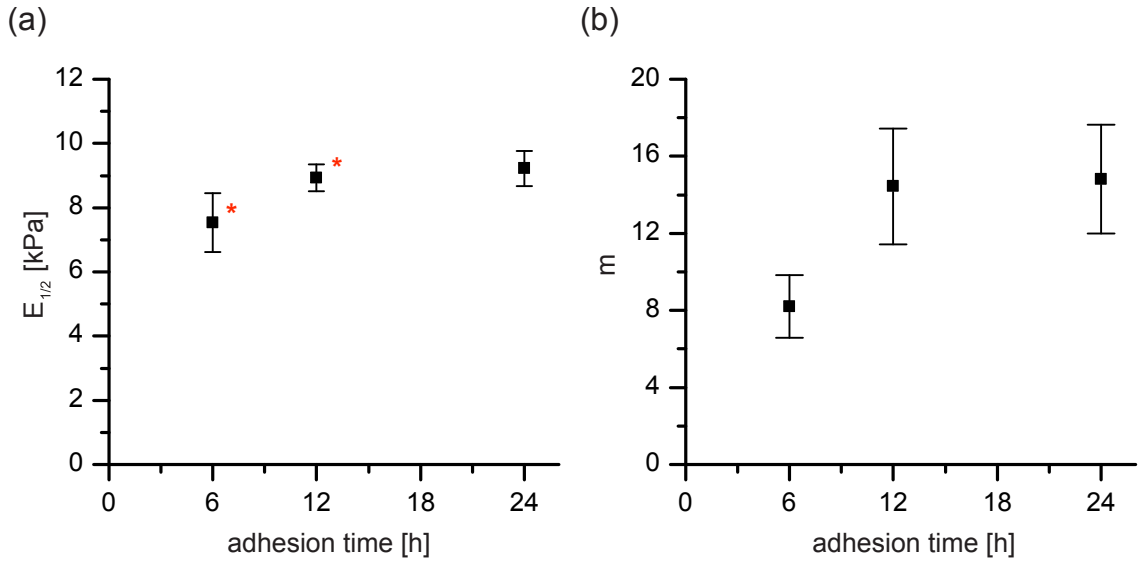

Figure 6.8: Statistical mean of calculated half saturation constants $E_{1/2}$ (a) and Hill's coefficient m (b). After 6 h, 12 h and 24 h of adhesion, respectively. Red stars in (b) denotes that these values are significantly different (p=0.046) from each other. The error bars refer to the standard error of the mean.

calculated 12 hours and 24 hours of adhesion, respectively. Moreover, an increase of Hill's coefficient m suggests time dependent changes in cellular transition and, thus the mechanosensinig behavior. The steepness of thresholds increased with adhesion time. This means that at least after 12 hours of adhesion cells can more strictly distinguish between rigid and soft substrates.

To verify these results and gain more detailed insight in force-driven mechnosensing processes, single cell force spectroscopy was performed as will be described in the next chapter.

Chapter

7

Single cell force spectroscopy on elastic nanopatterned ECM analogs

Cellular interactions with two-dimensional substrates, like migration and spreading, as well as controlled development of focal adhesion and mechanosensing processes are dependent on force, which is applied by the cell on the underlying substrate. Biophysical, stochastic models introduced in Chapter 2.2.1 suggest, that effective control of signaling processes within focal adhesion clusters most likely occurs close to the critical, stall force F_c applied by the cells on their surroundings via focal adhesions. Therefore, quantification of cell-substrate detachment or adhesion forces $F_{ADH} = F_c$ may give an important insight in processes described above.

In the late 90s SPM* was introduced as a tool to quantify cell-cell and cell-substrate adhesion forces [149, 150]. This very sensitive, force spectroscopy approach allows to determine a wide range of forces acting between cells or single proteins on scales ranging from several pN to tens of µN. The term single cell force spectroscopy (SCFS) was introduced for experiments, where forces between a cell and a substrate or another cell are measured [151].

7.1 Principle of single cell force spectroscopy

The basic principle of SCFS is illustrated in Figure 7.1. Here, REF YFP pax cells were plated on desired substrate for 6 to 8 hours, respectively. After cell spreading the substrates was transferred to SCFS, thus SPM experimental setup. There, a tipless, biofunctionalized cantilever with known spring constant k was gently approached from the top to allow cell-cantilever immobilization. After a certain contact time T_c, the cantilever was retracted and so-called force-distance curves were acquired by cantilever deflection, that was recorded during the separation process. Detailed experimental setup is presented in Chapter A.2.1

Stable cell-cantilever connection is required for successful cell detachment. Hence,

*SPM technique is described in detail in Chapter A.2.1

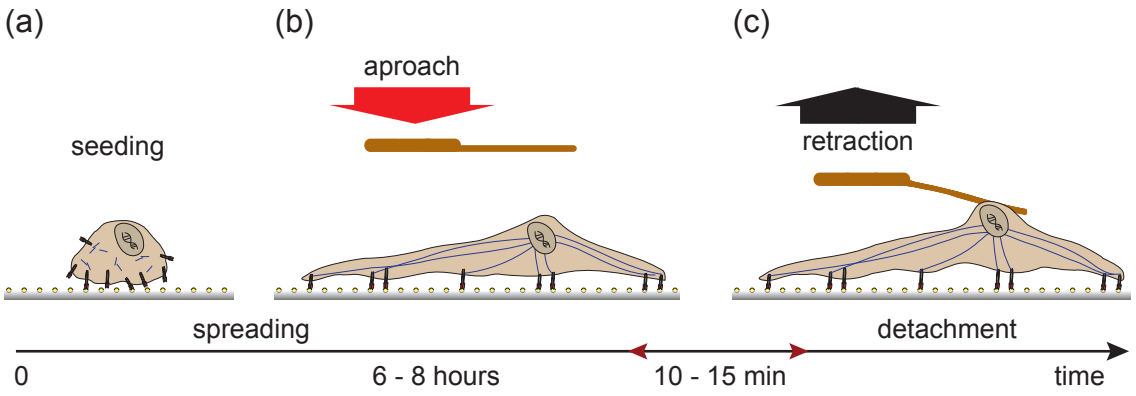

Figure 7.1: Single cell force spectroscopy as applied in presented experiments. After seeding the cells on the desired substrates and subsequent spreading (a) the substrate was transferred into the SPM apparatus. Then, a fibronectin-functionalized tipless cantilever was approached to the top of the cell (b). The cantilever-cell contact time was set to 10-15 min to establish resistant connection. During the retraction, cell-substrate detachment forces were measured (c).

the only way to detach adhering cells from the substrate is to induce adhesion contacts at the cell-cantilever interface of at least an equivalent strength. Moreover these contacts must be connected to the cytoskeleton to transmit forces applied by the cantilever to the cell-substrate interface. In all experiments presented here cantilever were functionalized by fibronectin in order to induce focal contact formation at the cell-cantilever interface. Fibronectin is an ECM protein, among others, responsible for cell adhesion as described in Chapter 1.3.3. It binds to the same $\alpha_V\beta_3$ integrin receptors as the c(RGDfK) peptide sequence immobilized on gold nanopatterns.

To avoid disturbance of the cell-substrate binding strength by a depletion of the integrin contacts the cantilever was touching the dorsal side of the cell for a relatively short contact time (10 min $< T_c <$ 15 min). Longer adhesion times were also tested, with presumable results in cell polarization towards the cantilever, which strongly affect cell-substrate interaction forces. The integrity of focal adhesions established by the cell on the substrate surface was verified by fluorescence microscopy prior the detachment where the fluorescence of YFP labeled paxilin was excited as shown in Figure 7.2.

Typical force-distance curve recorded during the approach and the detachment procedure are presented in Figure 7.3. In case of adhesion forces acting on the cantilever the values of force-distance curves are negative. They are positive if load, applied by the cantilever, is acting on the cell of interest. During the SCFS experiments initial loading of 10 nN was applied on the cell to facilitate the formation of strong cantilever-cell connection. To avoid cell damage the retraction velocity of the cantilever was set to 1 µm/s. Typical detachment process of the adhering cell is shown in Figure 7.3. This process is not spontaneous but rather occurs

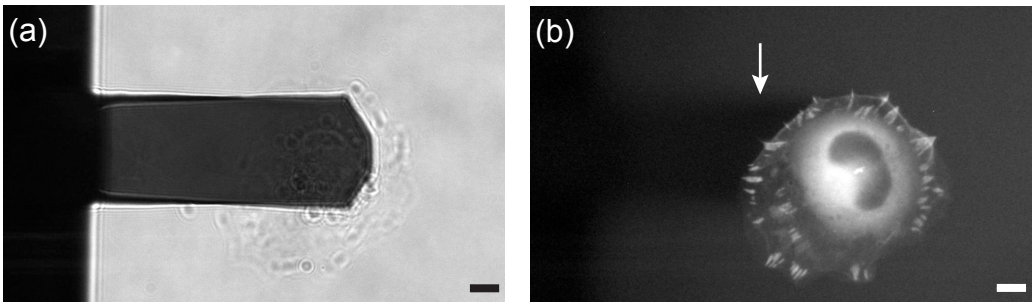

Figure 7.2: Phase contrast (a) and fluorescence micrographs (b) of a adherent REF YFP pax cell on elastic nanopatterned substrate just before the detachment process. The approached cantilever is clearly visible in (a) and is denoted by white arrow in (b). Scale bars 10 µm.

step by step with a tensional stretching of the cell in between the rupture events. This is in good agreement with the discrete adhesion sites established by the cell, through the cytoskeleton, on the substrate surface. The observed stretching most likely corresponds to elastic response of those parts of the cytoskeleton (e.g. actin filaments), which are connected to adhesion sites.

During the detachment focal adhesions first act as parallel loaded spring array with an effective spring constant $K = \sum K_i$ until the maximum force, which the array can resist, is reached. Since its arrangement is not regular, at certain time point first cell-substrate connections break, which results in fast zipping like rupture of all others. With each rupture, less adhesion sites participate in the detachment process, which leads to decaying force constant, thus lower gradients in elastic cell response between rupture steps as shown in Figure 7.3b.

The force constants of the elastic response of single step, recently quantified for REF YFP pax cells, is approximately 20 nN/µm [141]. The average number of detachment events observed during the SCFS experiments vary between 5 and 15. The overall spring constant of the aforementioned spring array could be approximated to 1-3 N/m which is in the same order of magnitude as the spring constants of used cantilevers. Therefore, good force transduction from the acting cantilever to the cellular adhesion sites could be assumed.

The nature of the detachment process discussed above suggests, that not the maximum force measured during the detachment process accords to the cellular adhesion force, but rather the sum of single forces corresponding to the single rupture events.

$$F_{ADH} = \sum_i f_i \tag{7.1}$$

Unfortunately, cells, even under same environmental conditions, feature different spreading areas and distributions of focal adhesions. In the case of spreading area experiments presented in Chapter 6.1, high number of investigated cells allowed to gain quantitative results. SCFS experiments are time-consuming and complex

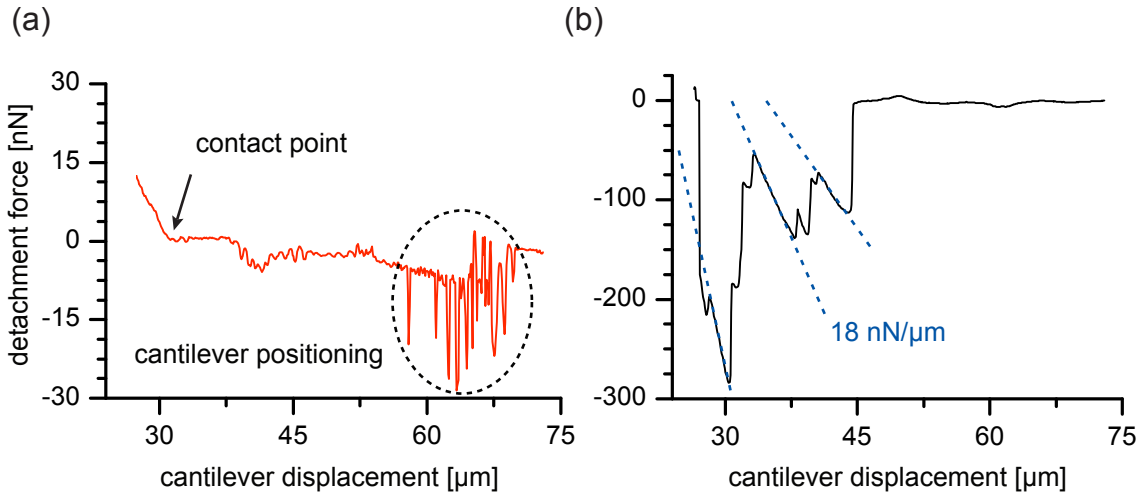

Figure 7.3: Typical SCFC force-distance curve. During the approach (a) the cantilever position was often readjusted to assure the best possible cell contact. Black arrow denotes cantilever-cell contact point. After the contact time T_c retraction was initiated (b). Blue dashed line denotes the regions where the cell is elastically stretched before rupture occurs. The force constant decreases with the number of detachment events.

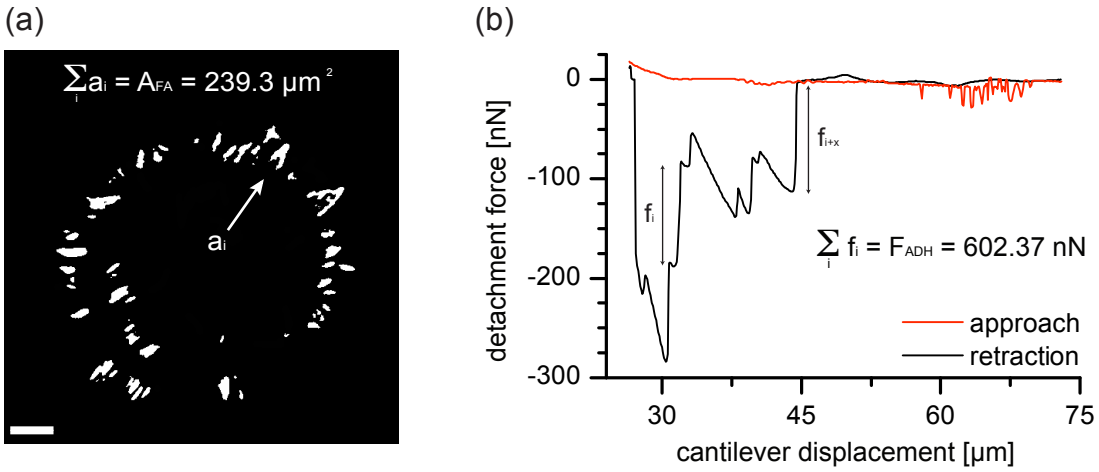

Figure 7.4: Calculation of adhesion force density, an example. (a) The total focal adhesion area A_{FA} is automatically calculated of each measured cell by homemade ImageJ macro. Therefore fluorescent micrograph (as shown in Fig. 7.2) was taken from the cell of interest straight before cantilever retraction. Scale bar 10 µm. (b) Typical force-distance curve recorded during SCFS experiment. The total adhesion force acquired F_{ADH}, acquired during the cantilever retraction, is the sum of several single detachment events corresponding to single focal adhesions.

to realize. For this reason, total adhesion force was normalized by the total focal adhesion area $A_{FA} = \sum a_i$, where a_i is the area of a single focal adhesion acquired by fluorescence microscopy and determined by standardized image processing routine. The so-called adhesion force density

$$\rho_{ADH} = \frac{F_{ADH}}{A_{FA}} \tag{7.2}$$

was defined. Overview of the ρ_{ADH} calculation procedure is presented in Figure 7.4.

7.2 Quantification of cell adhesion forces on elastic nanopatterned substrates

In the SCFC experiments presented here, REF YFP pax cells were cultured 6 to 8 hours on elastic nanopatterned substrates and glass surfaces. In the case of PEG-DA based substrates interparticle distances, thus integrin binding site spacings were hold constant at approximately 46 nm. Substrate elasticities were changed in the same way as in spreading area experiments between 3.8 kPa and 12.2 kPa respectively.

On stiff substrates binding sites spacings of 25 nm, 50 nm, 75 nm, 90 nm and 100 nm respectively were used. Between 5 and 14 cells per data point were measured. Results obtained on substrates with tunable binding site spacings are plotted over binding site density[†] for better comparison. Figure 7.5 presents measured total adhesion force F_{ADH} and adhesion force density ρ_{ADH}.

Obviously, total adhesion forces are not suitable for quantitative determination of cell-substrates interaction forces. As can be observed in Figure 7.5a and b, decrease of detachment forces is distinguishable. In case of compliance variations it seems to be linear. No threshold in detachment force can be observed. If binding site spacing is tuned, certain transition of cell-substrate forces are visible. The only result, which can be gained from this observations is that the cell-substrate total interaction force is quite strong. The maximum force ranges from F_{ADH}=1.0 µN to 1.2 µN. Assuming integrin expression level of approximately 10^5 molecules per cell [152] one can calculate ≈ 10-12 pN per integrin. This value lies within reported order of magnitude of single integrin-fibronectin interaction forces at low loading rates of 35±27 pN.

To gain quantitative statement about cell-surface interaction forces, the measured total adhesion forces were normalized by focal adhesion area as described in equation (7.2). On rigid substrates and small binding sites spacings (high binding site densities) maximum adhesion force densities of approximately 3.5-5 nN/µm^2 could be measured. In literature, where substrate distortion was used to visualize adhesion forces, adhesion force densities between 2 and 10 nN/µm^2 are reported

[†]The global interparticle density was calculated as $\rho_{ADH} = \frac{2/}{\sqrt{3}} \frac{particles}{\Delta L^2}$

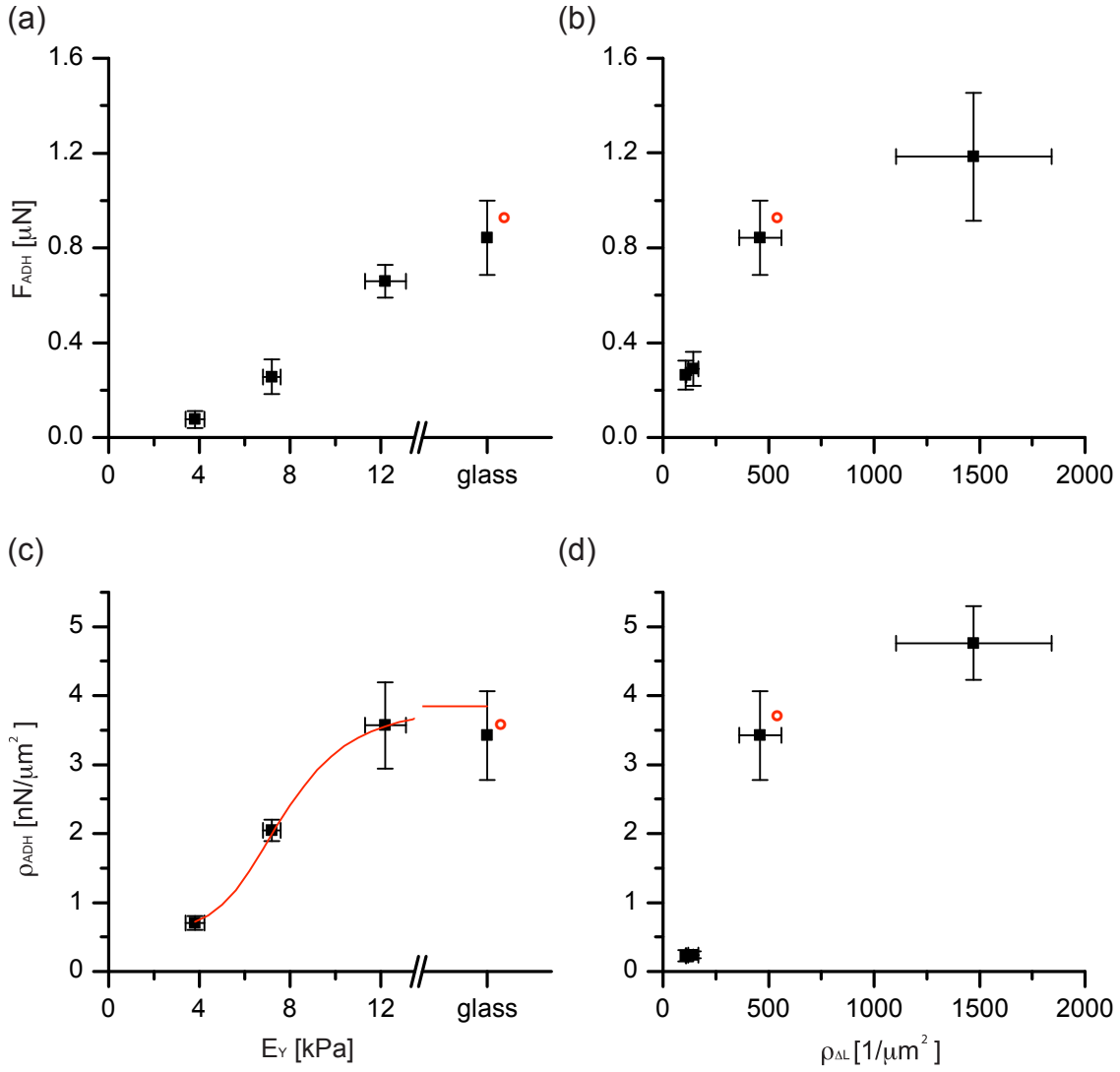

Figure 7.5: Total adhesion F_{ADH} (a)-(b) and adhesion force density ρ_{ADH} (c)-(d) measured by SCFS experiments. The red circles marks identical datapoint plotted in corresponding graphs. Modified Hill equation (6.2) was fitted in (c), $E_{1/2}$= 7,65±0.4 kPa, χ^2=0.29. (b) and (d) adapted from [141]. the error in total adhesion force and adhesion force density refer to the standard error of mean.

[45, 79, 153]. This is in good agreement with results presented here. According to Figure 7.5c and d, two clear transitions in adhesion forces per focal adhesion area can be distinguished.

When substrate rigidity is changed ρ_{ADH} development is very similar to the development of cell spreading area presented in Chapter 6.3. To calculate the tactile set-point of cellular mechanosensing, half saturation constant $E_{1/2}$ was calculated according to the modified Hill equation presented above. In contrast to the spreading area experiments, were cells feature initial spreading area A_{min}, adhesion forces of $F_{ADF} = 0$ are possible. Therefore, the equation (6.2) was modified as

$$\rho_{ADH}(E_Y) = \rho_{ADHmax} \frac{E_Y^m}{E_{1/2}^m + E_Y^m} \tag{7.3}$$

Fitting this relation to the data presented in Figure 7.5c yielded $E_{1/2}$= 7,65±0.4 kPa and $m = 5.1 \pm 2.3$, respectively. This is in very good agreement with the values gained from spreading area investigations. As shown in Table 7.1 the tactile set-points of cellular mechanosensing determined with two very different methods are identical within errors. This fact suggest, that elasticity of cellular environment and thus tissue elasticity can globally affect cellular behavior.

Table 7.1: Comparison of cellular mechanosensing tactile set-points $E_{1/2}$ gained from spreading area determination and SCFS 6 h after seeding.

measured value	$E_{1/2}$[kPa]	m	χ^2	ΔL [nm]
A	7.86±0.12	8.0±0.8	0.21	46
ρ_{ADH}	7,65±0.4	5.1±2.3	0.29	46

Unfortunately, the model utilized above does not deliver appropriate results if fitted to the data where distance or density of integrin binding sites is varied. This is quite reasonable since integrin cooperativity and clustering, responsible for force transduction between the cytoskeleton and ECM, follow essential complex stochastic models as shown in Chapter 2.2.1.

Experiments presented within previous chapters yield various interesting results in terms of quantification and further understanding of cellular reactions on changing environmental parameters. Detailed discussion and general concusions will be presented in Part V.

Part V

Conclusions and Outlook

Chapter

8

Conclusions

A better understanding how tissue is formed and maintained is of great biological and medical interest. Cells can build-up, modify and change the tissue and its properties. Research in this field, performed in the last decades, has gained outstanding results and enriches the understanding of this processes. Within this thesis, a small but hopefully important building block was added to this complex and still developing knowledge meshwork.
The presented experiments can be roughly divided into two parts: development of artificial ECM analogs and its biophysical application.

- Substrates with well defined and precisely tunable properties were developed to mimic biophysical and biochemical properties of connective tissues. The extensive substrate characterization could show that substrate elasticity as well as spacing of binding sites, providing cellular adhesion, can be adjusted to the majority of physiologically reasonable properties. The elastic modulus of the substrate system could be successfully tuned within four orders of magnitude (0.6 kPa$< E_Y <$6 MPa). Simultaneously, the binding site spacing could be varied between 20 nm and 120 nm, respectively. This resulted in a two-dimensional system of environmental parameters, tuned independently from each other.

Application of this system to rat embryonic fibroblasts gave important insights in cellular environmental-sensing processes. Cellular adhesion in general and cellular response on changing environmental stimuli in particular were investigated. Cellular growth and adhesion revealed tactile set-points of mechanosensing and sensing of binding site spacing and density. These set-points of approximately 8 kPa and 70 nm were already known from the literature and were precisely reproduced to approve the utilized substrate system.
Two major conclusions could be drawn:

- First: Hierarchy of environmental stimuli were found. Due to the application of two different experimental approaches, the elasticity of cellular environment turned out to be the parameter, dominating global cellular behavior. Figure

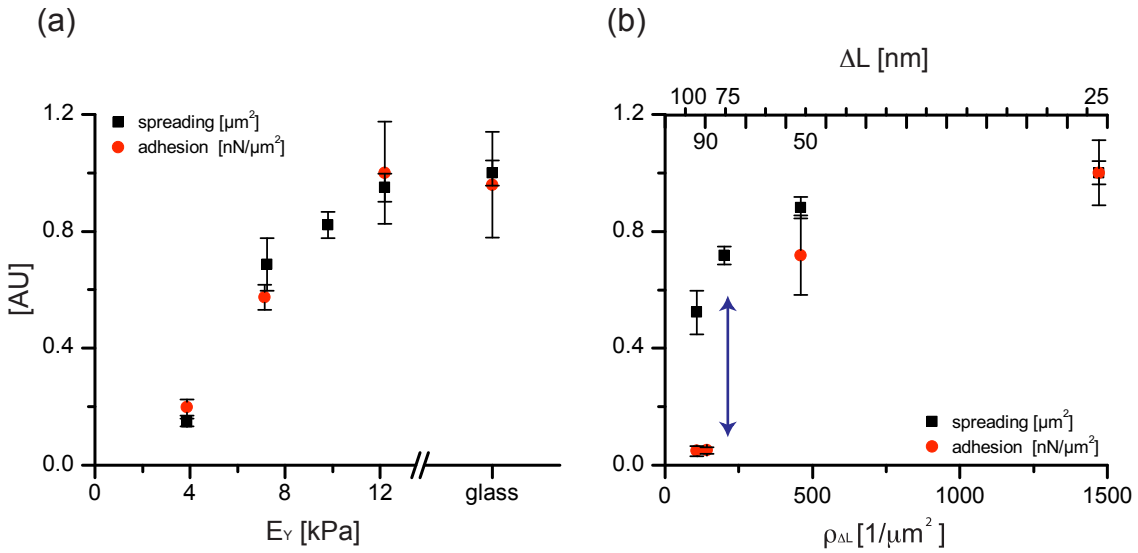

Figure 8.1: Comparison of results gained in performed experiments. (a) normalized cell spreading area and adhesion force density plotted against varying substrate elasticity. The signals feature nearly identical progression. (b) same variables, but plotted over binding site density. Great signal difference could be distinguish as denoted by the blue arrow.

8.1a summarizes the results of yielded cell spreading area and cellular adhesion forces. Identical cellular response was measured when the elastic modulus of the substrates were changed. This means, that the elasticity of cellular surrounding dominates both measured cellular reactions, thus global cellular behavior. When binding site spacing or density was varied (Fig. 8.1b), a great difference in cellular response could be observed. Here, the cellular sensing machinery is strongly disturbed at the molecular level (adhesion forces). Nevertheless cells are able to globally adapt to these conditions (spreading area).
The domination of mechanosensing was revealed during the investigations of cellular growth rates, as shown in Figure 8.2. According to the gained tactile set-points, substrates could be assumed to be hard (+) when they are stiffer than 8 kPa and soft (-) when not. The binding site spacing on their surface could be defined as low (+) when less than 70 nm and high (-) when not. Comparison of so defined valency of substrate properties with calculated cellular growth rates revealed an anomaly in cellular behavior. On hard and low-spaced substrates (+ +), cells showed the highest growth rate (red). On soft and high spaced substrate (- -), cellular growth rate was low (blue). Consequently, in case of alternating substrate properties and equivalent weighting, one would expect intermediate growth rate (green) as it was measured on high binding site spaced and hard substrates (- +). Surprisingly, cell feature less or no growth (blue) on low spaced and soft substrates (+ -).
From this follows that, receiving "negative" results from monitoring biophysi-

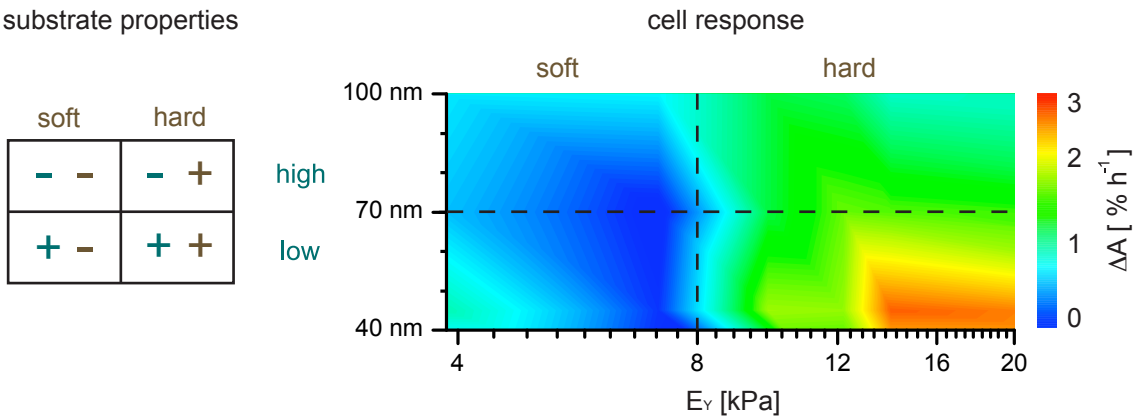

Figure 8.2: Cellular growth rate between 6th and 24th hour of adhesion, compared with the valency of substrate properties.

cal properties of surrounding environment, performed at early spreading state, crucially dominates further cellular development. This supports a recently introduced so called hierarchical phase model [144]. In this model, cells develop in phases. Different dynamic phases correspond to different functional regions in relating parameter space. The phases are sequences of transitions, i.e. trajectories in this parameter space, which is determined by cellular signaling network. Some signals (e.g mechanosensing) are able to initiate or inhibit this trajectories, thus "switch" cells from one phase to the other or freeze them in a certain phase. Other signals are not as dominant. They crucially affect cellular behavior but have less or no influence on phase sequence. The mechanosensing signal, that originates from soft environment definitely stops phase transitions. In contrast, disturbed integrin clustering, that originates from high spacing of binding sites most likely does not.

- And second: Cells feature precise selectivity in quantification of environmental signals. It could be shown, that a certain experimental parameter space exists, where cell growth is maximal. It lies approximately between 12 kPa and 50 kPa rigid substrates and 35 nm to 60 nm spaced integrin binding sites, respectively. This matches the biophysical and biochemical values of physiological properties of connective tissues, where used cells stem from. It is very remarkable, that cells and their sensing apparatus, can selectively recognize and judge this environmental stimuli.

Chapter

9

Outlook

We were able to show that elastic nanopatterned substrates are suitable for mimicking crucial biochemical and biophysical properties of connective tissues. Biological conclusions could be drawn, concerning the effect and hierarchy of sensing of different environmental stimuli on cellular behavior. However, many questions remain unanswered. Especially the molecular mechanisms underlying mechnosensing within focal adhesions may be clarified through investigations of integrin activation processes or phosphorylation of adaptor or signaling proteins like FAK or p130Cas.

The substrate system developed in this work, opens a wide field for further investigations on cellular behavior. Nevertheless, its characteristics spectrum is not complete. For instance, nanoparticle arrays that consist of micrometer-sized patches of nanopatterns surrounded by non-structured areas, so-called micro-nanostructures, could be transferred onto PEG-DA hydrogel surface to decouple the relation between particle spacing and density [125]. And therefore, enrich the substrate system by an additional environmental parameter.

Moreover, different types of tissues may be mimicked with the presented substrates, e.g. epithelial, muscle, nervous and connective tissue. This could be achieved by varying substrate mechanical properties within expanded limits and utilization of different peptides (e.g. IKVAV*) for biofunctionalization.

The focus of further investigations could be shifted from mechanosensing to cell-cell and cell-matrix signaling processes. Biophysical adjustability of the presented substrate system may be used to guarantee suitable mechanical micronenvironments and variable proteins and peptides could be used to study e.g. differentiation of stem cells, mechanisms of the immune response and morphogenesis. During the last decades, stem cell research has become more and more important. Elastic nanopatterned PEG-DA hydrogels could be utilized to move closer towards a universal physiological stem cell niches.

*The IKVAV (Ile-Lys-Val-Ala-Val) is a sequence of the ECM protein laminin and mediates cell attachment, migration, and neurite outgrowth [154].

List of Figures

Bibliography

[1] Alberts, B., Bray, D., Lewis, J., Raff, M., Roberts, K., and Watson, J.D. *The cell*. **2002**. 6, 7, 9

[2] Thoumine, O. and Ott, A. Time scale dependent viscoelastic and contractile regimes in fibroblasts probed by microplate manipulation. *Journal of cell science*, 110, (17): 2109–2116, **1997**. 6

[3] Herrmann, H. and Aebi, U. Intermediate filaments and their associates: multi-talented structural elements specifying cytoarchitecture and cytodynamics. *Current Opinion in Cell Biology*, 12, (1): 79–90, **2000**. 6

[4] Goldman, RD, Khuon, S., Chou, YH, Opal, P., and Steinert, PM. The function of intermediate filaments in cell shape and cytoskeletal integrity. *Journal of Cell Biology*, 134, (4): 971–983, **1996**. 6

[5] Brangwynne, C.P., MacKintosh, F.C., Kumar, S., Geisse, N.A., Talbot, J., Mahadevan, L., Parker, K.K., Ingber, D.E., and Weitz, D.A. Microtubules can bear enhanced compressive loads in living cells because of lateral reinforcement. *Journal of Cell Biology*, 173, (5): 733, **2006**. 7

[6] Geiger, B., Yehuda-Levenberg, S., and Bershadsky, AD. Molecular interactions in the submembrane plaque of cell-cell and cell-matrix adhesions. *Acta anatomica*, 154: 46–62, **1995**. 7

[7] Gartner, L.P., Hiatt, J.L., and Strum, J.M. *Cell biology and histology*. Lippincott Williams & Wilkins, **2006**. 7

[8] Welsch, U. *Sobotta Lehrbuch Histologie Zytologie, Histologie, mikroskopische Anatomie*. Urban & Fischer in Elsevier, **2006**. 7

[9] Even-Ram, S. and Yamada, K.M. Cell migration in 3D matrix. *Current opinion in cell biology*, 17, (5): 524–532, **2005**. 8

[10] Diridollou, S., Patat, F., Gens, F., Vaillant, L., Black, D., Lagarde, JM, Gall, Y., and Berson, M. In vivo model of the mechanical properties of the human skin under suction. *Skin Research and Technology*, 6, (4): 214–221, **2000**. 8, 73

[11] Meller, D., Peters, K., and Meller, K. Human cornea and sclera studied by atomic force microscopy. *Cell and tissue research*, 288, (1): 111–118, **1997**. 9, 14, 33

[12] Emsley, J., Knight, C.G., Farndale, R.W., Barnes, M.J., and Liddington, R.C. Structural basis of collagen recognition by integrin $\alpha 2\beta 1$. *Cell*, 101, (1): 47–56, **2000**. 8, 14

[13] Pankov, Roumen and Yamada, Kenneth M. Fibronectin at a glance. *J Cell Sci*, 115, (20): 3861–3863, **2002**. 9

[14] Ruoslahti, E. and Oebrink, B. Common principles in cell adhesion. *Experimental cell research*, 227, (1): 1–11, **1996**. 9

[15] Cavalcanti-Adam, E.A., Tomakidi, P., Bezler, M, and Spatz, J.P. Geometric organization of the extracellular matrix in the control of integrin-mediated adhesion and cell function in osteoblasts. *Prog Orthod*, 6, (2): 232–237, **2005**. 9, 14

[16] Carman, C.V. and Springer, T.A. Integrin avidity regulation: are changes in affinity and conformation underemphasized? *Current opinion in cell biology*, 15, (5): 547–556, **2003**. 10, 11

[17] van Kooyk, Y. and Figdor, C.G. Avidity regulation of integrins: the driving force in leukocyte adhesion. *Current opinion in cell biology*, 12, (5): 542–547, **2000**. 10

[18] Lodish, H., Berk, A., Zipursky, SL, Matsudaira, P., Baltimore, D., and Darnell, JE. *Molecular biology of the cell*. New York, Scientific American Books, **1995**. 10

[19] Rosen, S.D. Ligands for L-selectin: homing, inflammation, and beyond. **2004**. 10

[20] Geiger, B., Bershadsky, A., Pankov, R., and Yamada, K.M. Transmembrane crosstalk between the extracellular matrix and the cytoskeleton. *Nature Reviews Molecular Cell Biology*, 2, (11): 793–805, **2001**. 10, 15

[21] Beckerle, Mary C. *Cell adhesion*. Oxford university press, **2001**. 10

[22] Hynes, R.O. Integrins: versatility, modulation, and signaling in cell adhesion. *Cell*, 69, (1): 11–25, **1992**. 10, 11, 12

[23] Bray, D., Levin, M.D., and Morton-Firth, C.J. Receptor clustering as a cellular mechanism to control sensitivity. *Nature*, 393, (6680): 85–88, **1998**. 12

[24] Zaidel-Bar, R., Ballestrem, C., Kam, Z., and Geiger, B. Early molecular events in the assembly of matrix adhesions at the leading edge of migrating cells. *Journal of Cell Science*, 116, (22): 4605–4613, **2003**. 12, 14

[25] Adams, JC. Cell-matrix contact structures. *Cellular and Molecular Life Sciences (CMLS)*, 58, (3): 371–392, **2001**. 13

[26] Cohen, M., Klein, E., Geiger, B., and Addadi, L. Organization and adhesive properties of the hyaluronan pericellular coat of chondrocytes and epithelial cells. *Biophysical journal*, 85, (3): 1996–2005, **2003**. 13

[27] Schmidt, CE, Horwitz, AF, Lauffenburger, DA, and Sheetz, MP. Integrin-cytoskeletal interactions in migrating fibroblasts are dynamic, asymmetric, and regulated. *Journal of Cell Biology*, 123, (4): 977–991, **1993**. 13

[28] Mitra, S.K., Hanson, D.A., and Schlaepfer, D.D. Focal adhesion kinase: in command and control of cell motility. *Nature Reviews Molecular Cell Biology*, 6, (1): 56–68, **2005**. 13

[29] Riveline, D., Zamir, E., Balaban, N.Q., Schwarz, U.S., Ishizaki, T., Narumiya, S., Kam, Z., Geiger, B., and Bershadsky, A.D. Focal contacts as mechanosensors externally applied local mechanical force induces growth of focal contacts by an mDia1-dependent and ROCK-independent mechanism. *Journal of Cell Biology*, 153, (6): 1175–1186, **2001**. 14, 29

[30] Bershadsky, A., Kozlov, M., and Geiger, B. Adhesion-mediated mechanosensitivity: a time to experiment, and a time to theorize. *Current opinion in cell biology*, 18, (5): 472–481, **2006**. 14, 29

[31] Zaidel-Bar, R., Itzkovitz, S., Ma'ayan, A., Iyengar, R., and Geiger, B. Functional atlas of the integrin adhesome. *Nature cell biology*, 9, (8): 858–867, **2007**. 14, 30

[32] Lock, J.G., Wehrle-Haller, B., and Stroemblad, S. Cell-matrix adhesion complexes: master control machinery of cell migration. **2007**. 14

[33] Berrier, A.L. and Yamada, K.M. Cell-matrix adhesion. *Journal of cellular physiology*, 213, (3), **2007**.

[34] Ingber, D.E. Cellular mechanotransduction: putting all the pieces together again. *The FASEB Journal*, 20, (7): 811, **2006**. 14, 29

[35] A., Cavalcanti-Adam E., Aydin, D., Hirschfeld-Warneken, V.C., and Spatz, J. P. Cell adhesion and response to synthetic nanopatterned environments by steering receptor clustering and spatial location. *HFSP J*, 2, (5): 276–285, Oct 2008. 14, 29, 64

[36] Maheshwari, G., Brown, G., Lauffenburger, DA, Wells, A., and Griffith, LG. Cell adhesion and motility depend on nanoscale RGD clustering. *Journal of Cell Science*, 113, (10): 1677–1686, **2000**. 14

[37] Koo, L.Y., Irvine, D.J., Mayes, A.M., Lauffenburger, D.A., and Griffith, L.G. Co-regulation of cell adhesion by nanoscale RGD organization and mechanical stimulus. *Journal of cell science*, 115, (7): 1423–1433, **2002**. 14

[38] Massia, SP and Hubbell, JA. An RGD spacing of 440 nm is sufficient for integrin alpha V beta 3-mediated fibroblast spreading and 140 nm for focal contact and stress fiber formation. *Journal of Cell Biology*, 114, (5): 1089–1100, **1991**. 14, 29

[39] Hirschfeld-Warneken, Vera C, Arnold, Marco, Cavalcanti-Adam, Ada, Lpez-Garca, Mnica, Kessler, Horst, and Spatz, Joachim P. Cell adhesion and polarisation on molecularly defined spacing gradient surfaces of cyclic rgdfk peptide patches. *Eur J Cell Biol*, 87, (8-9): 743–750, Sep 2008. 29, 53

[40] Arnold, M., Cavalcanti-Adam, E.A., Glass, R., J., Bluemmel., Eck, W., Kantlehner, M., Kessler, H., and Spatz, J.P. Activation of integrin function by nanopatterned adhesive interfaces. *Chemphyschem*, 5, (3): 383–388, Mar 2004. 14, 29, 69, 71

[41] Yan, B., Calderwood, D.A., Yaspan, B., and Ginsberg, M.H. Calpain cleavage promotes talin binding to the $\beta 3$ integrin cytoplasmic domain. *Journal of biological chemistry*, 276, (30): 28164–28170, **2001**. 15

[42] Cluzel, C., Saltel, F., Lussi, J., Paulhe, F., Imhof, B.A., and Wehrle-Haller, B. The mechanisms and dynamics of $\alpha \mathrm{v} \beta 3$ integrin clustering in living cells. *The Journal of cell biology*, 171, (2): 383, **2005**. 15, 64

[43] Calderwood, D.A. and Ginsberg, M.H. Talin forges the links between integrins and actin. *Nature Cell Biology*, 5, (8): 694–697, **2003**. 15

[44] Geiger, B. and Bershadsky, A. Exploring the neighborhood adhesion-coupled cell mechanosensors. *Cell*, 110, (2): 139–142, **2002**. 15, 19, 29

[45] Balaban, N.Q., Schwarz, U.S., Riveline, D., Goichberg, P., Tzur, G., Sabanay, I., Mahalu, D., Safran, S., Bershadsky, A., Addadi, L., et al. Force and focal adhesion assembly: a close relationship studied using elastic micropatterned substrates. *Nature cell biology*, 3, (5): 466–472, **2001**. 15, 29, 83

[46] Nicolas, A., Geiger, B., and Safran, S.A. Cell mechanosensitivity controls the anisotropy of focal adhesions. *Proceedings of the National Academy of Sciences*, 101, (34): 12520–12525, **2004**. 15, 29

[47] Novak, I.L., Slepchenko, B.M., Mogilner, A., and Loew, L.M. Cooperativity between cell contractility and adhesion. *Physical review letters*, 93, (26): 268109, **2004**.

[48] Schwarz, U.S., Erdmann, T., and Bischofs, I.B. Focal adhesions as mechanosensors: the two-spring model. *BioSystems*, 83, (2-3): 225–232, **2006**. 15, 26, 29

[49] Bruinsma, R. Theory of force regulation by nascent adhesion sites. *Biophysical journal*, 89, (1): 87–94, **2005**. 15

[50] Besser, A. and Safran, S.A. Force-induced adsorption and anisotropic growth of focal adhesions. *Biophysical journal*, 90, (10): 3469–3484, **2006**. 15, 25

[51] Chen, B.H., Tzen, J.T.C., Bresnick, A.R., and Chen, H.C. Roles of Rho-associated kinase and myosin light chain kinase in morphological and migratory defects of focal adhesion kinase-null cells. *Journal of Biological Chemistry*, 277, (37): 33857–33863, **2002**. 15

[52] Wang, Y., Botvinick, E.L., Zhao, Y., Berns, M.W., Usami, S., Tsien, R.Y., and Chien, S. Visualizing the mechanical activation of Src. *Nature*, 434, (7036): 1040–1045, **2005**.

[53] von Wichert, G., Jiang, G., Kostic, A., De Vos, K., Sap, J., and Sheetz, M.P. RPTP-α acts as a transducer of mechanical force on αv/β3-integrin-cytoskeleton linkages. *Journal of Cell Biology*, 161, (1): 143–153, **2003**. 15

[54] Kostic, A. and Sheetz, M.P. Fibronectin rigidity response through Fyn and p130Cas recruitment to the leading edge. *Molecular biology of the cell*, 17, (6): 2684–2695, **2006**. 15

[55] del Rio, A., Perez-Jimenez, R., Liu, R., Roca-Cusachs, P., Fernandez, J.M., and Sheetz, M.P. Stretching single talin rod molecules activates vinculin binding. *Science*, 323, (5914): 638, **2009**. 15

[56] Jiang, G., Huang, A.H., Cai, Y., Tanase, M., and Sheetz, M.P. Rigidity Sensing at the Leading Edge through αvβ3 Integrins and RPTPα. *Biophysical journal*, 90, (5): 1804–1809, **2006**. 15, 29

[57] Vogel, V. and Sheetz, M. Local force and geometry sensing regulate cell functions. *Nature Reviews Molecular Cell Biology*, 7, (4): 265–275, **2006**. 15, 16, 29, 64

[58] Fung, Y.C. Biomechanics: mechanical properties of living tissues. **1993**. 20

[59] Thoumine, O., Ott, A., Cardoso, O., and Meister, J.J. Microplates: a new tool for manipulation and mechanical perturbation of individual cells. *Journal of biochemical and biophysical methods*, 39, (1-2): 47–62, **1999**. 20

[60] Fernández, P., Pullarkat, P.A., and Ott, A. A master relation defines the nonlinear viscoelasticity of single fibroblasts. *Biophysical journal*, 90, (10): 3796–3805, **2006**. 21

[61] Schmitz, J., Benoit, M., and Gottschalk, K.E. The viscoelasticity of membrane tethers and its importance for cell adhesion. *Biophysical Journal*, 95, (3): 1448–1459, **2008**. 21

[62] Bell, GI. Models for the specific adhesion of cells to cells. *Science*, 200, (4342): 618, **1978**. 22, 25, 27

[63] Green, N.M. Avidin and streptavidin. *Methods Enzymol*, 184: 51–67, **1990**. 22

[64] Kramers, HA. Brownian motion in a field of force and the diffusion model of chemical reactions. *Physica*, 7, (4): 284–304, **1940**. 23

[65] Evans, E. and Ritchie, K. Dynamic strength of molecular adhesion bonds. *Biophysical Journal*, 72, (4): 1541–1555, **1997**. 23

[66] Merkel, R., Nassoy, P., Leung, A., Ritchie, K., and Evans, E. Energy landscapes of receptor-ligand bonds explored with dynamic force spectroscopy. *Nature*, 397, (6714): 50–53, **1999**. 23

[67] Zhang, X., Wojcikiewicz, E., and Moy, V.T. Force spectroscopy of the leukocyte function-associated antigen-1/intercellular adhesion molecule-1 interaction. *Biophysical journal*, 83, (4): 2270–2279, **2002**.

[68] Marshall, B.T., Sarangapani, K.K., Lou, J., McEver, R.P., and Zhu, C. Force history dependence of receptor-ligand dissociation. *Biophysical journal*, 88, (2): 1458–1466, **2005**.

[69] Wojcikiewicz, E.P., Abdulreda, M.H., Zhang, X., and Moy, V.T. Force spectroscopy of LFA-1 and its ligands, ICAM-1 and ICAM-2. *Biomacromolecules*, 7, (11): 3188, **2006**. 23, 24

[70] Li, F., Redick, S.D., Erickson, H.P., and Moy, V.T. Force Measurements of the $\alpha 5 \beta 1$ Integrin–Fibronectin Interaction. *Biophysical journal*, 84, (2): 1252–1262, **2003**. 23, 114

[71] Essevaz-Roulet, B., Bockelmann, U., and Heslot, F. Mechanical separation of the complementary strands of DNA. *Proceedings of the National Academy of Sciences*, 94, (22): 11935–11940, **1997**. 25

[72] Nicolas, A. and Safran, SA. Elastic deformations of grafted layers with surface stress. *Physical Review E*, 69, (5): 51902, **2004**. 25

[73] Erdmann, T. and Schwarz, US. Stability of adhesion clusters under constant force. *Physical review letters*, 92, (10): 108102, **2004**. 25, 29

[74] Seifert, U. Rupture of multiple parallel molecular bonds under dynamic loading. *Physical Review Letters*, 84, (12): 2750–2753, **2000**. 26, 29

[75] Schwarz, U.S., Erdmann, T., and Bischofs, I.B. Focal adhesions as mechanosensors: the two-spring model. *BioSystems*, 83, (2-3): 225–232, **2006**. 26

[76] Wong, J.Y., Velasco, A., Rajagopalan, P., and Pham, Q. Directed movement of vascular smooth muscle cells on gradient-compliant hydrogels. *J. Cell Sci*, 112: 1967, **1999**. 27, 28

[77] Lo, C.M., Wang, H.B., Dembo, M., and Wang, Y. Cell movement is guided by the rigidity of the substrate. *Biophysical journal*, 79, (1): 144–152, **2000**. 27, 28, 64

[78] Cheung, Y.K., Azeloglu, E.U., Shiovitz, D.A., Costa, K.D., Seliktar, D., and Sia, S.K. Microscale Control of Stiffness in a Cell-Adhesive Substrate Using Microfluidics-Based Lithography. *Angewandte Chemie International Edition*, **2009**. 28

[79] Beningo, K.A. and Wang, Y.L. Flexible substrata for the detection of cellular traction forces. *Trends in Cell Biology*, 12, (2): 79–84, **2002**. 29, 83

[80] Wang, Y.L. and Pelham, RJ. *Preparation of a flexible, porous polyacrylamide substrate for mechanical studies of cultured cells*, volume 298. Elsevier, **1998**. 29, 37

[81] Engler, A.J., Richert, L., Wong, J.Y., Picart, C., and Discher, D.E. Surface probe measurements of the elasticity of sectioned tissue, thin gels and polyelectrolyte multilayer films: correlations between substrate stiffness and cell adhesion. *Surface Science*, 570, (1-2): 142–154, **2004**. 29, 65, 73

[82] Discher, D.E., Janmey, P., and Wang, Y. Tissue cells feel and respond to the stiffness of their substrate. *Science*, 310, (5751): 1139–1143, **2005**. 33, 58, 68

[83] Zajac, A.L. and Discher, D.E. Cell differentiation through tissue elasticity-coupled, myosin-driven remodeling. *Current Opinion in Cell Biology*, 20, (6): 609–615, **2008**. 29, 69

[84] Yeung, T., Georges, P.C., Flanagan, L.A., Marg, B., Ortiz, M., Funaki, M., Zahir, N., Ming, W., Weaver, V., and Janmey, P.A. Effects of substrate stiffness on cell morphology, cytoskeletal structure, and adhesion. *Cell motility and the cytoskeleton*, 60, (1): 24–34, **2005**. 29

[85] Tang, Y., Yoo, J., Yethiraj, A., Cui, Q., and Chen, X. Mechanosensitive Channels: Insights from Continuum-Based Simulations. *Cell biochemistry and biophysics*, 52, (1): 1–18, **2008**. 29

[86] Paul, R., Heil, P., Spatz, J.P., and Schwarz, U.S. Propagation of mechanical stress through the actin cytoskeleton toward focal adhesions: model and experiment. *Biophysical Journal*, 94, (4): 1470–1482, **2008**. 29

[87] Chen, C.S., Mrksich, M., Huang, S., Whitesides, G.M., and Ingber, D.E. Geometric control of cell life and death. *Science*, 276, (5317): 1425, **1997**. 29, 30

[88] Dubin-Thaler, B.J., Giannone, G., Doebereiner, H.G., and Sheetz, M.P. Nanometer analysis of cell spreading on matrix-coated surfaces reveals two distinct cell states and STEPs. *Biophysical journal*, 86, (3): 1794–1806, **2004**. 29, 68, 69

[89] Engler, A., Bacakova, L., Newman, C., Hategan, A., Griffin, M., and Discher, D. Substrate compliance versus ligand density in cell on gel responses. *Biophysical journal*, 86, (1): 617–628, **2004**. 30, 58

[90] Graeter, S.V., Huang, J., Perschmann, N., Lopez-Garcia, M., Kessler, H., Ding, J., and Spatz, J.P. Mimicking cellular environments by nanostructured soft interfaces. *Nano Lett*, 7, (5): 1413–1418, May 2007. 30, 38, 49

[91] Schwarz, U.S. and Bischofs, I.B. Physical determinants of cell organization in soft media. *Medical Engineering and Physics*, 27, (9): 763–772, **2005**. 30

[92] Geiger, Benjamin, Spatz, Joachim P, and Bershadsky, Alexander D. Environmental sensing through focal adhesions. *Nat Rev Mol Cell Biol*, 10, (1): 21–33, Jan 2009. 30

[93] Stupack, D.G., Puente, X.S., Boutsaboualoy, S., Storgard, C.M., and Cheresh, D.A. Apoptosis of adherent cells by recruitment of caspase-8 to unligated integrins. *Journal of Cell Biology*, 155, (3): 459–470, **2001**. 30

[94] Beglova, N., Blacklow, S.C., Takagi, J., and Springer, T.A. Cysteine-rich module structure reveals a fulcrum for integrin rearrangement upon activation. *Nature Structural & Molecular Biology*, 9, (4): 282–287, **2002**. 33

[95] Spatz, J.P. Nano-and Micropatterning by Organic-Inorganic Templating of Hierarchical Self-Assembled Structures. *Angewandte Chemie International Edition*, 41, (18), **2002**. 34

[96] Spatz, J.P., Sheiko, S., and Moller, M. Ion-stabilized block copolymer micelles: film formation and intermicellar interaction. *Macromolecules*, 29, (9): 3220–3226, **1996**. 34

[97] Gao, Z. and Eisenberg, A. A model of micellization for block copolymers in solutions. *Macromolecules*, 26, (26): 7353–7360, **1993**. 34

[98] Spatz, J.P., Roescher, A., Sheiko, S., Krausch, G., and Moller, M. Noble metal loaded block lonomers: micelle organization, adsorption of free chains and formation of thin films. *Advanced Materials*, 7, (8), **1995**. 35, 50

[99] Glass, R., Moller, M., and Spatz, J.P. Block copolymer micelle nanolithography. *Nanotechnology*, 14, (10): 1153–1160, **2003**. 36

[100] Glass, R., Arnold, M., Blummel, J., Kuller, A., Moller, M., and Spatz, J.P. Micro-nanostructured interfaces fabricated by the use of inorganic block copolymer micellar monolayers as negative resist for electron-beam lithography. *Advanced Functional Materials*, 13, (7): 569–575, **2003**. 36

[101] Bansmann, J., Kielbassa, S., Hoster, H., Weigl, F., Boyen, HG, Wiedwald, U., Ziemann, P., and Behm, RJ. Controlling the Interparticle Spacing of Au- Salt Loaded Micelles and Au Nanoparticles on Flat Surfaces. *Langmuir*, 23, (20): 10150–10155, **2007**. 36

[102] Arnold, M., Hirschfeld-Warneken, V.C., Lohmueller, T., Heil, P., Bluemmel, J., Cavalcanti-Adam, E.A., Lpez-Garca, M., Walther, P., Kessler, H., Geiger, B., and Spatz, J.P. Induction of cell polarization and migration by a gradient of nanoscale variations in adhesive ligand spacing. *Nano Letters*, 8, (7): 2063–2069, **2008**. 36, 71

[103] Krishnamoorthy, S., Hinderling, C., and Heinzelmann, H. Nanoscale patterning with block copolymers. *Materials Today*, 9, (9): 40–47, **2006**. 36

[104] Darhuber, A.A., Troian, S.M., Miller, S.M., and Wagner, S. Morphology of liquid microstructures on chemically patterned surfaces. *Journal of Applied Physics*, 87: 7768, **2000**. 36

[105] Glass, R. *Micellar Nano- and Electron Beam Lithography and its Application.* PhD thesis, University of Heidelberg, **2005**. 37

[106] Chambon, F. and Winter, H.H. Linear viscoelasticity at the gel point of a crosslinking PDMS with imbalanced stoichiometry. *Journal of Rheology*, 31: 683, **1987**. 37

[107] Balazs, E.A. and Leshchiner, A. Cross-linked gels of hyaluronic acid and products containing such gels, January 13 1987. US Patent 4,636,524. 37

[108] Sheu, M.T., Huang, J.C., Yeh, G.C., and Ho, H.O. Characterization of collagen gel solutions and collagen matrices for cell culture. *Biomaterials*, 22, (13): 1713–1719, **2001**. 37

[109] Bluemmel, J., Perschmann, N., Aydin, D., Drinjakovic, J., Surrey, T., Lopez-Garcia, M., Kessler, H., and Spatz, J.P. Protein repellent properties of covalently attached peg coatings on nanostructured sio(2)-based interfaces. *Biomaterials*, 28, (32): 4739–4747, Nov 2007. 38

[110] Lussi, J.W., Falconnet, D., Hubbell, J.A., Textor, M., and Csucs, G. Pattern stability under cell culture conditionsa comparative study of patterning methods based on PLL-g-PEG background passivation. *Biomaterials*, 27, (12): 2534–2541, **2006**. 38

[111] Lee, J.H., Lee, H.B., and Andrade, J.D. Blood compatibility of polyethylene oxide surfaces. *Progress in Polymer Science*, 20, (6): 1043–1079, **1995**. 38

[112] Lin, H., Kai, T., Freeman, B.D., Kalakkunnath, S., and Kalikas, D.S. The effect of cross-linking on gas permeability in cross-linked poly (ethylene glycol diacrylate). *Macromolecules*, 38, (20): 8381–8393, **2005**. 38

[113] Moon, J.J., Lee, S.H., and West, J.L. Synthetic biomimetic hydrogels incorporated with ephrin-A1 for therapeutic angiogenesis. *Biomacromolecules*, 8, (1): 42–49, **2007**. 38

[114] Bryant, S.J., Nuttelman, C.R., and Anseth, K.S. Cytocompatibility of UV and visible light photoinitiating systems on cultured NIH/3T3 fibroblasts in vitro. *Journal of biomaterials science. Polymer edition*, 11, (5): 439, **2000**. 38

[115] Brown, K.R. and Natan, M.J. Hydroxylamine seeding of colloidal Au nanoparticles in solution and on surfaces. *Langmuir*, 14, (4): 726–728, **1998**. 41

[116] Turkevich, J., Stevenson, P.C., and Hillier, J. A study of the nucleation and growth processes in the synthesis of colloidal gold. *Discussions of the Faraday Society*, 11: 55–75, **1951**. 41

[117] Lohmueller, T., Bock, E., and Spatz, J.P. Synthesis of Quasi-Hexagonal Ordered Arrays of Metallic Nanoparticles with Tuneable Particle Size. *Advanced Materials*, 20, (12): 2297–2302, **2008**. 41

[118] Su, KH, Wei, QH, Zhang, X., Mock, JJ, Smith, DR, and Schultz, S. Interparticle coupling effects on plasmon resonances of nanogold particles. *Nano Letters*, 3, (8): 1087–1090, **2003**. 41

[119] Elbert, D.L., Pratt, A.B., Lutolf, M.P., Halstenberg, S., and Hubbell, J.A. Protein delivery from materials formed by self-selective conjugate addition reactions. *Journal of Controlled Release*, 76, (1-2): 11–25, **2001**. 43

[120] Cleveland, JP, Manne, S., Bocek, D., and Hansma, PK. A nondestructive method for determining the spring constant of cantilevers for scanning force microscopy. *Review of Scientific Instruments*, 1, (2): 5, **1993**. 45, 116

[121] Cavalcanti-Adam, A.E. *The control of cell adhesion and adhesion dependent events by nanotemplates regulating the spacial arrangement of integrin ligands.* PhD thesis, Universty of Heidelberg, **2005**. 45

[122] Spatz, J.P., Mossmer, S., Hartmann, C., Moller, M., Herzog, T., Krieger, M., Boyen, H.G., Ziemann, P., and Kabius, B. Ordered deposition of inorganic clusters from micellar block copolymer films. *Langmuir*, 16, (2): 407–415, **2000**. 50

[123] Larsen, A.E. and Grier, D.G. Melting of metastable crystallites in charge-stabilized colloidal suspensions. *Physical review letters*, 76, (20): 3862–3865, **1996**. 50

[124] Grabar, K.C., Brown, K.R., Keating, C.D., Stranick, S.J., Tang, S.L., and Natan, M.J. Nanoscale characterization of gold colloid monolayers: a comparison of four techniques. *Anal. Chem*, 69, (3): 471–477, **1997**. 53

[125] Aydin, D., Schwieder, M., Louban, I., Knoppe, S., Ulmer, J., Haas, T.L., Walczak, H., and Spatz, J.P. Micro-nanostructured protein arrays: a tool for geometrically controlled ligand presentation. *Small*, 5, (9): 1014–1018, May 2009. 54, 55, 91

[126] Orm, M., Cubitt, A.B., Kallio, K., Gross, L.A., Tsien, R.Y., and Remington, S.J. Crystal structure of the Aequorea victoria green fluorescent protein. *Science*, 273, (5280): 1392, **1996**. 54, 55

[127] Wexler, A. Vapor pressure formulation for ice. *J. Res. Natl. Bur. Stand. Part A*, 81: 5–19, **1977**. 56

[128] Hertz, H. Ueber die Beruehrung fester elastischer Koerper. *Journal fuer die reine und angewandte Mathematik*, 92: 156–171, **1881**. 57, 58, 119

[129] Sneddon, I.N. The relation between load and penetration in the axisymmetric Boussinesq problem for a punch of arbitrary profile. *Int. J. Eng. Sci*, 3, (1): 47–57, **1965**. 119

[130] Weisenhorn, AL, Khorsandi, M., Kasas, S., Gotzos, V., and Butt, H.J. Deformation and height anomaly of soft surfaces studied with an AFM. *Nanotechnology*, 4: 106–106, **1993**. 57, 119

[131] Dechantsreiter, M.A., Planker, E., Matha, B., Lohof, E., Holzemann, G., Jonczyk, A., Goodman, S.L., and Kessler, H. N-Methylated Cyclic RGD Peptides as Highly Active and Selective $\alpha_V\beta_3$ Integrin Antagonists. *J. Med. Chem*, 42, (16): 3033–3040, **1999**. 58

[132] Baneyx, G., Baugh, L., and Vogel, V. Fibronectin extension and unfolding within cell matrix fibrils controlled by cytoskeletal tension. *Proceedings of the National Academy of Sciences*, 99, (8): 5139, **2002**. 59

[133] Iba, Y., Shibata, A., Kato, M., and Masukawa, T. Possible involvement of mast cells in collagen remodeling in the late phase of cutaneous wound healing in mice. *International immunopharmacology*, 4, (14): 1873–1880, **2004**. 59

[134] Aydin*, D., Louban*, I., Lohmueller, T., Fiammengo, R., A., Cavalcanti-Adam E., Kessler, H., and Spatz, J. P. Polymeric substrates with tunable elasticity and nanoscopically controlled biomolecule density. *in preparation*, **2009**. Daniel Aydin and Ilia Louban contributed equally to this work. 59

[135] Zaidel-Bar, R., Cohen, M., Addadi, L., and Geiger, B. Hierarchical assembly of cell–matrix adhesion complexes. *Biochemical Society Transactions*, 32: 416–420, **2004**. 64

[136] von Wichert, G., Haimovich, B., Feng, G.S., and Sheetz, M.P. Force-dependent integrin–cytoskeleton linkage formation requires downregulation of focal complex dynamics by Shp2. *The EMBO Journal*, 22, (19): 5023, **2003**. 64

[137] Keselowsky, B.G., Collard, D.M., and Garcia, A.J. Integrin binding specificity regulates biomaterial surface chemistry effects on cell differentiation. *Proceedings of the National Academy of Sciences*, 102, (17): 5953–5957, **2005**. 64

[138] Giannone, G. and Sheetz, M.P. Substrate rigidity and force define form through tyrosine phosphatase and kinase pathways. *Trends in Cell Biology*, 16, (4): 213–223, **2006**. 64

[139] Latchman, D.S. Transcription factors: an overview. *International Journal of Biochemistry and Cell Biology*, 29, (12): 1305–1312, **1997**. 64

[140] Woods, A.J., Roberts, M.S., Choudhary, J., Barry, S.T., Mazaki, Y., Sabe, H., Morley, S.J., Critchley, D.R., and Norman, J.C. Paxillin associates with poly (A)-binding protein 1 at the dense endoplasmic reticulum and the leading edge of migrating cells. *Journal of Biological Chemistry*, 277, (8): 6428–6437, **2002**. 64

[141] Selhuber, Christine. *Biological Adhesion on Nanopatterned Substrates Studied with Force Spectroscopy and Microinterferometry.* PhD thesis, University of Heidelberg, **2006**. 66, 79, 82, 118

[142] Reinhart-King, C.A., Dembo, M., and Hammer, D.A. The dynamics and mechanics of endothelial cell spreading. *Biophysical journal*, 89, (1): 676–689, **2005**. 66

[143] Cuvelier, D., Théry, M., Chu, Y.S., Dufour, S., Thiéry, J.P., Bornens, M., Nassoy, P., and Mahadevan, L. The universal dynamics of cell spreading. *Current Biology*, 17, (8): 694–699, **2007**. 66

[144] Doebereiner, H.G., Dubin-Thaler, B., Giannone, G., Xenias, H.S., and Sheetz, M.P. Dynamic phase transitions in cell spreading. *Physical review letters*, 93, (10): 108105, **2004**. 66, 67, 89

[145] Doebereiner, H.G., Dubin-Thaler, B.J., Giannone, G., and Sheetz, M.P. Force sensing and generation in cell phases: analyses of complex functions. *Journal of Applied Physiology*, 98, (4): 1542–1546, **2005**. 67, 68

[146] Engler, A.J., Sen, S., Sweeney, H.L., and Discher, D.E. Matrix elasticity directs stem cell lineage specification. *Cell*, 126, (4): 677–689, **2006**. 69

[147] Cavalcanti-Adam, E.A., Volberg, T., Micoulet, A., Kessler, H., Geiger, B., and Spatz, J.P. Cell spreading and focal adhesion dynamics are regulated by spacing of integrin ligands. *Biophys J*, 92, (8): 2964–2974, Apr 2007. 71

[148] Lauffenburger, D.A. and Linderman, J.J. Receptors: Models for binding, trafficking, and signaling. **1996**. 73

[149] Benoit, M., Gabriel, D., Gerisch, G., and Gaub, H.E. Discrete interactions in cell adhesion measured by single-molecule force spectroscopy. *Nature cell biology*, 2, (6): 313–317, **2000**. 77

[150] Benoit, M. and Gaub, H.E. Measuring cell adhesion forces with the atomic force microscope at the molecular level. *Cells Tissues Organs*, 172: 174–189, **2002**. 77

[151] Helenius, J., Heisenberg, C.P., Gaub, H.E., and Muller, D.J. Single-cell force spectroscopy. *Journal of Cell Science*, 121, (11): 1785, **2008**. 77, 116

[152] Garcia, A.J., Huber, F., and Boettiger, D. Force required to break $\alpha 5\beta 1$ integrin-fibronectin bonds in intact adherent cells is sensitive to integrin activation state. *Journal of Biological Chemistry*, 273, (18): 10988–10993, **1998**. 81

[153] Munevar, S., Wang, Y., and Dembo, M. Traction force microscopy of migrating normal and H-ras transformed 3T3 fibroblasts. *Biophysical Journal*, 80, (4): 1744–1757, **2001**. 83

[154] Tashiro, K., Sephel, GC, Weeks, B., Sasaki, M., Martin, GR, Kleinman, HK, and Yamada, Y. A synthetic peptide containing the IKVAV sequence from the A chain of laminin mediates cell attachment, migration, and neurite outgrowth. *Journal of Biological Chemistry*, 264, (27): 16174–16182, **1989**. 91

[155] Brundle, C.R., Evans, C.A., and Wilson, S. Encyclopedia of Materials Characterization: surfaces, interfaces, thin films. **1992**. 113

[156] Binnig, G., Quate, C. F., and Gerber, Ch. Atomic force microscope. *Phys. Rev. Lett.*, 56, (9): 930–933, Mar 1986. 114

[157] Kasas, S., Gotzos, V., and Celio, MR. Observation of living cells using the atomic force microscope. *Biophysical journal*, 64, (2): 539–544, **1993**. 114

[158] Engel, A. and Muller, DJ. Observing single biomolecules at work with the atomic force microscope. *Nature Structural Biology*, 7, (9): 715–718, **2000**.

[159] Kong, X., Kawai, T., Abe, J., and Iyoda, T. Amphiphilic polymer brushes grown from the silicon surface by atom transfer radical polymerization. *Macromolecules*, 34, (6): 1837–1844, **2001**. 114

[160] Hansma, PK, Cleveland, JP, Radmacher, M., Walters, DA, Hillner, PE, Bezanilla, M., Fritz, M., Vie, D., Hansma, HG, Prater, CB, et al. Tapping mode atomic force microscopy in liquids. *Applied Physics Letters*, 64: 1738, **1994**. 115

[161] Domke, J., Dannoehl, S., Parak, W.J., Mueller, O., Aicher, W.K., and Radmacher, M. Substrate dependent differences in morphology and elasticity of living osteoblasts investigated by atomic force microscopy. *Colloids and Surfaces B: Biointerfaces*, 19, (4): 367–379, **2000**. 116

[162] Magonov, SN, Elings, V., and Whangbo, MH. Phase imaging and stiffness in tapping-mode atomic force microscopy. *Surf. Sci*, 375: L385–L391, **1997**. 116

[163] Mueller, D.J., Sapra, K.T., Scheuring, S., Kedrov, A., Frederix, P.L., Fotiadis, D., and Engel, A. Single-molecule studies of membrane proteins. *Current opinion in structural biology*, 16, (4): 489–495, **2006**. 116

[164] Puech, P.H., Poole, K., Knebel, D., and Muller, D.J. A new technical approach to quantify cell–cell adhesion forces by AFM. *Ultramicroscopy*, 106, (8-9): 637–644, **2006**. 116

[165] Vinckier, A. and Semenza, G. Measuring elasticity of biological materials by atomic force microscopy. *FEBS letters*, 430, (1-2): 12–16, **1998**. 117

[166] Timoshenko, SP and Goodier, JN. In:(3rd edn. ed.), Theory of Elasticity. **1970**. 119

[167] Heuberger, M., Dietler, G., and Schlapbach, L. Mapping the local Young's modulus by analysis of the elastic deformations occurring in atomic force microscopy. *Nanotechnology*, 6, (1): 12–23, **1995**. 119

[168] Weast, RC. Handbook of Chemistry and Physics, 57. **1976**. 119

Acknowledgments

An erster Stelle gilt der Dank meinem Doktorvater, Prof. Joachim P. Spatz, für die Möglichkeit die ich in den vergangenen dreieinhalb Jahren genoss, in einem interdisziplinären und hoch interessanten Bereich der Wissenschaft forschen zu dürfen. Insbesondere für das Vertrauen, das er meiner Arbeit entgegenbrachte, die Freiheit, die er mir dabei ließ und die zahlreiche Möglichkeiten die Ergebnisse national und international präsentieren zu dürfen.

Prof. Reiner Fink danke ich herzlich für die übernahme des Zweitgutachtens und allen Prüfern für ihre Mühen sich durch diese interdisziplinäre Materie zu arbeiten.

Ganz herzlich möchte ich Roberto Fiammengo danken, ohne sein Engagement wäre die Durchführung meiner Arbeit so nicht möglich gewesen. Ein besonderer Dank gilt meinen HiWis: Christina Gosmann, Michael Dieckman und Catharina Cadmus für die unermüdliche Unterstützung bei der Probenherstellung und das "on demand" Arbeiten. Des weiteren gilt mein Dank Daniel Aydin, sowie Theobald Lohmüller und Marco Schwieder für die zahlreichen Einweisungen und kritischen Diskussionen. Danke Jungs, ich hab viel von euch gelernt. Bei Ada Cavalcanti-Adam, Babak Hosseini, Tobias Wolfram, Kai Uhrig, Simon Schuz, Tamas Haraszti, Ralf Richter, Jasmin Zahn und Vera Hirschfeld-Warneken möchte ich mich für die fruchtbaren Diskussionen, kluge Vorschläge und kritische Anmerkungen zu meiner Arbeit bedanken. Christine Selhuber danke ich sehr für die Einwesungen in die vielfältigen Methoden des Projekts, ohne sie wäre meine Einlernzeit viel länger und schwieriger verlaufen. Nadine Perschmann, Jacques Blümmel und Nicole Rauch möchte ich für die Begleitung meiner ersten Schritte bei der PEG Herstellung bedanken. Natürlich geht der Dank auch an unsere Techniker: Ioanis Grigoridis für die zuverlässige und sehr flexible Unterstützung am Cryo, Sigrid Riese und Richard Morlang für die Unterstützung im Bio- und Chemielabor. Danke für eure Hilfe, sie hat mir einige Nerven und Zeit erspart! Bei Daniel Aydin, Babak Hosseini, Ada Cavalcanti-Adam, Roberto Fiammengo, Tobias Wolfram, Janosch Deeg, Tamas Haraszti und Vera Hirschfeld-Warneken möchte ich mich für das Korrekturlesen meiner Arbeit bedanken.

Dem gesamten AK Spatz möchte ich für die schöne, freundschaftliche Atmosphäre und sehr angenehmes und abwechslungsreiches Arbeitsklima danken.

Vielen Dank!

Ganz besonders möchte ich meiner Familie danken. Sie hat mich während meines Studiums und der Promotion unermüdlich und vorbehaltlos unterstützt, mir viele Unannehmlichkeiten erspart und schöne Dinge ermöglicht. Ich habe euch viel zu verdanken!

Appendix

A

Appendix

A.1 Scanning electron microscopy

The SEM technique is capable to visualize surface topography and even chemical composition with sub-micrometer resolution [155]. To generate an image of the surface of interest, it is scanned with a focused high energy beam of electrons in a raster scan pattern.

Usually, the electrons are generated by field emission cathodes and then accelerated by strong electron fields up to 30 kV. The beam is focused by a set of magnetic and electrostatic lenses to a diameter between 5 and 0.5 nm, before striking the sample. The interaction of the beam with the substrate generates a variety of different signals depending on the nature of the sample and the energy of the electrons. Its penetration depth is controlled by acceleration voltage and sample properties. These signals result from interactions of the electron beam with atoms at or near the surface of the sample. Principally, the radiation generates a signal contrast between an object and the surrounding surface, similar to light microscopy. If primary electrons hit the surface, they can be reflected by elastic scattering and are then called backscattered electrons (BSE). Moreover, primary electrons can cause ionization of atoms on the surface resulting in low energy secondary electrons (SE). The SE originate from the outer shell of an atom hit by either a primary or a backscattered electron. In general, electrons with an energy less than 50 eV are considered as secondary electrons.

Since the ratio of backscattered and primary electrons strongly depends on the atomic number of the analyzed sample, BSE provide a very good material contrast. In contrary, the amount of secondary electrons is nearly independent from the atomic number of the material. Consequently the contrast is less emphasized, while the topography of the sample is brought out.

Unlike in optical microscopy, the magnification of an SEM does not depend on the power of the magnification lens. The objective and condenser lenses inside the electron column are rather used to focus the beam to a smaller diameter. The primary electron beam, scanning the surface, is synchronized with a cathode ray

tube (CRT) display, therefore, the obtained image is a result of the mapped intensity from the detected signal. Hence, the magnification can be controlled by altering the size of the scanned region. Decreasing the dimension of this area results in a higher magnification.

A.1.1 Cryo scanning electron microscopy

PEG-DA hydrogels and cells on their surface are high water-content materials, therefore, no conventional SEM could be applied. Thus, special SEM techniques are needed. Here, we used low temperature ($T_{op} \approx -130°C$) SEM, so-called cryo SEM to lower the partial pressure of water and ice, respectively, in order to allow for high resolution imaging of PEG-DA hydrogel samples.

Unfortunately, no conductive coating could be applied, due to the aforementioned properties of PEG-DA hydrogels. This results in a low conductivity surface, which allowed to use only low acceleration voltages. Since gold nanoparticles and surrounding ice feature very high material contrast, in terms of electron density, BSE electrons were detected to visualize the gold nanoarrays.

A.2 Scanning probe microscopy

Scanning probe microscopy* (SPM) was invented as a further development of scanning tunneling microscopy (STM) by G.Binning in the 1980s [156]. It is a versatile technique for investigation of surface structures at the nanometer and micrometer scale. It is based on the detection of attractive and repulsive forces between the probe and the surface of interest. The advantage of the SPM is, that no specific environmental limitations like low temperatures or pressures are necessary. Therefore, SPM has proved its value in material and life sciences not only for resolving the topographical structures, but also for probing inherent properties of samples, like local interaction forces, mechanical properties or dynamics in a natural environment [70, 157–159]. Since SPM is a widely used and well-known technique, only a brief description will be given here.

The heart of the SPM instrument is the small (tens µm) spring-like cantilever with a very sharp (1 -10 nm sized) tip at its end (Fig. A.1). This tip is exposed to attractive or repulsive dipole-dipole, van der Waal and electrostatic interaction forces, when scanned over the surface. According to a Hook's law, these forces causes a deflections of the cantilever towards or away from the sample. The detection of these small deflections is realized by the so-called optical lever principle. Therefore, a laser beam is reflected from the backside of a cantilever and then focused on a four-quadrant photodiode. This setup allows to convert small bending angles of the cantilever into measurable a large signal on the detector. The cantilever itself

*The terminus atomic force microscopy (AFM) is also often used in the literature.

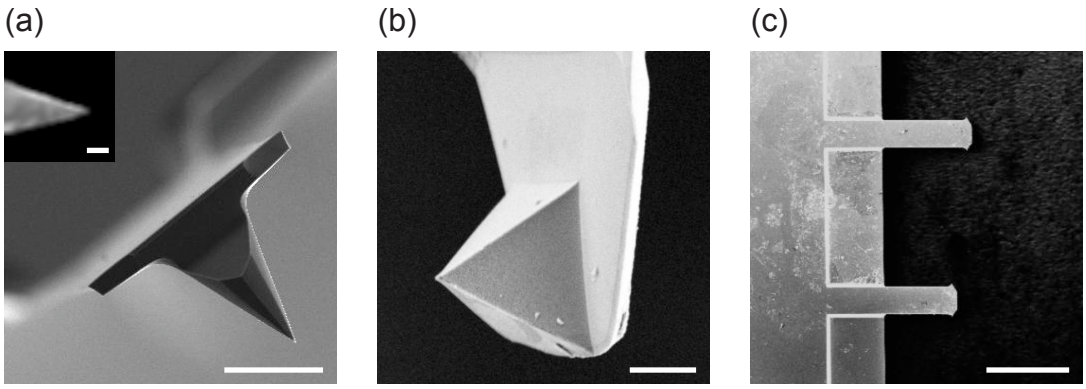

Figure A.1: Scanning electron micrographs of cantilever types used in this thesis. (a) Cantilever used for scanning of nanodecorated surfaces and indentation measurements with quasi-conical tip shape and low radius of curvature of about 10 nm. Scale bar 10 µm, inset 100 nm. (b) Cantilever used for scanning of PEG-DA hydrogels with low spring constants of about 0.6 N/m and tip radius of curvature of approximately 30 nm. Scale bar 2 µm. (c) Tipless cantilever used for SCFS. Scale bar 100 µm.

is attached to the piezo actuator, to regulate the tip-sample interaction distances. Figure A.2 summarizes the basic principle of scanning probe microscopy.

Three basic scanning modes exists in scanning probe microscopy: contact, non contact and intermittent contact mode. In contact mode, the tip is in permanent contact with the investigated surface. Changes in surface topography cause changes in the cantilever deflection. While scanning, the cantilever deflection is used as feedback signal to control the z-movement of the piezo actuator in a way that the deflection remains constant. The readout of the piezo actuator voltage corresponds to the topography of the investigated sample.

During intermittent and non-contact mode the cantilever is externally driven to oscillate near its resonance frequency. Here, the amplitude of this oscillation (typically several nm) is the parameter to be kept constant. The forces acting on the cantilever, when the tip comes close to the surface, cause small changes in the amplitude. This changes, detected by the photodiode and fed back to the piezo actuator provide the readout signal of the topography composition of the sample [160]. The only difference between the intermittent and non contact mode is that the tip experiences short interactions with the sample at the lower reversal point of the oscillation in intermittent contact mode and no interaction at all in non contact mode. Intermittent and non contact mode are often used in biological applications, since the cantilever does not drag across the surface, as in contact mode, which results in less surface damage.

Different signals, and thus information about the investigated sample can be provided by SPM. First and most obvious is height signal. These topography information recorded by the piezo actuator is, from a mathematical point of view, a convolution of the tip and the surface shape. Therefore, no topographical features

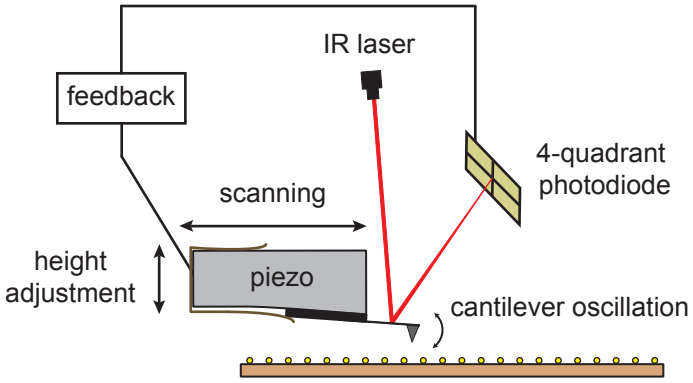

Figure A.2: The principle of SPM. During the scanning of the sample, the oscillating cantilever experiences interaction forces between its tip and the sample, when brought close to the surface. Small changes of its amplitude can be detected by a four-quadrant photodiode via a focused laser beam. A continuous feed-back routine monitors these changes, and keeps the amplitude constant, by adjusting the cantilever-sample distance by a piezo actuator (non-contact mode).

can be resolved with SPM, when they are significantly smaller than the scanning tip size.

The deflection signal, provided by the photodiode is a consequence of the finite reaction time of the SPM feedback. It is well suitable to visualize the roughness of the surface e.g. in case of cell imaging, the underlying cytoskeleton of the investigated cell [161].

The phase signal corresponds to the recorded phase shift between the drive phase and the actual cantilever oscillation phase. It is caused by elastic or viscous response of the investigated surface and can give an insight into its mechanical properties. Thus visualize the mechanical contrast of the investigated sample [162].

A.2.1 Atomic force spectroscopy

As mentioned above, the detection of forces is the major principle of SPM. For imaging purposes, it is not mandatory to determine the spring constant of the cantilever, only its order of magnitude is important to estimate cantilever-sample interaction forces, e.g. to assure the integrity of the sample. In case of atomic force spectroscopy (AFS), cantilever-sample interaction forces are in focus of interest. Therefore, a precise determination of the spring constant is necessary. Commercially available cantilevers are pre-calibrated, but feature huge variance to the nominative values. Because of this variance, every cantilever has to be individually calibrated to obtain characteristic force constants by analyzing the power spectrum of thermal noise fluctuations of the cantilever [120].

In past decades AFS was established as a standard approach to quantify molecule-molecule [163], cell-cell [164] and cell-substrate [151] interaction forces or mechanical

properties of investigated samples [165]. The principle of AFS is demonstrated in Figure A.3. Here, the cantilever can be seen as a spring with the spring constant k where the deflection of the cantilever Δd corresponds to a force F acting on it.

$$F = -k\Delta d \tag{A.1}$$

If the force is attractive, the cantilever will be bent towards the sample surface, which will result in negative values in the recorded force-distance curve. If the force is repulsive, the cantilever will be bent away from the sample surface and the deflection value will be positive. Unfortuntely, the four-quadrant photodiode is not able to

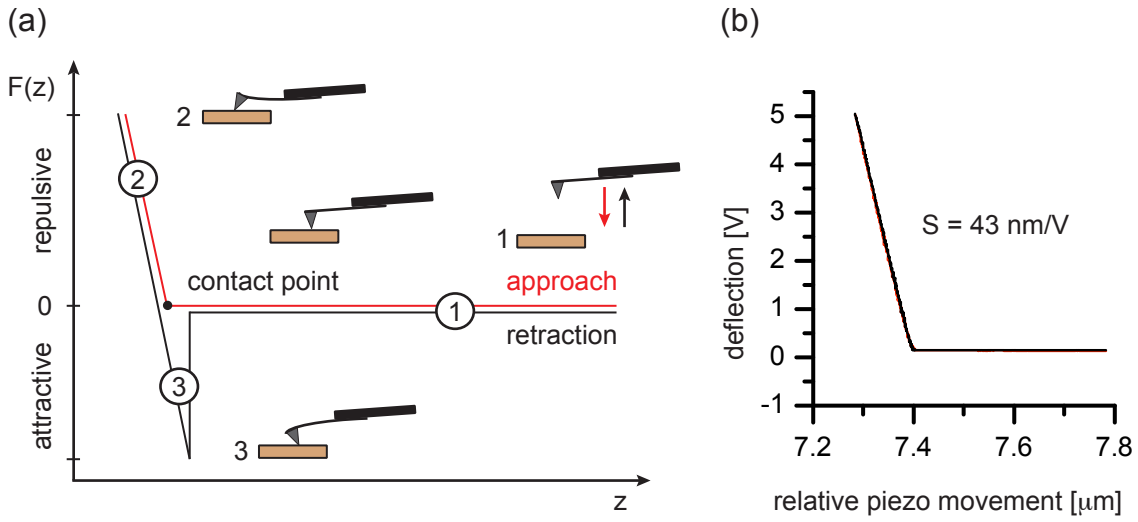

Figure A.3: The principle of AFS. (a) (b)Typical deflection-distance curve for calibration purposes. The height-deflection relationship or sensitivity S could be determined via linear fit. Note: no attractive interactions are measured!

directly determine cantilever deflections. Its output signal U is the difference of laser intensities on corresponding quadrants and is expressed in Volt. This voltage can be converted into the the deflection of the cantilever by determination of the linear height-deflection relationship measured by pressing the cantilever onto very stiff (to neglect elasticity effects) surface (Fig. A.3b). Linear fit delivers the sensitivity S, which is the proportionality factor expressed in m/V

$$\Delta d = S \cdot U \tag{A.2}$$

Thus, the force is finally calculated by

$$F = -k\Delta d = -k(d - d_0) = -k \cdot SU \tag{A.3}$$

The sensitivity S is crucially affected by the cantilever-sample contact point, since this point defines the effective cantilever length. Moreover, the effective cantilever

length affects its spring constant, and therefore, the force acting on the surface or molecule of interest. Especially in case of single cell force spectroscopy (SCFS), where the cantilever is loaded by the cell, the cantilever-sample interaction point is unique for each acquired force-distance curve, due to the variable cell position (Fig. 7.2). Thus, a small deviation from equation (A.3) will occur, and a correction factor c needs to be calculated for each experiment [141]:

$$F = c \cdot F_0 \tag{A.4}$$

with F_0 as measured force and

$$c = \frac{1 + 2l_C}{L_0 - 2l_C + l_L} \tag{A.5}$$

were L_0 is the cantilever length and l_C and l_L are the individual cell and laser position, respectively.

A.2.2 The Hertz model and indentation measurements

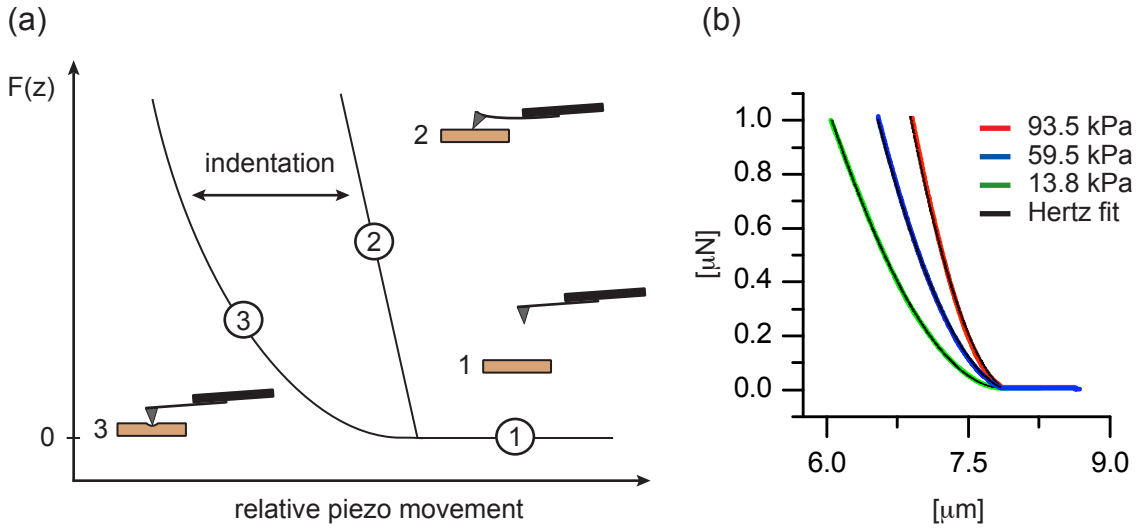

Figure A.4: (a) Schematic representation of typical force-distance curves, derived during indentation measurements on hard (2) and soft (3) substrates. During the approach, no forces act between tip and sample (1). When tip strikes the hard sample (2), the recorded signal originates from the linear (Hook) cantilever deformation, no indentation is measurable. If the sample is soft (3) it will be deformed by the tip, which results in the deviation from the linear relationship between the force and the distance. (b) Examples of the force distance curves obtained during the E_Y measurements on different PEG-DA hydrogels and corresponding Hertz fits.

According to Hook's law the Young modulus is the mechanical resistance of a material while elongating or compressing. Its dimension is force per surface area.

As long as the stress-strain relation is linear, the deformation of the material is elastic and the material will always regain its original shape if no more force is applied. This general viscoelasticity theory outlined above, and in more detail presented in Chapter 2.2.2, is based on the theory of Hertz [128, 166]. In general, the theory of Hertz describes the deformation of an elastic sphere under external load against a rigid, flat surface.

As shown in Figure A.4, determination of substrate elasticity by SPM is performed by indenting a very stiff (compared to the sample) probe of defined geometry into the sample of interest and monitoring the resulting force-distance curves. This results in a deformation, which is the sum of the sample and indenter (tip) deformations. The most suitable modification of the Hertz theory for SPM tip-sample system was introduced by Sneddon [129] and describes an infinitely hard indenter with a special geometry and flat, deformable substrate [130, 167, 167]. For a conical tip with a opening angle α, the total force F_{cone} as a function of the indentation δ is described by:

$$F_{cone}(\delta) = \frac{2E^*}{\pi(tan(\frac{\alpha}{2}))}\delta^2 \tag{A.6}$$

where E^* is the relative Young modulus:

$$\frac{1}{E^*} = \frac{1-\mu_{tip}^2}{E_{tip}} + \frac{1-\mu_{sample}^2}{E_{sample}} \tag{A.7}$$

and μ the Poisson ratio[†]. If the modulus of the studied material E_{sample} is much lower than the modulus of the indenter E_{tip}, equation (A.7) can be simplified:

$$\frac{1}{E^*} \approx \frac{1-\mu_{sample}^2}{E_{sample}} \tag{A.8}$$

To determine the elasticity of the PEG-DA samples, force distance curves were recorded and fitted to the equation (A.6). In order to accurately derive Young moduli, the characteristics of the indenter such as the cone angle of the tip and the spring constant of the cantilever were carefully measured. Examples of indentation force-distance curves and Hertz fits are given in Figure A.4b.

[†]Poisson ratio is the ratio of the orthogonal strain and the strain along the direction of elongation [168]. Is was assumed to be μ_{PE-DA}=0.5 due to the high water content of PEG-DA (μ_{H_2O}=0.5)

A.3 Abbreviations

Abbreviation	Full Name
AFM	atomic force microscopy
ATP	adenosine triphosphate
BCMN	block copolymer micelle nanolithography
BSE	backscattered electron
CAM	cell adhesion molecule
CMC	critical micelle concentration
CRT	cathode ray tube
DFS	dynamic force spectroscopy
DNA	deoxyribonucleic acid
ECM	extracellular matrix
FA	focal adhesion
FAK	focal adhesion kinase
FBS	fetal bovine serum
GAG	glycosaminoglycan
GFP	green fluorescent protein
ICAM-1	intercellular adhesion molecule-1
IKVAV	isoleucine-lysine-valine-alanine-valine
LFA-1	leukocyte function-associated antigen-1
PAAM	poly(acryl amide)
PDMS	poly(dimethyl siloxane)
PEG	poly(ethylene glycol)
PEG-DA	poly(ethylene glycol)-diacrylate
PS	polystyrene
PVP	poly(vinyl pyridine)
REF	rat embryonic fibroblast
RGD	arginine-glycine-aspartic acid
SE	secondary electron
SEM	scanning electron microscope
SPM	scanning probe microscopy
STM	scanning tunneling microscope
YFP	yellow fluorescent protein

A.4 List of Publications

Louban, I., Cavalcanti-Adam, A., Deeg, A. J., Aydin, D., Selhuber-Unkel, C., Cadmus, C., Fiammengo, R., and Spatz, J. P. Mimicking Cellular Enviroments: effects of elastic nanopatterned substrates on integrin-mediated cell spreading. *in preparation.*

Aydin, D.[‡], **Louban, I.**[‡], Perschmann, N., Blümmel, J., Lohmüller,T., Cavalcanti-Adam, E.A., Fiammengo, R., Kessler, H., and Spatz, J.P. Polymeric substrates with tunable elasticity and nanoscopically controlled biomolecule density. *in preparation.*

Hosseini, H. B., **Louban, I.**, Djandji, D., Wabnitz, H. G.,Deeg A.J., Bulbuc, N., Samstag, I., Gunzer, M., Spatz P. J. and Hämmerling. J. G. Immune synapse formation determines interaction forces between T cells and antigen presenting cells measured by atomic force microscopy. *submitted to PNAS.*

Aydin, D., Schwieder, M., **Louban, I.**, Knoppe, S., Ulmer, J., Haas, T.L., Walczak, H., and Spatz, J.P. Micro-Nanostructured Protein Arrays – A Tool for Geometrically Controlled Ligand Presentation. *Small*, 5, 1014–1018, 2009.

[‡]These two authors contributed equally to the work

Ich erkläre hiermit, dass ich die vorgelegte Dissertation selbst verfasst und mich keiner anderen als der von mir ausdrücklich bezeichneten Quellen und Hilfen bedient habe.

Heidelberg, den 24. August 2009

.....

Ilia Louban